Crystallographic and Microstructural Studies of Dental Enamel using Synchrotron X-ray Diffraction and Complementary Techniques

Samera Siddiqui

(BSc Hons)

Supervised by Dr Maisoon Al-Jawad and Dr Graham Davis

A thesis submitted to the University of London for the degree of Doctor of Philosophy

2014

Dental Physical Sciences Unit, Centre for Oral Growth and Development, Institute of Dentistry, Barts and The London School of Medicine and Dentistry, Queen Mary University of London

Statement of Originality

I declare that the research included within this thesis is my own work or that where it has been carried out in collaboration with, or supported by others, that this is duly acknowledged below and my contribution indicated. Previously published material is also acknowledged below.

I attest that I have exercised reasonable care to ensure that the work is original, and does not to the best of my knowledge break any UK law, infringe any third party's copyright or other Intellectual Property Right, or contain any confidential material.

I accept that the College has the right to use plagiarism detection software to check the electronic version of the thesis.

I confirm that this thesis has not been previously submitted for the award of a degree by this or any other university.

The copyright of this thesis rests with the author and no quotation from it or information derived from it may be published without the prior written consent of the author.

Name: Samera Siddiqui

Course: PhD

Title of work submitted: Crystallographic and Microstructural Studies of Dental Enamel using Synchrotron X-ray Diffraction and Complementary Techniques

Examination: A thesis submitted for the degree of Doctor of Philosophy, University of London

Signature:

Date:

Dedicated to

Mum, Baba and Atif.

This is for you.

Acknowledgements

I would like to thank my project supervisors Dr. Maisoon Al-Jawad and Dr. Graham Davis, for their continuous support, encouragement and guidance throughout the PhD, without which this achievement would not have been possible.

A special acknowledgement to all the beamline scientists at the synchrotron facilities visited during the course of this research project for data collection, their technical support, time and expert advice given during beam time is immensely appreciated. I am very grateful to Dr. David Mills for the tremendous amount of help and friendly advice. I would also like to thank Prof. Brian Clarkson and Harrison Chang at the Michigan Dental School for giving me the invaluable opportunity of working in their research group and for making me feel so welcome in the lab.

I am extremely thankful to the staff and students at the Dental Physical Sciences Unit who have all been very caring and friendly and made my time there pleasant. A special thank you to my fellow peers, Steve, Navina, Nasrine, Niall, Mohammed, Jamila, Rawan and Jing.

I would like to express a special appreciation to my parents and brother, Atif, for the endless love and prayers, which gave me the strength to carry on. Finally, I would like to extend my gratitude to all my friends and family who have been such an incredible support system, always giving me the encouragement and motivation to strive towards my goal. I am extremely lucky to have such wonderful and positive people in my life.

Abstract

The complex microstructure and properties of dental enamel have been studied for decades using a variety of quantitative and qualitative techniques in order to gain a greater depth of understanding behind the chemical and physical processes that are associated with the formation and destruction of this biological apatite. Dental enamel is composed of highly ordered carbonated hydroxyapatite crystals which, together with its small organic component, are responsible for its mechanical strength, allowing it to serve its functional purpose. Environmental changes at any stage of the biomineralisation process or post eruption can disrupt the orientation and alter the structure and function, which can have detrimental clinical effects.

The aim of this study is to understand and characterise the structural and crystallographic properties of disrupted enamel, and compare this to healthy unaffected tissue. Enamel affected by the genetic disorder, Amelogenesis Imperfecta, alongside enamel disrupted by dissolution and caries were studied using Synchrotron X-ray diffraction, 3D X-ray Microtomography, and Scanning Electron Microscopy techniques to relate these features to the clinically observed characteristics; to the chemistry; and to the known genetics of the tooth. Synchrotron radiation was used to map changes in preferred orientation, while the corresponding mineral density distributions were seen by using an in house developed, non-destructive microtomography system.

Structural information on dental enamel at the crystallographic and micron length scales can benefit a variety of different disciplines. This project has the potential to inform early diagnosis, develop a tool for an early recognition of progressive or highly variable medical conditions, and design potential treatment regimes. The comparison of affected enamel to that of healthy enamel will provide a unique opportunity to identify the developmental pathways required for normal tooth development and give insights into the basic principles underlying mammalian biomineralisation.

Table of Contents

List of Figures

List of Tables

List of Abbreviations

AD	Autosomal Dominant
AI	Amelogenesis Imperfecta
Al	Aluminium
AMEL	Amelogenin
APS	Advanced Photon Source
AD	Autosomal Dominant
AR	Autosomal Recessive
BM	Bending Magnet
CEJ	Cemento-Enamel Junction
CCD	Charge-Coupled Device
CRG	Collaborating Research Group
CRL	Compound Refractive Lenses
CT	Computed Tomography
DLS	Diamond Light Source
EDJ	Enamel Dentine Junction
ENAM	Enamelin
EPSRC	Engineering and Physical Sciences Research Council
ESRF	European Synchrotron Radiation Facility
EXPEDT	GSAS Editor
FA	Fluorapatite
FDI	World Dental Federation notation
FWHM	Full Width Half Maximum
GENLES	General Least Squares
GISRD	Grazing Incidence Synchrotron Diffraction

GSAS	General Structural Analysis System
HA	Hydroxyapatite
ICDD	International Centre for Diffraction Data
ICSD	Inorganic Crystal Structure Database
ID	Insertion Device
IDL®	Interactive Data Language
KLK4	Kallikrein 4
LaB6	Lanthanum Hexaboride
LAC	Linear Attenuation Coefficient
LINAC	Linear Accelerator
MMP20	Matrix Metalloproteinaise-20 (Enamelysin)
MPS	Mucopolysaccharidosis
OD	Orientation Distribution
OCP	Octacalcium Phosphate
O_{hkl}	Preferred Orientation
PDF	Powder Diffraction File
POWPLOT	Powder Pattern Plotting
POWPREF	Powder Data Preparation
ROI	Region of Interest
SAXS	Small Angle X-ray Scattering
SEM	Scanning Electron Microscopy
SMR	Scanning Microradiography
SNR	Signal to Noise Ratio
SXRD	Synchrotron X-ray Diffraction
TEM	Transmission Electron Microscopy

TCP	Tricalcium Phosphate
TDI	Time Delay Integration
TMR	Transversal Microradiography
WAXS	Wide Angle X-ray Scattering
XMaS	X-ray Magnetic Scattering
XMT	X-ray Microtomography
1D	One Dimensional
2D	Two Dimensional
3D	Three Dimensional
μ	Mu
ρ	Density
Å	Ångström
E	Energy
λ	Wavelength
θ	Theta
J	Texture Index
B	Magnetic field
E	Electron energy
I_i^{calc}	Calculated intensity at point *i*
y_i^{back}	Background intensity
R_{wp}	Weighted R Factor
R_{exp}	Expected R Factor
S_{ph}	Scale factor

Chapter 1: Introduction

1.1 Thesis structure

This thesis has been organised such that the general aims and objectives have been outlined in chapter 1. Chapters 2, 3 and 4 provide a basic overview of the structure and properties of human dental enamel and a theoretical background into the X-ray scattering and absorption methods used to conduct this study respectively. Chapter 5 reviews the techniques used to study enamel and the studies to date at different length scales. Chapter 6 describes the general materials and methods, with specific set up stated in each of the results chapters. Chapters 7 to 10 present the experimental results and discussion. A combined discussion is given in chapter 11, linking all the studies and suggestions of future work.

1.2 General aims and objectives

The aim of this project was to quantitatively characterise the crystallography and microstructure of human enamel affected by genetic and environmental factors to aid the understanding of enamel structure behaviour during biomineralisation and biodemineralisation.

The specific objectives were:

1. To use high resolution synchrotron X-ray diffraction to measure the crystallographic parameters of enamel
2. To image and obtain information on the mineral concentration of tooth specimens using TDI X-ray microtomography
3. To relate the clinical phenotype to the crystallographic and microstructural properties of enamel
4. To characterise and quantify the enamel texture in AI affected sample and carious enamel
5. To synthesise ordered apatite crystallites as a method of remineralising demineralised enamel

Chapter 2: Introduction to Enamel

2.1 Basic tooth structure

Human teeth are a small, yet important component of the body. Being the first point of contact with food and drink, they serve the functional requirement of mastication in preparation for digestion. They bear a wide range of imposed loads and physiological stresses, but must still retain structural strength, shape and integrity.

Each tooth (Fig. 2.1) is comprised of three major structural layers, enamel, dentine and the pulp cavity. Enamel is a hard, highly mineralised whitish, translucent material that forms a protective outer coating, supported by a less mineralised but tougher dentine structure. Dentine forms the core of each tooth; it spans out from the root to the crown, protecting the pulp cavity and maintains enamel integrity. The interface between these two materials is known as the enamel dentine junction (EDJ). The pulp cavity holds within it, nerves and blood vessels. The root of the tooth is encapsulated by the gingiva and mandible or maxillary bone to anchor the entire structure.

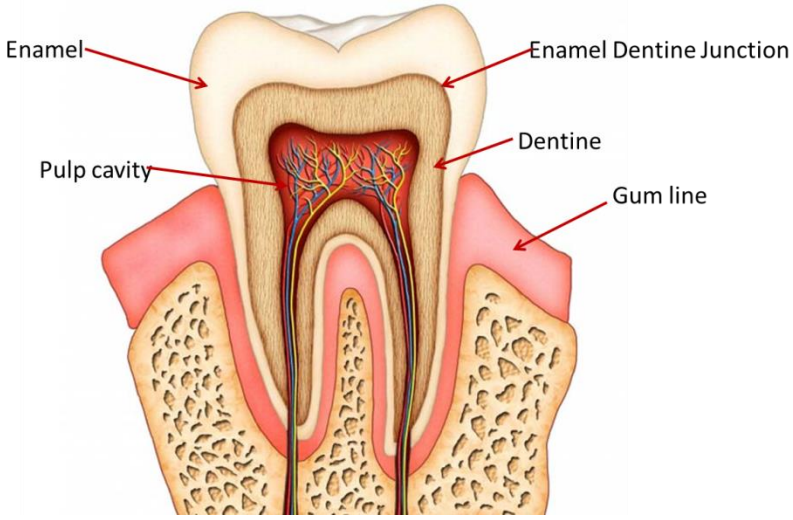

Figure 2.1: Basic schematic representation of the structure of a human tooth

(Image taken from http://beta.classmint.com).

Humans display two full sets of teeth during their lifetime, deciduous and permanent. The deciduous dentition (more commonly referred to as primary or milk teeth) develops during the prenatal stage and erupts between the ages of 6 to 8 months. It consists of incisors, canines and molars; these are exfoliated and replaced by the permanent dentition. Eruption of the permanent dentition begins at 6 years, which consists of the above tooth types, with the addition of premolars and develops as the jaw grows and matures (Atkinson and White, 1992). Morphology and anatomy of each tooth varies according to the tooth type and location in which it sits in the jaw. The anatomy of each tooth can be clinically distinguished by characteristics such as the size, shape and number of roots and cusps (Berkovitz et al., 2009, AlQahtani et al., 2010). Dental clinicians use an internationally recognised two digit numbering system, known as world dental federation notation (FDI), to describe the tooth type.

2.2 Hydroxyapatite crystal structure

Dental enamel is the strongest and most mineralised biological material present in the body, comprised of 96 wt% inorganic material in the form of mineral crystals and traces of organic material and fluid. The main mineral constituent of dental enamel is a non-stoichiometric calcium deficient carbonated hydroxyapatite (HA) [$Ca_{10}(PO_4)_6(OH)_2$] (Kay et al., 1964, Young, 1974). HA is a member of the calcium phosphate family, which also includes octacalcium phosphate (OCP), a precursor phase of HA and tricalcium phosphate (TCP) (Elliott, 1994).

The HA crystal can be best described as a series of hexagonal plates (Kerebel et al., 1979) stacked one on top of another, each rotated 60° in relation to the immediate neighbours to form a column (Fig. 2.2). Each plate has a central hydroxyl ion, enclosed by a triangle of calcium II ions, which is surrounded by a triangle of phosphate ions rotated out of phase by 60°, all within a hexagon of calcium I ions (Kay et al., 1964). Each atomic site within the HA crystal is susceptible to substitutions: the Ca site in the apatite structure can be substituted by varied metal cations, e.g. Na, K, Mg, Sr, Ba, Mn and Pb; the phosphate can be partially carbonate substituted; and the –OH site can accept F, Cl or H_2O substitution (represented by: $Ca,Sr,Mg,Na,H_2O,[\ ])_{10}(PO_4,HPO_4,CO_3P_2O_7)_6(OH,F,Cl,H_2O,O,[\ ])_2$).

Substitutions lead to distortions, altering the lattice parameters and affecting apatite solubility, an important factor to consider during the caries process (Robinson et al., 1995). The crystallographic unit cell stoichiometry is made up of four columnar calcium II ions, six screw axis calcium I and six phosphates located around the hydroxyls which occupy columns on the screw axes. Its structure consists of mirror planes at z= ¼ and ¾ (Reyes-Gasga et al., 2012). HA has space group (a crystallographic term to describe the symmetry of the crystal) symmetry $P6_3/m$ and lattice parameters a = 9.513Å and c = 6.943Å (Young and Mackie, 1980).

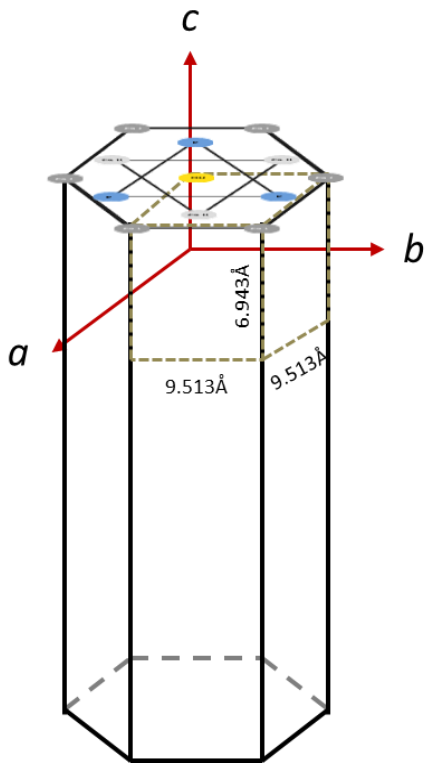

Figure 2.2: Schematic representation of an enamel HA crystallite, showing the arrangement of ions in the hexagonal plate. The dashed box defines a crystallographic unit cell.

Enamel crystallites grow by deposition of ions on the crystal faces *a*, *b* and *c*. These can be defined as the crystallographic axes of the HA structure. Rapid elongation occurs in the direction of the *c*-axis (Thewlis, 1940), from the build-up of ions in the (001) plane. This is followed by an increase in the crystallite width (*b* axis) and then thickness (*a*-axis) at a

slower rate by addition to the (010) plane and the (100) plane of the crystallite respectively (Simmer and Fincham, 1995). Crystallites display structural defects such as screw dislocations, edge dislocations as a result of crystal growth or deformation through substitution (Kerebel et al., 1979). The cross-sectional dimensions of each enamel crystallite are approximately 50 nm × 25 nm and up to 1 mm in length extending from the dentine to the enamel surface.

2.3 Enamel microstructure

At a light microscope level the microstructure of dental enamel consists of aligned prisms which run approximately at acute angles from the enamel–dentine junction (EDJ) to the tooth surface and likely to cross one another in this course (Boyde, 1964). Prisms are the basic units of enamel and are made up of multitudes of HA crystallites. The cross sectional shape of the prism in human enamel can best be depicted as a keyhole structure, with a head directed towards the occlusal surface and a tail region orientated cervically, this allows very close packing. The dimensions of a prism are 3-6 μm in diameter and 9 μm in height (Ten Cate, 1989).

Early X-ray diffraction and electron microscopy studies established that within each prism, HA crystallites are preferentially arranged with their long (*c*) axis almost parallel to the long axis in the head region of the prism, yet gradually change orientation in the tail of the keyhole structure. The boundaries between prisms, interprismatic regions, consist of HA crystallites aligned in a different direction from those found in the prisms. Thewlis (1940) was first to demonstrate deviation of crystallites within prisms from the prism axis by about 5^0 and in the interprismatic region by as much as 40^0 from the prism axis. Further studies confirmed the average inclination angle from the prism axes ranges from 0^0 to 40^0 in the prism head and as much as 70^0 in the prism tail, with deviation always directed towards the cervical parts of the tooth (Poole and Brooks, 1961).

Heterogeneity in enamel microstructure has been observed due to the variation in the orientation of prisms and the crystallites within. In the cuspal regions of the tooth, the mean direction of the crystallites is parallel with the direction of the prisms (perpendicular to natural biting surfaces (Simmons et al., 2011). However, in the lateral enamel (sides of the

crown); crystallite direction is displaced away from the prism axes towards the cervical margin (Poole and Brooks, 1961, Glas, 1962, Meckel et al., 1965). Highest crystal order of HA occurs near the occlusal surface of the enamel (9 μm below the surface) and then decreases travelling towards the EDJ (Low, 2004). These areas of high crystallite alignment match the expected biting surfaces, where greatest force is expected (Al-Jawad et al., 2007). Deciduous enamel has less well-structured crystal arrangement than permanent enamel, although prisms are smaller, the crystallites within them are larger (Lynch, 2013).

2.4 Amelogenesis

Amelogenesis (enamel formation), is an orchestrated extracellular sequence of events under rigorous genetic control (Simmer and Hu, 2001). The epithelial process is triggered and managed by ameloblasts, cells that are responsible for the secretion of the enamel matrix which consists of a group of proteins which regulate the nucleation, growth and organisation of mineral crystallites (Margolis et al., 2006). Ameloblasts become fully functional when they differentiate after the first layer of dentine has formed by odontoblasts and are lost as the tooth erupts into the oral cavity (Ten Cate, 1989). Within its life cycle, the ameloblast phenotype changes to reflect its primary role at the different stages of enamel formation.

The phase of amelogenesis during which mineralisation occurs is divided into three main stages: secretion, transition and maturation. During the secretory stage, columnar shaped ameloblasts secrete a protein-rich, partially mineralised, self-organising enamel matrix through the Tomes' process (a cone shaped region at the distal end of the ameloblast) (El-Sayed et al., 2010). The enamel matrix is composed predominantly (90%) of amelogenin (Fincham et al., 1999), a protein encoded by the AMELX gene, which assembles into nanospheres, about 20 nm in diameter, to regulate crystal spacing and support elongation along the *c*-axis (Fincham and Simmer, 2007). The rest of the matrix contains a small portion of ameloblastin, a cell adhesion molecule that facilitates the attachment of ameloblast to the enamel matrix (Margolis et al., 2006) and enamelin (encoded by the ENAM gene), suggested to aid crystal elongation (Hu et al., 1997, Hu et al., 2000). Additionally, MMP20 is expressed by ameloblasts throughout the secretory stage and into

early maturation to ensure correct processing of the matrix proteins. The proteins create a mineralisation front, migrating away from the Tomes' process to allow crystal growth. The orientation of the HA crystallites is governed by the angulation of the Tomes' process, as crystallites form perpendicular to the surface of Tomes' process. HA crystallites elongate into ribbons in circadian cycle leaving incremental lines corresponding to the daily increases in the enamel layer. The final length of the enamel crystal is determined by the duration the ameloblast continue to add proteins.

Upon entering the transition stage, ameloblasts shrink in size, reduce the secretion of enamel proteins and commence secretion of the proteases kalikren 4 (KLK 4) for degradation of the organic matrix. The maturation stage of enamel formation is characterised by the removal of the organic matrix, which terminates crystallite growth in length, and accelerates growth in width and thickness to generate the mature enamel. During this stage HA crystallites are organised in the bulk and the fully formed enamel layer is hardened, producing a mature acellular tissue (Simmer and Fincham, 1995, Hu et al., 2007).

Changes in the environment at any stage of the enamel formation leads to defects in the resultant enamel. With increasing age enamel tends to get progressively weaker and worn in regions of masticatory attrition (Nanci and Ten Cate, 2008). Though there are many other factors that can disrupt enamel formation, such as febrile disease, tetracycline induced disturbance and increased fluoride (Nanci and Ten Cate, 2003), the studies in this report will only concentrate on the implications on enamel structure due to genetic dysplasia and caries. Ameloblast proteins are very sensitive to environmental change. Changes due to mutations coding sequence of the proteins associated with amelogenesis can alter enamel formation. Furthermore, changes in the oral environment can lead to enamel disruption causing demineralisation and caries. The highly organised nature of enamel can be affected in two ways, during development, due to mutations (AI) or once fully formed, as a result of environment factors (caries).

The significance of studying the effects of genetic mutations on enamel structure is to determine the precise role that each protein plays at every stage of biomineralisation.

Studying the effects of caries on enamel structure can provide an insight into how the prisms are disrupted by the environment.

2.5 Amelogenesis Imperfecta

Amelogenesis Imperfecta (AI) is a genetically and clinically heterogeneous group of inherited conditions typically characterised by the alteration of the quantity and/or quality of enamel. It is a rare disorder, with an average prevalence of 1 in 500 worldwide (Darling, 1956), but in certain locations is present with greater frequency. Defects can be seen in both primary and permanent dentition (Aldred et al., 2003, Crawford et al., 2007). It is known to disrupt the correct formation of HA crystallites during the biomineralisation of enamel, which ultimately can affect the structure and clinical appearance of teeth (Crawford et al., 2007). AI brings with it three types of macroscopic defects in the enamel hypoplasia, hypomaturation and hypocalcification. Inheritance patterns for AI include autosomal dominant, autosomal recessive, X-linked and sporadic modes of inheritance. Mutations of various genes encoding proteins associated with AI have been found to be the cause of this disease, these include AMELX, ENAM, KLK 4 and MMP20 (Crawford et al., 2007). So far 14 subtypes of AI have been recognised based on the clinical phenotype and the mode of inheritance (Crawford et al., 2007). The diversity of enamel malformations observed in AI is believed to reflect the differences in the timing during Amelogenesis, when the disruptions occur (Darling, 1956).

The phenotype of AI shows a spectrum of clinical variability, it is dependent on the pattern of inheritance, the mutation, and expression of the protein and biochemical changes. Generally, in its mildest form AI displays discolouration and abnormal morphology of the clinical dental crowns and in its most severe presentation the enamel is hypomineralised causing it to be abraded from the teeth shortly after emergence into the oral cavity (Aldred et al., 2003, Crawford et al., 2007). This type of enamel defect holds many problems; it can be soft or brittle meaning that restorative dentistry tends to be quite difficult.

Though there are different types of AI with ranging severities, all have shown to have a negative effect on patient's day to day life. The effects of Amelogenesis Imperfecta can have a psychosocial impact on people affected by this developmental defect, such that there

are much higher levels of social avoidance, distress and discomfort in comparison to those without AI. The clinical implication spans out beyond disrupted enamel and can affect overall health (Coffield et al., 2005).

The most recent AI classification system is based on four areas (Gadhia 2012):

- Mode of inheritance: autosomal dominant, autosomal recessive, X-linked, isolated case
- Molecular basis: chromosomal localisation/locus/mutation
- Biochemical outcome: putative result of mutation when known
- Phenotype: hypoplastic, hypocalcified, hypomaturation, hypomaturation and hypoplastic with taurodontism

2.5.1 Hypoplasia

Hypoplasia is the subtype of AI which clinically manifests as enamel of abnormal thickness, with the presence of grooves and pits. It is a secretory stage defect resulting in insufficient crystal elongation and leaves the enamel pathologically thin.

Mutations in the *AMELX* and *ENAM* gene have shown to cause enamel hypoplasia, different phenotypes are associated depending on the location of the mutation within the gene. Phenotype can vary from smooth, local and generalised hypoplasia.

Enamalin is one class of proteins that plays an active role in the development of the enamel matrix during amelogenesis (Hu and Yamakoshi, 2003). In a specific case, a mutation in the ENAM gene has been identified as the cause of local hypoplastic autosomal dominant AI in families from northern Sweden (Mardh et al., 2002) where a scanning electron microscopy study has shown disrupted prism morphologies in these enamel specimens (Shore et al., 2010). A major clinical concern is the underdiagnoses of ENAM mutated AI teeth, as enamel can appear to be normal at the surface, yet microstructural analysis indicate defects can occur beneath the surface. Sections of affected deciduous teeth were ascribed a number based on clinical standards, whereby they did not seem to be too severe. However further analysis using SEM indicated irregular arrangement of crystals within the prisms with boundaries which could not be differentiated from one to the adjacent. These

characteristics gave a glass like appearance due to the fusion of crystals (Shore et al., 2010). Severity varies not only from tooth to tooth, but also from different regions intra tooth (Shore et al., 2010). We now wish to study the effect of the ENAM mutation on the crystallite organisation in affected enamel in order to better understand the role of enamelin during amelogenesis. This study is presented in chapter 7.

One approach in observing the severity and the extent of disruption in enamel affected by AI is to measure the micro hardness and microstructural characteristics, however to date only one mechanical study has been conducted on deciduous enamel (Pavlic et al., 2007). When compared to healthy control enamel, the micro hardness of pitted hypoplastic enamel was lower overall, with a substantial drop at the EDJ. Smooth hypoplastic AI enamel was extremely thin and soft. Hypomature enamel showed fluctuating hardness values, whilst hypocalcified enamel resembled values of dentin. Through the testing of different types of AI a variety of microstructural changes were measured, from changes in orientation to lack of normal prismatic structure and severe porosity.

2.5.2 Hypomaturation

The characteristics exhibited by hypomature enamel are of normal thickness but mottled in appearance and pathologically softer than normal and vulnerable to tooth wear. The hypomature subtype of AI is a result of maturation stage defects, if the enamel matrix is not properly degraded or resorbed.

AMELX can result in abnormal maturation and mineralisation defects, KLK4 and MMP20 show defects in the final crystallite mineralisation or maturation of the enamel.

Little is known about the hypomaturation subtype of AI. We there wish to charactise the structural properties of clinically diagnosed hypomature AI enamel (Chapter 8).

2.5.3 Hypocalcification

Hypocalcified enamel is representative of defective calcification, as with the hypomature subtype, this too presents enamel of normal thickness which is soft and structurally weak. It appears opaque and chalky in colour; teeth become stained and rapidly wear down. It is a

result of a mutation in the FAM83H. Amelogenin null mouse exhibits a dramatic enamel phenotype, which is manifested by a thin of mineral lacking a typical rod pattern (Gibson et al., 2001). The MMP20 null mouse exhibits severely abnormal tooth phenotype, with an altered rod pattern and hypoplastic enamel that delaminates from the dentine (Beniash et al., 2006). ENAM mutation exhibited severe phenotypic autosomal dominant Amelogenesis imperfecta (Hart et al., 2003, Hu and Yamakoshi, 2003).

2.6 Caries

Dental caries can be defined as a disease of the calcified tissue essentially caused by chemical imbalances in the oral environment. It is the most prevalent disease encountered worldwide, affecting both children and adults of all ages, causing considerable pain and discomfort as well as loss of function and the need for costly restoration (Tang et al., 2005, Robinson et al., 2000). The caries process involves constant cycles of destruction through demineralisation and restoration by remineralisation, with demineralisation ultimately dominating the process. If the surface of the enamel remains intact and the bacterial infection is removed, remineralisation predominates with restoration of enamel integrity (Nanci and Ten Cate, 2008).

Clinicians are faced with the problem of caries on a daily basis, ranging in severity, from minor (where a better oral hygiene regimen is needed) to extremely severe, whereby the bacterial infection progresses through the enamel in to the dentine and therefore major restoration or even tooth extraction is necessary. Caries is clinically identified as a white opaque spot; however, an important characteristic of the early caries lesion is that most of the demineralisation occurs at the subsurface level, with a well mineralised surface layer enclosing the lesion (Darling and Darling, 1982).

2.6.1 Demineralisation

Demineralisation occurs when the pH in the mouth drops below the critical value (usually pH 4). This can be caused by acidic food or drink consumption or when bacteria in plaque metabolise carbohydrate and produce acid. A fall in bacterial pH gradually dissolves mineral underlying dental tissue. Dissolution increases tissue porosity and the carious

lesion begins to form. Loss of ions from the crystal structure distorts the lattices destabilising the overall structural scaffold. Dissolution is more likely to occur at the prism boundaries and the progresses to the prism interior via the cross striations. As the periphery of the prisms has lower crystal packing and thus allows the acid to diffuse into the tissue (Darling, 1961).

The natural caries lesion in enamel exhibits four zones, identified by optical birefringence to polarised light microscopy (Darling, 1961). The surface zone is an intact unaffected layer, with a thickness in the range of 35 to 130 µm (Cochrane et al., 2012). It is believed that this layer remains intact as Ca^{2+} and PO_4^{3-} ions from saliva are deposited at the surface. Zone 2, the body of the lesion, displays a substantial mineral loss (approx. 24 %) and morphological changes in the crystal (Nanci and Ten Cate, 2008). The dark zone exhibits mineral loss of about 6 % and is characterised by enlargement of pores (Silverstone, 1967); the translucent zone (mineral loss of 1 %) is the deepest zone and represents the advancing front of enamel lesion. Pores or voids form along the enamel prism boundaries as the outer crystals dissolve due to the ease of hydrogen ion penetration during the carious process (Johnson, 1967, Boyde, 1989).

High resolution TEM images identified the initiation of dissolution by formation of holes at the surface core of the crystal which rapidly progresses along the *c*-axis due to the presence of dislocations (Tohda et al., 1987, Voegel and Frank, 1977, Yanagisawa and Miake, 2003). Gradual dissolution continues along the a and b axes by the removal of unit cells, causing defects in the lateral surfaces, which fuse to open the central perforations.

2.6.2 Remineralisation

Mineral lost during enamel demineralisation can be restored biochemically by a subsequent increase in the pH of the oral environment. Salivary buffering causes the pH to rise to the point when any carious destruction of the underlying tissue ceases (remineralisation). Saliva is rich in Ca^{2+} and PO_4^{3-} ions which are deposited in the carious lesion to repair the damages.

Remineralisation of enamel occurs by precipitation, growth of partially dissolved crystal or the formation of new crystals (Darling, 1997). It is believed that non-cavitated enamel lesions retain most of their original crystalline framework of the enamel rods and the etched crystallites serve as nucleating agents for remineralisation (Metser et al., 2014).
Primary teeth are more vulnerable to caries than permanent teeth. This is because permanent enamel undergoes post eruptive maturation, accumulating fluoride, becoming harder, less porous and less caries prone.

Acids produced by the plaque adhering to the enamel surfaces diffuse in the enamel and react with the mineral to release calcium and phosphate ions. Consequently the soluble ions are understood to diffuse out of the enamel leaving a porous structure (Christoffersen and Arends, 1982).

2.7 Enamel chemistry

As mentioned in section 1.2, the HA crystal structure properties can be altered by incorporation of ions during tooth development or by interaction with the surrounding environment post tooth eruption.

Variations in the lattice parameters as a function of position are indicative of a change in crystal chemistry (Al-Jawad et al., 2007). Carbonate content typically increases from enamel surface (1 wt %) to EDJ where it reaches 4 wt %, by substitution for phosphate and hydroxyl ions (Robinson et al., 1995). This is most likely due to the metabolic activity of cells during enamel formation (Robinson et al., 1995). High carbonate content increases solubility and thus makes enamel more prone to dissolution. However, if the hydroxyl ions are instead replaced by a smaller sized ion such as Fluoride (high electronegativity and symmetrical charge distribution), the structure becomes more stable against dissolution. Fluoride in mature enamel is present in high concentration near the surface due to fluorine present in toothpastes and dentifrices. This not only prevents demineralisation but promotes remineralisation (Robinson et al., 2000), whilst magnesium will replace calcium leading to less stable and therefore more soluble crystals, facilitating demineralisation.

2.8 Enamel Microhardenss

In addition to the hierarchical structure and chemical heterogeneity of enamel, the spatial inhomogeneity of enamel is evident also from variation in its mechanical properties as a function of position. Dental enamel is a hard material and exhibits high elasticity as an effect of the large number of crystallites. The hierarchical organisation of the HA crystals and chemical composition contribute towards the outstanding physical properties, mechanical strength and resistance to wear (Low et al., 2008). Methods including, compressive testing, Vickers indentation and nano indentation have been applied to human enamel samples in order to test determine the strength of this mineralised tissue. A decrease in Hardness (*H*) and Young's modulus (*E*) is apparent not only from enamel surface to EDJ but between buccal and lingual surface of permanent human molar teeth, as a result of changes in crystal chemistry rather than prism alignment (Cuy et al., 2002, Braly et al., 2007). This idea was opposing the conclusion drawn by (Habelitz et al., 2001), who found *H* and *E* to be a function of microstructural texture. A difference in the measurement taken parallel and perpendicular to the axis of the enamel prism, *H* and *E* were lower in the tail region and the interprismatic region, where crystal orientation deviates the most (Thewlis, 1940), than the prism head (Habelitz et al., 2001).

Hypomineralised enamel has an increased protein content in comparison to sound enamel which results in lower hardness and modulus of elasticity of hypomineralised (Xie et al., 2007, Xie et al., 2009) enamel (0.53 ± 0.31 and 14.49 ± 7.56 GPa, respectively) than normal enamel (3.66 ± 0.75 and 75.57 ± 9.98 GPa respectively) (Mahoney et al., 2004). SEM images corresponding to the hypomineralised regions revealed disorganised enamel with poorly demarcated prism boundaries (Mahoney et al., 2004).

Overall, microhardness of AI (pitted and smooth hypoplastic) affected enamel is much lower than healthy enamel. Hypomature and hypocalcified enamel can even be as soft as dentine (Pavlic et al., 2007). Microstructural changes varied from altered orientation of enamel prisms in pitted hypoplastic AI to lack of normal prismatic structure and severe porosity in hypocalcified AI (Pavlic et al., 2007).

2.9 Enamel structure summary

Enamel is a highly mineralised material with an intricate microstructure. The structural properties and strength can become comprised through genetic factors during formation or through environmental influences post eruption. These properties can be studied using X-ray techniques which are described in Chapters 3 and 4.

Chapter 3: X-ray Scattering Methods

The studies presented in this thesis have used a combination of X-ray techniques to measure microstructural and crystallographic features of different enamel samples. A theoretical description of X-ray scattering and absorption is given in chapter 2 and 3 respectively.

3.1 X-rays

Since their discovery by Röntgen in 1895, X-rays have been used extensively to investigate a wide range of medical, industrial and scientific problems, as well as in food and cosmetics. X-ray techniques have revolutionised research as they can reveal internal information about the material, such as structure, chemical composition, and physical properties at several length-scales from $1x10^{-3}$ to $1x10^{-10}$ metres.

X-rays are photons, and belong to the high frequency end of the electromagnetic spectrum (Seibert, 2004). The electromagnetic spectrum is the complete range of wavelengths (the distance between successive crests of the travelling wave) of electromagnetic radiation (photons). It ranges from long wavelength radio waves (low frequency end), to short wavelength gamma rays (high frequency end). X-rays display short wavelengths in the region of 0.1 and 100 Ångstrom (Å) (10^{-10} m), with energies in the range of 100 eV-100 keV. X-rays selected for diffraction studies lie approximately in the range 0.5 to 2.5 Å, as it corresponds to chemical bond distances and repeat distances in a crystal (Cullity, 1978).
As X-ray travel through matter they interact with the atoms and are scattered. The energy of X-rays can be calculated using the following equation:

$$E = \frac{h\,c}{\lambda}$$

Equation 3.1

Where *h* is Planck's constant,

c is the speed of light,

λ is the wavelength.

The energy E (the penetrating power), of X-rays required for a study is given by the reciprocal of the wavelength λ:

$$E\ (keV) = \frac{12.4}{\lambda\ (\text{Å})}$$

Equation 3.2

Thus X-rays have a greater penetrating power when they have shorter wavelength, higher energy.

3.2 X-ray interactions with matter

X-ray photons directed at the sample interact with its atoms, causing the energy of the photons (initial intensity of the incident beam) to be absorbed or scattered. X-rays are said to be attenuated when intensity is lost in this manner. The extent of attenuation is dependent on:

- The energy of the X-rays
- The density of the material
- The atomic number of elements that make up the material

The physical mechanisms by which photons interact with the atom and are responsible for the attenuation of X-rays include:

Photoelectric absorption

This occurs when an incident X-ray photon is absorbed by the transfer of its energy to the inner orbital electron of the atom. The electron becomes excited and is ejected, leaving a vacant inner electron orbit, to be filled by electrons from the outer orbit. This emits a characteristic photon, with low energy. The photoelectric mechanism is dominant for low X-ray energies.

Compton scattering

When the energy from the incoming photon is greater than that of the binding energy (energy required to remove the electron from the atom) of the electron, interactions occur with the outer orbital electrons, ejecting them and losing only part of its own energy, after which, the incident photon is deflected and scattered in all different direction (inelastic scattering).

Pair production

This mechanism requires high energy X-ray photons (> 1.02 MeV), therefore does not occur when using impact sources. The photon interacts with the nucleus of the atom, which transforms it into a positron-electron pair. Energy is converted into mass, with any excess photon energy transferred into kinetic energy in the particles produced.

Thomson scattering

This is also known as simple or coherent scattering, it occurs when the incident photon energy is much lower than the electron binding energy (< 30 keV). The X-ray photon interacts with the whole atom and is purely deflected without any loss of energy (elastic scattering).

3.3 X-ray Production

X-rays are generated by electronic transitions involving highly energised charged particles such as electrons. A monochromatic source produces radiation with one wavelength; alternatively a source producing a wide range of wavelengths produces polychromatic light. X-rays are produced by a conventional X-ray tube or by synchrotron radiation.

3.3.1 Laboratory sources

An X-ray tube (Fig. 3.1) is generally the source of X-rays in research laboratories. X-rays are generated when high speed electrons strike a metal target. Within the glass tube electrons are liberated from the negatively charged cathode emitter and accelerated in the electric field between the anode and the cathode towards the positively charged anode target (typically a piece of tungsten). The high speed electrons collide with the atoms and

nuclei of the metal target and rapidly decelerate, emitting a continuous spectrum of X-rays. In this way, two atomic processes produce the X-rays:

1. Bremsstrahalung: A German term which translates to 'breaking radiation.' X-rays are produced by the sudden deceleration and deflection of electrons by the electric field surrounding the atomic nuclei. Energy is lost as electrons scatter, which radiates as X-rays, producing a continuous spectrum which becomes more intense and shifts toward higher frequencies when the energy of the accelerated particles is increased.

2. Characteristic: Increase in the voltage of an X-ray tube above the critical value of the target metal cause a sharp intensity maxima to appear at certain wavelengths, superimposed on the continuous spectra. Electrons from a higher atomic level drop to the vacant level with the emission of an X-ray photon characterised by the difference in energy between the two levels. Each element has a unique set of energy levels, and thus the transition from higher to lower energy levels produces X-rays with frequencies that are characteristic to each element. The X-rays produced by transitions from the L shell (n=2) to the K shell (n=1) levels are known as K-alpha X-rays, and transition from M shell (n=3) to the K shell are called K-beta X-rays. This produces monoenergetic X-rays which are of greater intensity than the X-ray photons released by Bremsstrahlung. In the laboratory a copper X-ray tube source produces X-rays with a wavelength of 1.54 Å.

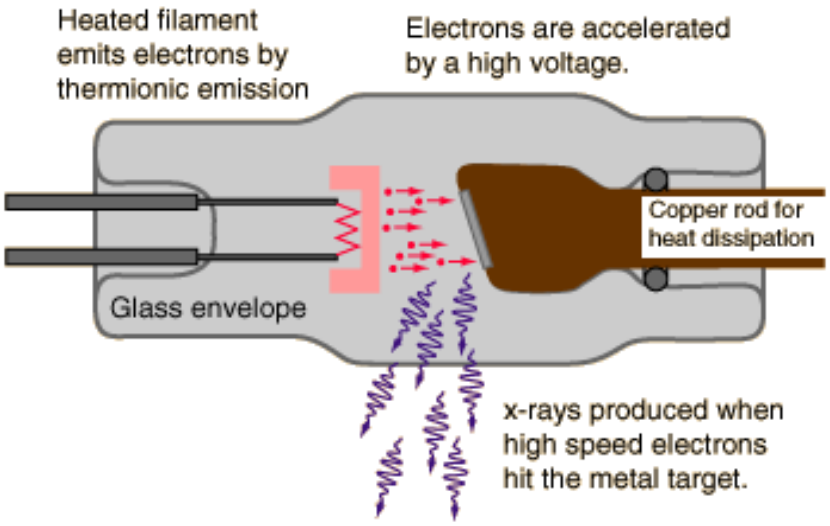

Figure 3.1: Schematic representation of an X-ray tube. X-rays are produced in research laboratories by the interaction of energetic electrons with a metal target.

(Image taken from http://hyperphysics.phy-astr.gsu.edu/hbase/quantum/xtube.html)

3.3.2 Synchrotron sources

Synchrotron facilities cater for research in a wide range of disciplines, including, material science, physics, chemistry and biomaterials, food science and, pharmaceuticals. There are currently 70 synchrotron light sources worldwide, each with varying energy levels and number of beamlines. These facilities offer a flux, energy range and resolution unachievable with conventional (laboratory) radiation sources. The three most powerful third generation sources include the European Synchrotron Radiation Facility (ESRF, Grenoble), the Advanced Photon Source (APS, Illinois) and the Super Photon Ring 8GeV (SPring-8, Japan). The Diamond Light Source (DLS, UK) is also a third generation synchrotron, with medium energy range. The X-ray diffraction studies carried out for this thesis were performed at the ESRF, APS and DLS. Detailed descriptions of the specific beamlines and setups are given in Chapter 6 (Materials and Methods).

Synchrotron radiation was discovered in 1947. A synchrotron (Fig. 3.2) is a system of particle accelerators that use electromagnetic fields to accelerate (near to the speed of light)

and guide charged particles around a circular track in a storage ring. When accelerated particles are deflected, normally to the orbit by a magnetic field, they emit bright synchrotron light. Bunches of electrons are generated in the electron gun and directed into the linear accelerator (LINAC), before entering the booster ring where they are accelerated to near the speed of light. Electrons are injected into the storage ring, where they are further accelerated and maintained in orbit through strong electromagnetic fields.

$$\lambda_c = \frac{18.6}{BE^2}$$

Equation 3.3

Where B is the magnetic field

E is the electron energy (GeV)

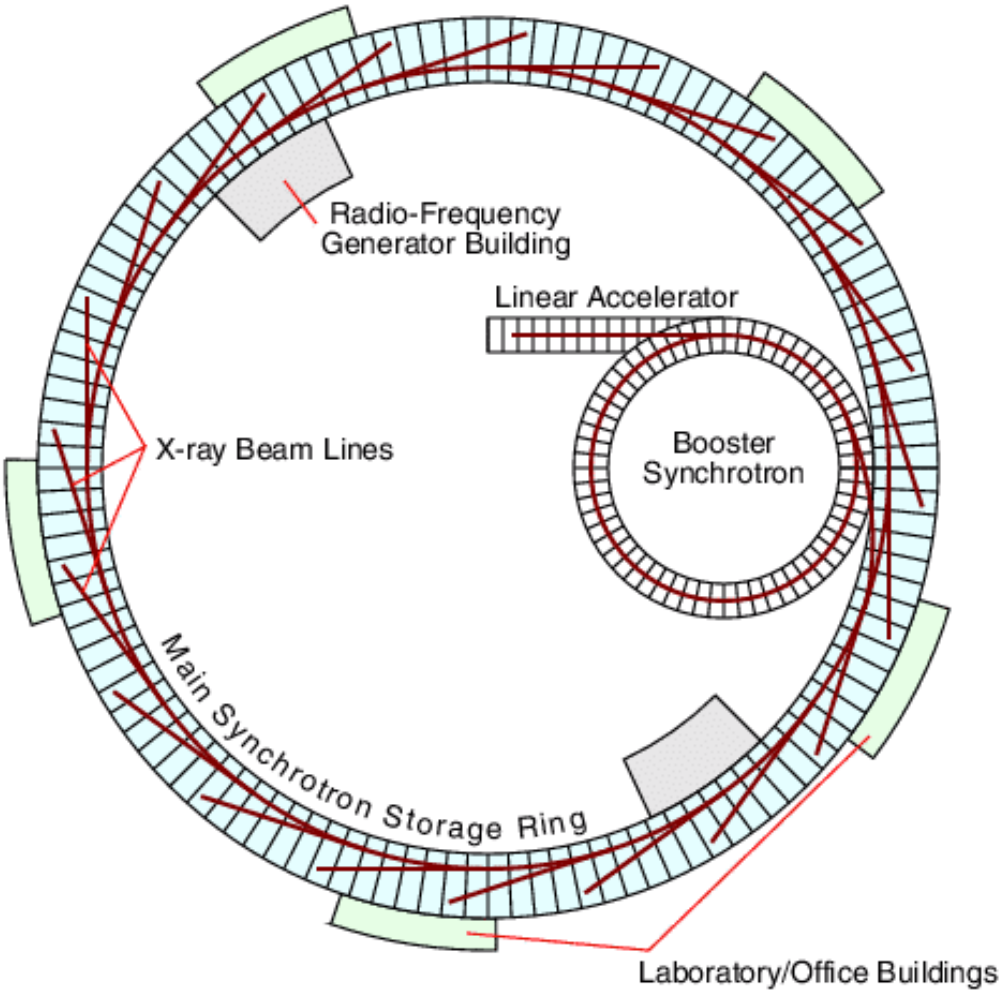

Figure 3.2: Schematic representation of a synchrotron radiation system.

(Image taken from http://pd.chem.ucl.ac.uk/pdnn/inst2/work.htm)

Radiation is emitted whenever the relativistically moving electrons are forced to deviate from a straight line motion. This is usually done by applying magnet fields, bending magnet (BM) and insertion device (ID) (Fig. 3.3a), which are located in the straight regions of the orbit. The dipole magnets serve the purpose of further enhancing radiation intensity as well as tuning the X-rays to the requirements of the beamline. Each beamline is designed to carry out specific experimental techniques.

Bending magnets are dipole magnets which are used to curve the electron beam around the storage ring. As the electron beam passes through the BM (Fig. 3.3b), energy is lost in the form of light; it produces a very stable beam over a broad spectrum.

There are two types of insertion devices, comprised of rows of magnets with alternating polarity, wigglers (Fig. 3.3c) and undulators (Fig. 3.3d) (names based on the motion of electrons through the magnetic field). Wigglers act as a wavelength shifter, shortening the wavelength to increase the X-ray energy and thus penetrating potential. The simplest wiggler is comprised of three magnets (alternating poles), as the electrons pass through the electromagnetic field, they digress in and out from the original path causing them to "wiggle" with a large deviation angle. This produces highly energised photons emitting bright and spectrally continuous light with and greater radial acceleration. Most scientific experiments require a very narrow range of wavelengths and therefore most of the wiggler radiation power remains unused leading to unwanted heat production within the optical devices.

Undulators are much larger, consisting of typically 20-30 alternating low field magnetic poles which cause undulations (a fluctuating series of inward and outward electron accelerations) with small deviation angles, producing a bright narrow beam a continuous frequency range. Emissions at each individual pole overlap and interfere (constructively or destructively) downstream from the undulator. By varying the separation of the magnet arrays, it is possible to tune the undulator and choose the energy that is generated.

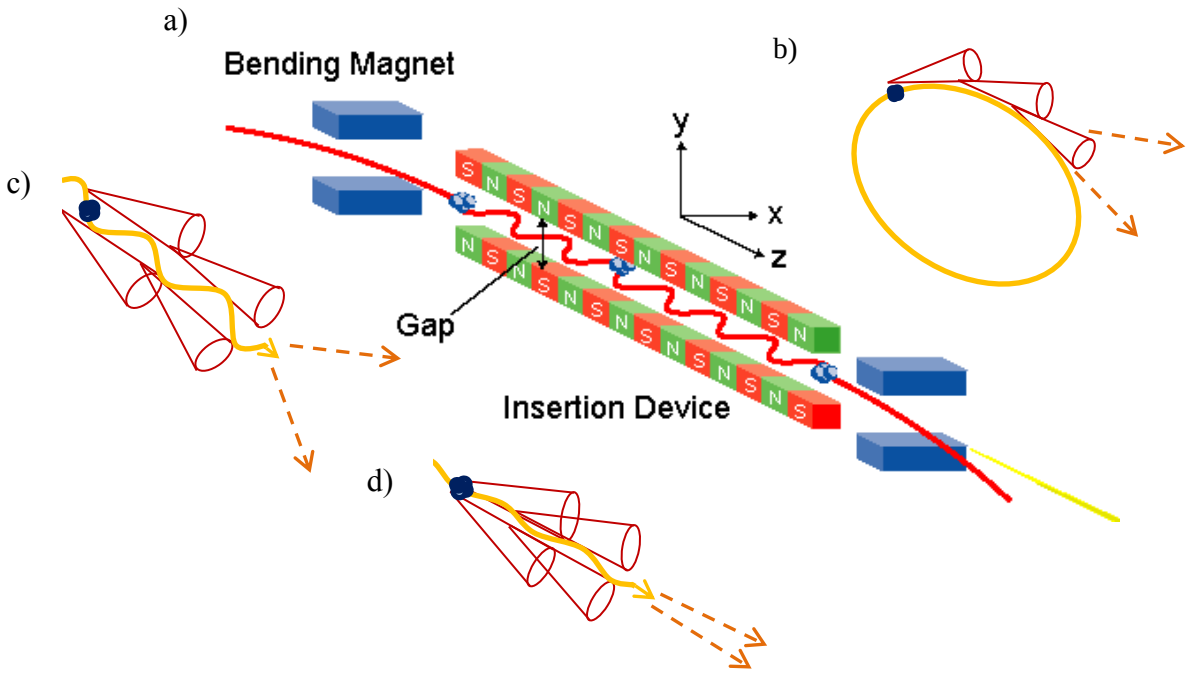

Figure 3.3: Schematic representations of the a) overall bending magnet and insertion device placed in the storage ring of the synchrotron and the radiation cones generated by the b) bending magnet c) wiggler and d) undulator.

(Image a) taken from http://www.spring8.or.jp/en/facilities/bl/light_source_optics/sources/insertion_device/whats_insertion_device)

Synchrotron radiation provides an extremely intense (x10^{12} more than laboratory X-ray tubes), highly collimated, continuous energy spectrum with high a photon flux. The high energy beams allow deeper penetration into the matter and the small wavelengths permits studying small features. Furthermore the beam size and optics can be modified to each specific experiment. Such characteristics allow rapid collection of high quality data sets.

Such advantages mean that synchrotron facilities have an extremely high demand of users; beam time can only be awarded to successful research proposals, which go through a

rigorous and competitive peer review process. Allocated time at such facilities is very limited, which can restrict the number of samples measured and experimental repeats. Exposure to high energy can cause sensitive samples, such as soft tissues, to suffer from radiation damage. Continuous upgrades and advancement to the beamline and general use by different research groups makes setup difficult to reproduce to match that of a previous experiment. Furthermore, travelling time (and in some instances, costs) need to be taken into consideration, as such facilities are not as easily accessible.

3.4 X-ray diffraction

X-ray diffraction is a powerful technique used to probe the structural arrangement of atoms and molecules in crystalline materials. The discovery was made by Laue in 1912 using a single crystal of Copper Sulphate Hydrate. Laue deduced, crystals composed of regularly spaced atoms act as scattering centres for X-rays, if electromagnetic waves of wavelength are equal to the interatomic distance in crystals, then it should diffract X-rays by means of crystals.

The X-ray diffraction technique uses short wavelength X-rays, on the order of a few angstroms, as it is used to probe features on the atomic length-scales. X-ray diffraction can determine the chemical composition and phase composition of a crystalline material, the texture (preferred orientation of crystallites), the crystallite size and presence of strain.
Wide-angle X-ray scattering (WAXS) and small-angle X-ray scattering (SAXS) are two ways of carrying out diffraction experiments (Fig. 3.4) which essentially work on the same principle. The main difference between WAXS and SAXS is the sample to detector distance, the former has a shorter distance (average distance) and thus diffraction maxima at greater angles are observed, whereas the detector in the latter is placed at a further distance (average distance) to the sample and records information at very low angles (in the range of 0.1 - 10°). In general WAXS is used to observe wide-angle scattering arising from lattice planes in crystalline materials, whereas SAXS is used for studying larger features such as grain sizes or inter-grain spacing (if dilute system) in both crystalline and non-crystalline materials.

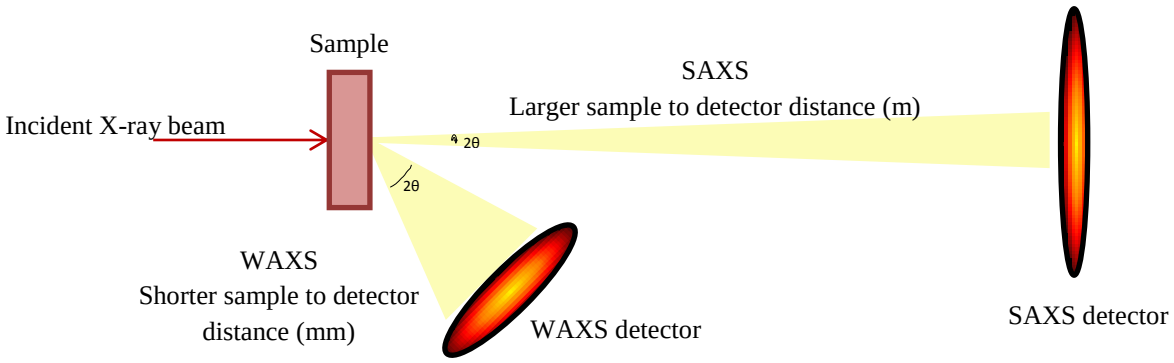

Figure 3.4: Schematic representation depicting the experimental set up for SAXS and WAXS, highlighting the difference in diffraction angle and sample to detector distance.

3.5 Bragg's Law

Crystal materials are three dimensional structures comprised of ordered atoms (spaced a distance, d apart) arranged in planes (determined by integers *hkl*), thus exhibit periodicity. Diffraction is the scattering of X-rays from successive planes in a crystal; when the distance between the atoms is of the same magnitude as the wavelength of the X-rays causing constructive interference.

Braggs law (Bragg, 1928) demonstrates that parallel rays of the incident beam on lattice planes (*hkl*) are scattered at angle θ so that the resultant reflections constitute coherent interference of the diffracted beam (Fig. 3.5). Diffraction is achieved only when the length sum of the incident X-ray (AB) is less than the length sum of reflecting X-ray (BC) from a plane of atoms inside the crystal, and the wavelength is of the same order of magnitude as the repeat distance between scattering centre.

$$AB + BC = 2d_{hkl} \sin\theta$$

Equation 3.4

Where $2d_{hkl}$ is the distance between successive lattice planes,

θ is half the scattered angle of incident beam with the lattice plane at which diffraction occurs.

Bragg's law is a simple mathematical model, based on Laue's experiment, expressing the necessary condition for X-ray diffraction.

$$n\lambda = 2d\ sin\ \theta$$

Equation 3.5

Where n is an integer,

λ is the wavelength of the X-rays,

d is the distance between atomic layers in a crystal,

θ is the incidence angle.

In powder diffraction, scattering of the diffracted beam from lattice planes of a polycrystalline material form continuous cones of intensity, known as Debye Scherrer cones. The direction of the diffracted beam can be used to determine the size and shape of the unit cell from an unknown crystal. The 2θ position of these cones defines the space d_{hkl} between diffracting atom planes *hkl* and the intensity defines the type of atoms present in the plane.

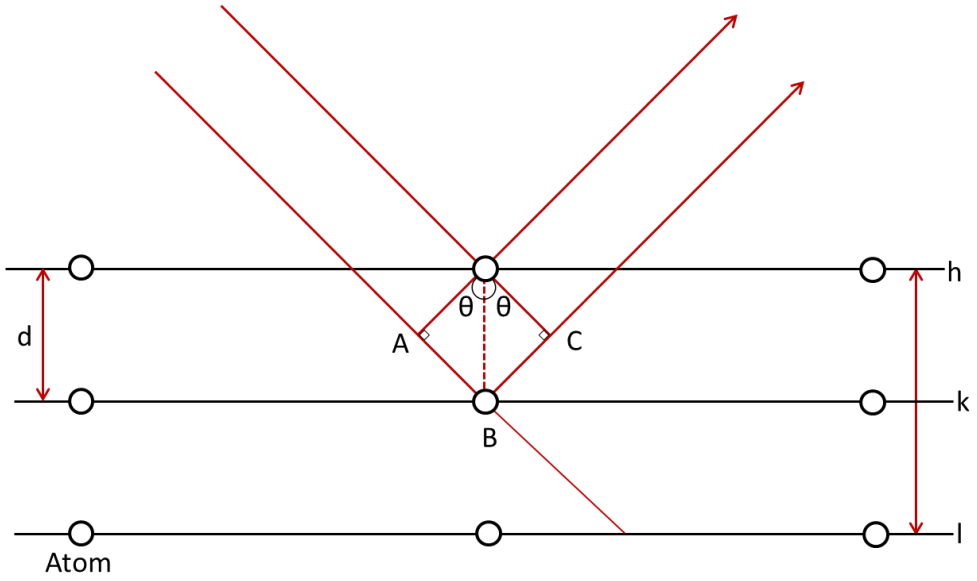

Figure 3.5: Simplified geometric construction to representing the conditions necessary for diffraction

3.6 Diffraction data analysis

Diffraction contains structural information about the crystal at the crystallographic level. Profile fitting is a precise method to determine diffraction peak position, integrated intensity, and broadening for calculating crystal chemistry, crystallite size and anisotropy.

3.6.1 Bragg Intensity

The intensity of a Bragg reflection, I_i^{calc} in the powder diffraction pattern can be calculated using the equation 3.6. The equation is derived of several experimental factors that affect I_i^{calc}, including the amount of phase present, the peak shape, the peak width, extinction and absorption coefficients, and preferred orientation effects.

$$I_i^{calc} = S_{ph} \sum_{hkl} L_{hkl} |F_{hkl}|^2 \phi(2\theta_i - 2\theta_{hkl}) O_{hkl} A + y_i^{back}$$

Equation 3.6

Where S_{ph} is the phase scale factor (used to adjust the relative contribution of individual phases to the overall diffraction pattern),

L_{hkl} is the multiplicity, Lorentz and polarisation factor (accounts for reciprocal space symmetry),

F_{hkl} is the structure factor (describes how the atomic arrangement of the crystal structure affects the scattered beam),

ϕ is the profile peak shape function (Gaussian, Lorentzian, Pseudo-Voight),

O_{hkl} is the preferred orientation function,

A is the absorption factor (corrects for the reduction in Bragg intensity due to the attenuation of X-rays passing through the sample),

y_i^{back} is the background intensity at point *i*.

3.6.2 Preferred orientation

The macroscopic mechanical properties of crystalline materials depend on the microscopic crystallite arrangement (Wcislak et al., 2002). Preferred orientation (O_{hkl}) can be defined as the orientation distribution (OD) of crystallites in a polycrystalline material. Randomly oriented crystallites lack texture (a crystallographic term used often alongside O_{hkl}), however when the crystallites in a sample are aligned in a preferential orientation along certain lattice planes then the material is said to have crystallographic texture. X-ray diffraction can be used to measure crystal arrangement, the direction and magnitude of crystal texture or preferred orientation in a material.

In this thesis, the degree of preferred orientation has been measured using the spherical harmonics model, based on the general axis equation (Equation 3.7) described by Bunge (1982). The preferred orientation correction (O_{hkl} from equation 3.6), essentially describes the change in Bragg intensity for a reflection due to texture and therefore depends on both the reflection, h, and on the sample orientation, y.

The spherical harmonics function is a complex, yet powerful method of measuring the pole density distributions of a number of diffraction planes.

$$O_{hkl} = 1 + \sum_{L=2}^{N_L} \frac{4\pi}{2L+1} \sum_{m=-L}^{L} \sum_{n=-L}^{L} C_L^{mn}\, k_L^m(h) k_L^n(y)$$

Equation 3.7

Where C_L^{mn} is an allowed harmonic coefficient,

$k_L^m(h)$ and $k_L^n(y)$ are harmonic terms, which take on values according to the crystal and sample symmetries, respectively

L is an integer

Thus the two inner summations are over only the resulting nonzero harmonic terms.

The magnitude of the texture can be evaluated from the texture index, J (Bunge, 1982).

$$J = 1 + \sum_{L=2}^{N_L} \frac{1}{2L+1} \sum_{m=-L}^{L} \sum_{n=-L}^{L} |C_L^{mn}|^2$$

Equation 3.8

If the texture is random then J = 1, otherwise J > 1; for a single crystal J = 0 (Matthies et al., 1988).

Equation 3.7, represent preferred orientation, using the spherical harmonics function. It is the complete function for O_{hkl}, including terms for crystal and sample symmetry. The texture index equation (Equation 3.8) includes a magnitude function within in it, Therefore texture is present when values are greater than one.

3.6.3 Particle Size analysis – peak widths

The Full Width at Half Maximum (FWHM) (Fig. 3.6) is a parameter commonly used to describe the width of a peak. It is given by the distance between points on the curve at which the function reaches half its maximum value. Equation 3.9 is the Guassian function, used to determine the FWHM.

$$y = y_0 + \frac{A}{w\sqrt{\pi/2}} e^{\frac{-2(x-x_c)^2}{w^2}}$$

Equation 3.9

Where x_c is the center,

w is the peak width

A is the area.

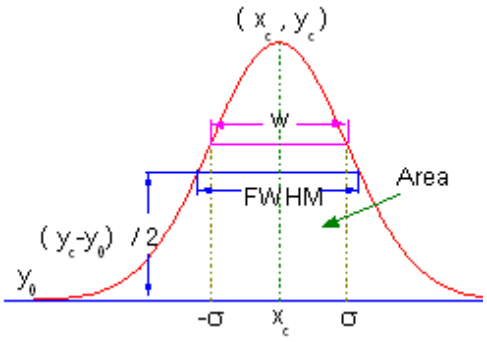

Figure 3.6: Graphical representation of the of the FWHM parameter

(Image taken from OriginLab®)

Sharp intense peaks are indicative of large crystal and broad peaks represent small crystals.

The Scherrer formulae (Patterson, 1939) (Equation 3.10) can be used to determine the average crystallite size (D).

$$D = \frac{K\lambda}{\beta \cos\theta}$$

Equation 3.10

Where *K* is a constant close to unity

λ is the wavelength

β is the FWHM of the peak

3.6.4 Rietveld refinement

Rietveld refinement is a quantitative phase analysis technique formulated by Hugo Rietveld in 1967, for use in the structural characterisation of crystalline materials (Young, 1993, Rietveld, 1988). The introduction of this method was a significant step forward in the analysis of powder diffraction data, as it was devised to overcome the problem that often occurs with powder diffraction of complex structures, overlapping reflections. For this method, each point in the diffraction pattern is treated as an individually observed intensity allowing an accurate determination of the structure. This is advantageous over conventional diffraction analysis that relies on individual diffraction peaks, particularly for low symmetry materials with many overlapping peaks and images with poor peak to background ratio (Lutterotti et al., 2007). The Rietveld method uses a least squares approach to refine a theoretical line profile until it matches the measured profile, it minimises the effect of variation in sample volume since all reflections are used to obtain a fit. Both, crystal structure of the material and instrument must be known to create a model of the expected reflections (McCusker et al., 1999).

The objective is to refine a model structure against a measured powder diffraction pattern (Fig. 3.7). Peak intensities provide the information about the crystal structure, peak positions provide unit cell information and peak widths and shape provide information on instrument and crystallinity of the sample. Figure 3.7 is an example of a typical 1D Intensity vs. 2θ diffraction pattern, where the crosses are the observed data points and the

solid line is the calculated profiles. The tick marks correspond to the to the 2θ peak position of the calculated diffraction pattern (in this case, hydroxyapatite), the difference pattern lies just beneath the tick marks.

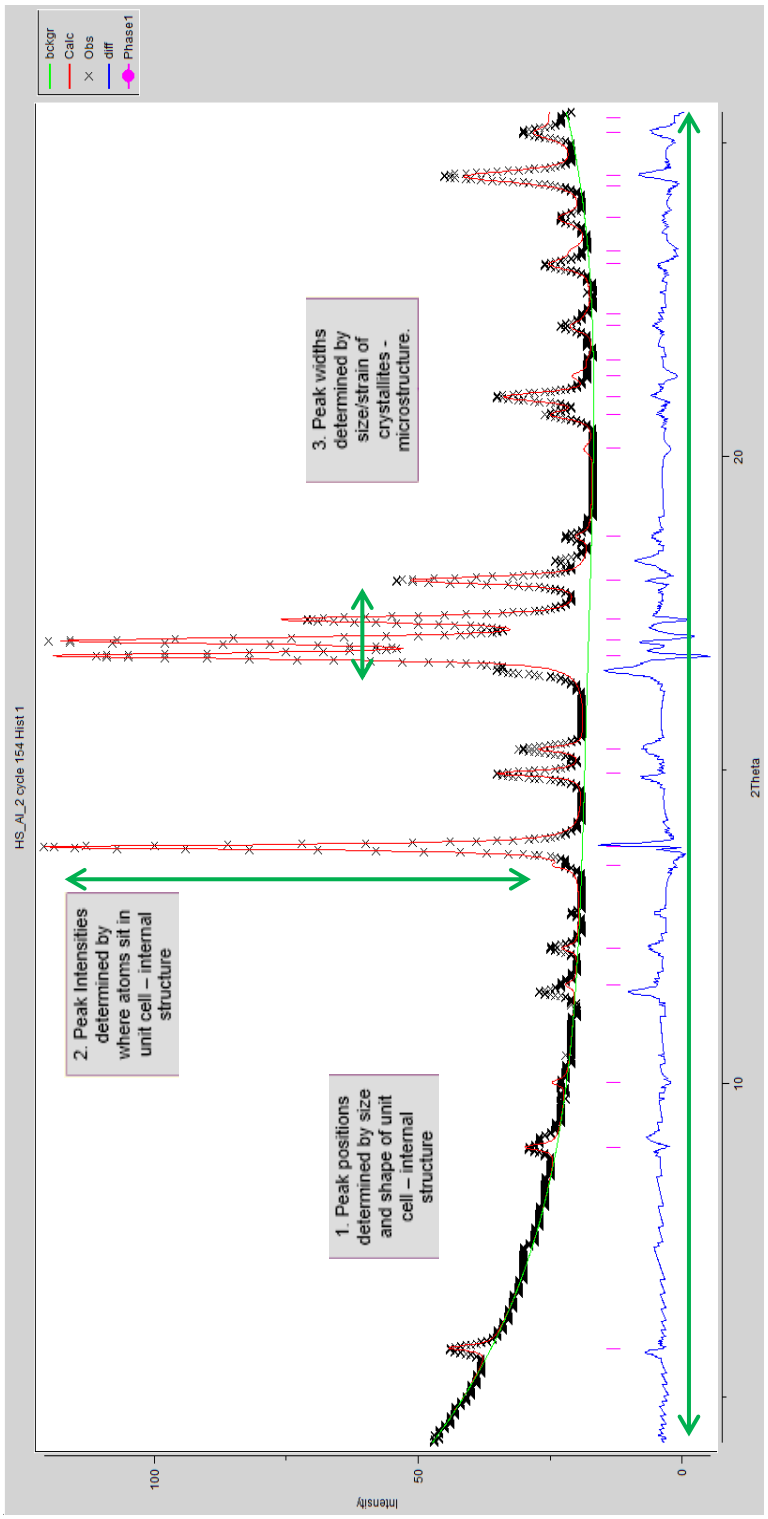

Figure 3.7: A typical Rietveld refinement indicating the type of information that can be extracted from a diffraction pattern.

The Rietveld refinement method is used to refine the structure from the powder diffraction data. Therefore the crystal structure of the sample must be known. The calculated model (I_i^{calc}) is refined iteratively against experimentally observed (I_i^{obs}) data to minimise the least-squares quantity and obtain a best fit, R, using the expression:

$$R = \sum_{i=1}^{N} \left[W_i (I_i^{obs} - I_i^{calc}) \right]^2$$

Equation 3.11

Where W_i is the weight attributed to each profile point, *i* (weighting of the data point and error), and is proportional to the square root of the count rate I_i^{obs}:

$$W_i = \frac{1}{\sqrt{I_i^{obs}}}$$

Equation 3.12

The intensity at each profile point in the diffraction pattern can be calculated by:

$$y_i^{calc} = y_i^{back} + \sum_{k=k_1}^{k=k_2} G_i^k \; I_i^k$$

Equation 3.13

Where y_i^{back} is the background (non-Bragg) intensity, calculated using Equation 3.14,

G_i^k is the normalised peak profile function (describes peak shape),

I_i^k is the Bragg intensity of reflection k,

k_1 and k_2 are the reflections contributing intensity to point *i*.

The background intensity (y_i^{back}) can be calculated using the following equation:

$$y_i^{back} = \sum_{n=0}^{N_b} a_n (2\theta_i)^n$$

Equation 3.14

Where N_b is the polynomial degree,

a_n is the polynomial coefficient.

The quality of the fit is calculated with reference to R-factors. Equation 3.15 describes the weighted profile R-profile, R_{wp}.

$$R_{wp} = \sqrt{\frac{\sum_{i=1}^{N}\left[W_i\left(I_i^{exp} - I_i^{calc}\right)\right]^2}{\sum_{i=1}^{N}\left[W_i I_i^{exp}\right]^2}}$$

Equation 3.15

Equation 3.16 describes the expected R-factor, R_{exp}.

$$R_{exp} = \sqrt{\frac{(N-P)}{\sum_{i=1}^{N}\left[W_i I_i^{exp}\right]^2}}$$

Equation 3.16

Where *N* is the number of observations (data points) and *P* is the number of parameters

The least-squares refinement parameter can be defined as:

$$X^2 = \left[\frac{R_{wp}}{R_{exp}}\right]^2$$

Equation 3.17

Therefore as X^2 approaches unity, the quality of the fit improves.

3.6.5 Phase analysis

The scale factor, S_{ph}, can be used for quantitative phase analysis of powder mixtures. It is proportional to the unit cell composition of the sample, and can be converted into weight fractions (W_p) using:

$$W_p = \frac{S_{ph} m_p}{\sum_{p=1}^{n} S_{ph} m_p}$$

Equation 3.18

Where S_{ph} is the phase fraction scale

m_p is the unit cell mass for phase p. This is computed from the atom site multiplicites and fractions present for that phase.

Chapter 4: X-Ray Absorption Methods and Scanning Electron Microscopy

4.1 Introduction

This chapter describes the physical theory involved for X-ray imaging. X-ray tomography (XMT) is a non-destructive technique which provides three dimensional information of materials at high resolution (Elliott and Dover, 1982). It can be best described as a miniaturised version of a computed tomography (CT) system, which was originally conceived by (Hounsfield, 1973). This technique has since been applied extensively across diverse range of disciplines to determine the internal structure and properties of materials.

4.1.1 Linear Attenuation Coefficients

Tomography measures a specimen's Linear Attenuation Coefficient (LAC). The LAC (μ) of an object being scanned is the logarithmic decrease in intensity of the transmitted radiation per unit length, typically expressed in units of cm^{-1}. Tomographic images can serve as maps of spatially varying LAC.

4.1.2 Beer's law

X-ray signals are exponentially attenuated as they are transmitted through the volume of the specimen; this relationship can be best described using Beer's law, which defines the basic attenuation equation for a monochromatic beam through a homogenous material. The transmitted intensity *I*, is given by:

$$I = I_0 e^{-\mu x}$$

Equation 4.1

Where I_0 = initial intensity of the beam

μ = Linear Attenuation coefficient

x = length of X-ray path through the material

4.2 History and development of computed tomography

Computed tomography has evolved considerably since the idea was initially conceived by Hounsfield and Cormack in 1973 (Hounsfield, 1973). Modern scanners generate high quality image data for complete volumes at an increased speed. This section gives an account of the development of the CT scanners

The first generation CT scanner used parallel beam geometry (Fig. 4.1a); samples were stepped through a collimated pencil beam to produce a single projection of X-ray attenuation across the sample volume. The system would rotate through a small angle and the process repeated. Although this method eliminated variations across the detector by using a single detector, it was time consuming, taking several hours to collect enough data for the reconstruction of only one slice.

Second generation scanners were developed to reduce data collection time by replacing the collimated pencil beam with a diverging partial fan beam to the translate-rotate geometry. The system was further developed to the third generation scanner, where the angle of the fan beam (Fig. 4.1b) was increased, eliminating the need for the translation steps and both source and detectors rotate simultaneously, which further reduced scan time.

The current system, the fourth generation CT scanner uses rotating fan beam with stationary detectors arranged in a complete circle surrounding the sample. Cone beam geometry (used extensively in dentistry) records 2D projections in order to acquire data for a complete 3D reconstruction in one rotation (Fig. 4.1c). This is the type normally used for desktop microtomography scanners (section 4.3) (Kalender 2006).

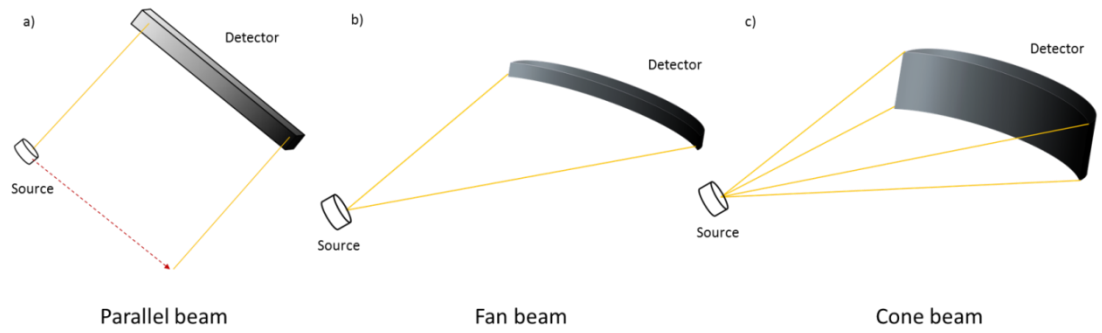

Figure 4.1: Schematic representation of tomography beam geometry a) parallel beam geometry, b) fan beam (wide angle) geometry and c) cone beam geometry (used in XMT systems for volumetric tomography.

4.3 Principles of microtomography

X-ray microtomography (XMT) is a miniaturised version of CT which follows the same fundamental principles as Hounsfield's medical CT scanner. This was developed by (Elliott and Dover, 1982) in order to output high quality images for accurate mineral quantification by analysis of the reconstructed LAC map. The technique provides three dimensional information of a material at micron resolution (Elliott and Dover, 1982) and is thus applied extensively across diverse range of disciplines to determine the internal structure and properties by virtually sectioning the sample into thin slices. The non-destructive and non-invasive nature of the tomography technique allows quantitative analysis by observing changes in the LAC (a measure of the sample atomic number and density).

Current XMT systems have a fixed X-ray source and detector, and instead the sample stage rotates. It makes use of cone beam geometry (Fig. 4.2) in order to get a three dimensional volumetric reconstruction of a sample instead of layered slices which are generated from pencil and fan beam geometries. As the sample rotates through 360°, the attenuation of the incident beam is recorded as radiographic images by an area detector array; this captures the transmitted fraction and converts the X-rays into a greyscale projection image (The grey level is directly linked to the attenuation). The resolution can be altered by changing the distance between the source and sample by altering the geometric magnification ratio. Data

collection time is faster using this method than with pencil beam or fan beam systems. A specialised back-projection algorithm is applied to reconstruct each image through the reconstructed volume to yield a true representation of the specimen.

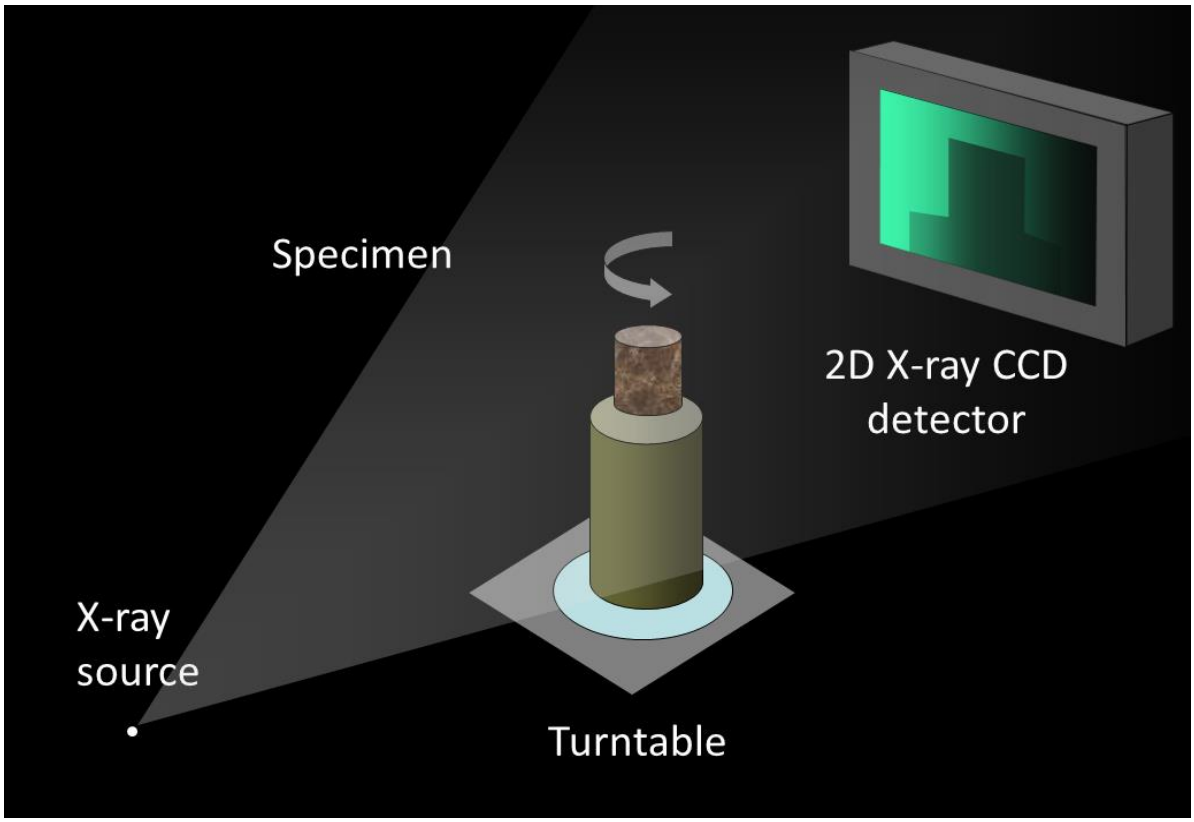

Figure 4.2: Schematic representation of cone beam geometry, used in current XMT system. (Wong et al., 2006).

4.4 Errors and artefacts

XMT is required to provide high quality data for structural analysis, both quantitative and qualitative, however due to the inaccessibility of synchrotron sources, conventional tomography is often used (Zou et al., 2011). A polychromatic source produces a spectrum of photon energies which can lead to errors and artefacts. It is important to minimise and eliminate these for accurate quantification. The most common errors are the presence of ring artefacts and beam hardening.

4.4.1 Ring artefacts

Ring artefacts are a result of variations in the X-ray sensitivities of adjacent detector elements. Artificial light or dark pixels always present in the same position on each projection and produce a ring like appearance in the reconstructed image. In order for this to be avoided, each element of the detector must be calibrated (Boas and Fleischmann, 2012).

4.4.2 Beam hardening

The X-ray beam from an impact source is a Bremsstrahlung spectrum, covering the entirety energy range. Beam hardening occurs when the proportion of higher energy photons in the transmitted beam increases due to the preferential attenuation of softer X-ray (Brooks and Di Chiro, 1976). A greater number of photons are absorbed at the surface of the specimen, whereas regions further away from the source (centre of the sample) will generally attenuate fewer photons by absorption (Davis et al., 2013). The extent of beam hardening varies according to the material attenuating the beam; materials with high atomic numbers (such as enamel) tend to cause a higher degree of beam hardening (Davis et al., 2008). If left uncorrected, the reconstructed image appears less dense at the centre with causing an underestimation of LAC values (Davis and Elliott, 2006). Furthermore, beam hardening causes streak artefacts in strongly attenuating regions (De Man et al., 1999).

4.5 *MuCAT2* Scanner

MuCAT2 is the 4th generation tomography scanner developed by Davis and Elliot, at the Dental Physical Science Department, Queen Mary University of London. This was developed from the 1st generation XMT scanner (Elliott and Dover, 1982)The in house built scanner, which has been optimised specifically for dental research (Davis et al., 2013, Davis and Elliott, 2003), follows the principles of the third generation microtomography system, with the addition of Time Delay Integration (TDI) CCD (Charge-coupled device) readout (Davis and Elliott, 1997).

Time Delay Integration (TDI) CCD readout method is employed in the *MuCAT2* system in order to eliminate the occurrence of ring artefacts. Read out and integration occurs simultaneously; this averages out the characteristics of all the detector elements in each row. The relative motion of charge along the CCD surface matches that of the focussed image. Each recorded image pixel is thus derived from the accumulation of charge as it shifted along the corresponding CCD column. Thus the sensitivities of all the recorded pixels in the same CCD column are identical each being an average of every physical detector element within that column (note, since the CCD is orientated at 90˚ to the normal convention, "columns" are horizontal.

The use of TDI also increases the field of view, meaning the sample can be longer than the CCD detector. This makes scanning larger specimens at higher geometric magnifications possible.

MuCAT systems gives high quality images, high signal to noise ratios, being designed for long X-ray exposures and a high dynamic range. This factor does compromise time and thus it is most suitable for studies where accurate quantification of the LAC is required rather than simple geometric measurements, which do not require high signal to noise ratio.

4.6 Beam hardening correction

A reduction in inaccuracies arising from beam hardening can be achieved by narrowing the X-ray spectrum through filtering during the scan and correction during reconstruction by calibration (Zou et al., 2011). Metal foils placed between the X-ray source and the sample absorb lower energy photons (<20keV), to allow transmission of higher energy photons (Jennings, 1988). The *MuCAT2* system uses a combination of Al and Cu filters to pre-harden the beam.

The effects of beam hardening due to polychromatic radiation can further be corrected for by precise calibration method. The attenuation properties of the calibration material are usually similar to that of the material under investigation across the X-ray spectrum of the source. Originally, aluminium was considered a suitable calibration material for the *MuCAT2* scanner as its behaviour in the absorption of X-rays is similar to that of hard

tissues at the X-ray energies of interest (Dowker et al., 1997, Wong et al., 2000). Its attenuation coefficient versus energy relationship is similar to that of hydroxyapatite in the low energy range and neither exhibited an absorption edge within the energy range of the *MuCAT2* XMT system. Furthermore, Aluminium was selected for its ease of machining to precise thicknesses and for the ability to obtain it at high purity (Evershed 2013).

The initial method of calibration for the 4th generation XMT scanner was to measure the attenuation of a symmetrical seven step aluminium wedge (99.98% Al sheet, 1.2mm thick) (Fig. 4.3a) (Wassif, 2007), placed horizontally on to the rotation stage (parallel to the plane of the beam), at each combination of voltage and filter thickness used (Davis and Elliott, 2003). However, the variation in thickness across the structure (thickest in the middle) caused scattering artefacts and thus was replaced with a 10 step Al wedge (0.5mm thick), mounted vertically on the stage (Fig. 4.3b) (Davis et al., 2008, Ahmed, 2010). A single projection was taken for each step of the wedge by raising the specimen stage between projections, each projection provides an attenuation measurement for a different thickness of aluminium, with the other steps shielded from the beam to minimise X-ray scatter. Wedge-shaped phantoms has the advantage that only one projection image is required to obtain more data points on the beam hardening curve than with the use of plates (de Casteele et al., 2004).

The most recent development in calibration of the *MuCAT2* system is the multi element carousel (Fig. 4.3c) comprising of 9 high purity attenuation plates. The structure is made up of 5 aluminium plates (0.2 to 4mm thick), 3 titanium plates (1 to 4mm thick) and a copper plate (2 mm thick) supported by two circular aluminium plates. The carousel is fixed below the sample stage and is scanned at the end. The filter elements are arranged around the carousel such that it permits the individual illumination of a filter by allowing the beam through the gap between the two sheets nearest the opposite side of the carousel. This arrangement provides a greater range of attenuations than a single species piece without the geometrical limitations, since the copper and titanium filters have significantly higher LACs at relevant energies than aluminium (Evershed 2013).

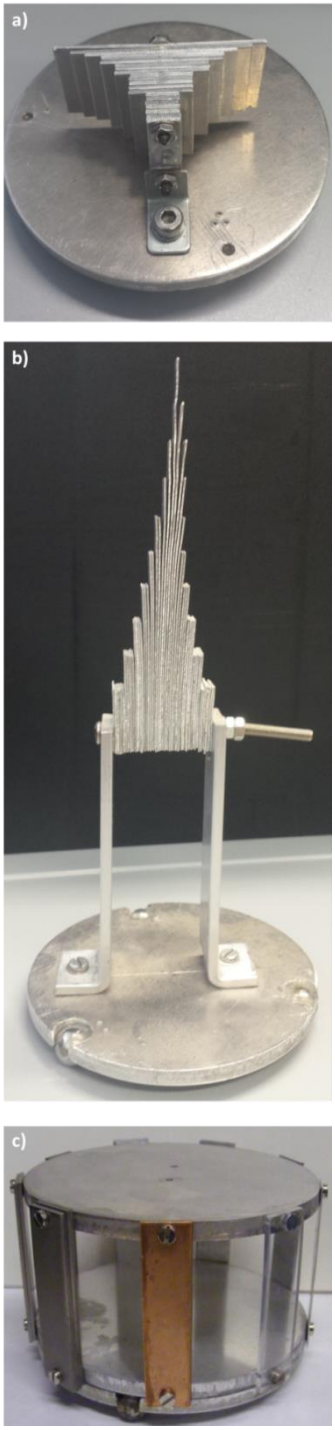

Figure 4.3: Evolution of the XMT calibration piece to reduce beam hardening a) horizontal seven step Al wedge, b) vertical ten step Al wedge and c) multi-element carousel.

4.7 Data collection

Tomographic data is collected by placing a specimen in the path of an X-ray and measuring the attenuated intensity (transmitted beam) with a 2D detector. The specimen, size and density determine the scan parameters such as, number of projections, exposure time (affects signal to noise ratio), image resolution, the X-ray tube voltage and current.

The minimum number of projections (P) required for reconstruction of the specimen can be calculated using equation 4.2.

$$P = \frac{\pi}{2} x$$

Equation 4.2

Where, x is the width of the specimen, in pixels. Larger samples therefore require a greater the number of projections.

A projection is taken at every angle across 360°, the centre of rotation can be determined using the mean of the centres of mass for each projection (Davis, 1994,Evershed, 2013).

4.8 Data reconstruction

Tomographic reconstruction is the process by which a set of 2-dimensional projections taken of the specimen through 360° are built up to provide a 3-dimensional array of X-ray LAC. A modified Feldkamp cone beam back projection algorithm (Feldkamp et al., 1984) is applied to the corrected projections in order to reconstruct the set of projections. The centre of rotation is calculated by locating the centre of mass from each projection (Ahmed, 2011).

4.9 Mineral concentration

The distribution of LAC values can be used to quantify the concentration, C, in a specimen by applying the following equation:

$$C = \frac{\mu_{LAC}}{\mu_m}\ \rho$$

Equation 4.3

Where μ_{LAC} is the measured LAC of the specimen

μ_m is LAC of a pure sample of the mineral

ρ is the sample density

4.10 Scanning electron Microscopy

Scanning Electron Microscopy (SEM) is an extensively used method to view structural and morphological features at the surface of samples at a high resolution. It is widely used across all research fields to study different materials, providing valuable information on the microstructural organisation and chemical and elemental composition, developing an understanding of the specimen at a sub-micron level. It utilises an electron beam to produce magnified images of specimens.

Information is provided by using a beam of electrons produced at the top of the microscope by an electron gun (hot filament) to scan the sample of interest. The beam follows a vertical path through the microscope to the specimen, which is held within a vacuum. Electrons travel through electromagnetic fields and lenses, which focus the beam into a fine probe which is scanned across a chosen region of the specimen surface in a raster by scan coils. Once the beam hits the sample, secondary, backscattered and Auger electrons are produced. Specimens must be electrically conductive for any interaction to occur; this can be achieved by coating the surface of the specimen with an electrically conductive thin film (either gold or carbon in the order of 20 nm thickness). These electrons are detected to form the image.

Secondary electrons

Secondary electrons primarily show morphology and topography on samples with the presence of some compositional contrast. Secondary electrons escape from the specimen at

low energies; these are knocked out of their orbits by an incident electron. This results in high spatial resolution images (Vernon-Parry, 2000).

Backscattered electrons

Backscattered electrons are most valuable for illustrating contrasts (elements of higher atomic mass have a greater contrast) in composition in multiphase samples and crystallographic information. These are the incident electrons that approach the nucleus of the atom sufficiently closely to be scattered through a large angle and re-emerge from the surface. These have higher energies than the secondary electrons, as the scattered electron come from deeper in the specimen, there is a slight compromise in resolution (Vernon-Parry, 2000).

4.11 Scanning microradiography

Microradiography is an established technique for studying the microscopic distribution of X-ray absorption in a thin section. Scanning microradiography can be applied to enamel samples to determine the rate of mineral loss and map changes in mineral density of teeth affected by caries (Anderson and Elliott, 1992). A narrow beam of X-rays is transmitted through the sample and measured with a photon-counting detector. The advantages of using a photon counting detector over a conventional photographic emulsion is avoiding the non-linearity of emulsions and in particular, allows a much larger dynamic range without the problems of background noise and saturation inherent to photographic emulsions (Elliott et al., 1994). Furthermore, samples can be placed at a distance from the detector, allowing it to be placed in a Perspex cell in order to control its environment. Measurements can be made at a single point, a series of points along a line or over a 2-dimensional array of points. A number of cells can be mounted on the scanning stage, allowing multiple experiments to be undertaken.

Scanning microradiography (SMR) enables monitoring of local mineral loss of thin sections of enamel during demineralisation without disrupting the specimen. Photon counting X-ray detectors are used with good counting statistics, so small changes in mineral content can be detected over a wide range of specimen thicknesses. The number of incident

and transmitted photons from the characteristic radiation of the target selected by the counting system are recorded in fixed times. From these the mineral mass can be calculated, knowing the appropriate mass attenuation coefficient. In addition, the statistical accuracy of any measurement can be calculated directly from the number of photons counted (Anderson et al., 1998).

Chapter 5: Introduction to the Study of Enamel Structure Using X-Ray Techniques

5.1 Introduction

The effect that structure has on the function of enamel as a cutting, grinding, masticatory tool (via its mechanical properties) is known to be an important feature of enamel. However, the precise relationship between structure and function in health and disease is still not fully understood. Investigation of enamel structure and properties in relation to its function has been conducted for several decades by a variety of advanced research techniques to extract information at different length scales in this hard tissue. Understanding the process of biomineralisation and the resulting complex microstructure is of great interest to clinicians, dental research and material scientists.

Early observations of microstructural features in dental enamel were made using polarised light microscopy, taking advantage of the materials birefringent nature. The technique was commonly used to identify and differentiate between the different zones during the formation of a caries lesion, based on the light scattering properties. SEM further developed understanding at a higher length scale and has been widely used to view the enamel surface, it shows topography. High resolution TEM is a technique that allows imaging of individual crystallite. AFM, TEM and SEM are qualitative techniques probing the surface only. X-ray absorption and scattering techniques can probe the atomic, sub-nanometre, nano- and micro- length scales revealing spatially resolved information on the chemistry, density, crystallography and nano- and micro- structures in this highly hierarchical material. Synchrotron and laboratory X-ray diffraction and absorption techniques are used to study healthy enamel structure (Al-Jawad et al., 2007, Simmons et al., 2011, Sui et al., 2013, Sui et al., 2014, Tafforeau et al., 2012, Dowker et al., 2004, Hirota, 1986). These techniques are also used to study enamel in disease including caries (Yagi et al., 2009, Tanaka et al., 2010, Huang et al., 2007, Deyhle et al., 2014); fluorosis (Colaço et al., 2012, Blau et al., 2002); and inherited conditions (Al-Jawad et al., 2012). They can also be used to study changes in

enamel structure following controlled de- or re-mineralisation (Lautensack et al., 2013, Tanaka et al., 2010); or controlled heating (Sui et al., 2014).

The work presented in this thesis builds on what is already understood about enamel structure. Therefore, in this chapter, recent studies utilising advanced X-ray techniques to measure enamel structure at the atomic, sub-nanometre, nano- and micro- length-scales are described.

5.2 Enamel at the Atomic and sub-nanometre length-scale

Enamel lattice parameters

X-ray diffraction is a commonly used method for studying the properties of enamel, as it is a crystalline material and scatters the X-ray beam in characteristic directions, which can determine the composition and structure. Powder diffraction is a useful method for providing structural information and determining the phases present. However, it does not measure the degree of preferred orientation of crystals in the material. In order to determine the crystallographic properties and chemical structure, XRD on powdered enamel has been used to establish fundamental information at a crystallographic length scale, defining the lattice parameters and space group as a = 9.441 Å and c = 6.878 Å and $P6_3/m$ (Al-Jawad et al., 2007, Young and Mackie, 1980, Wilson et al., 1999, Wilson et al., 2004). However, enamel is an anisotropic material with varying chemical and structural properties as a function of position. Thus in order to really appreciate the crystal organisation of enamel, it is important to consider the spatial resolution. This can be determined using synchrotron radiation.

Changes within the crystal structure have an effect on the properties. Substitution of carbonate for the phosphate ions causes distortion of the apatite structure by the decrease in the a-lattice parameter; this in turn increases crystal solubility, making it prone to dissolution (Elliott, 1997). A systematic decrease in the a-lattice parameter occurs due to increase in carbonate substitution as a function of increasing tooth age, resulting in the reduced crystallinity and average crystallite size (from 38 nm to 12 nm) of human dental apatite demonstrated by broadening of the (002) and (310) Bragg peaks (Leventouri et al.,

2009). The c-lattice parameter remains constant revealing no significant substitution occurs at the hydroxyl site as a function of tooth age.

Diffraction of powdered enamel provides information over an average sample mass but does not account for any spatial variations. As mentioned in chapter 2, enamel is an anisotropic and graded structure, varying in chemical composition and crystallite organisation at different sites of the tooth crown. In order to fully appreciate and understand the structure of dental enamel, the method of powder diffraction has recently been applied to intact tooth sections (measured in transmission geometry) as a non-destructive modern approach to study complex enamel features.

The *a*- and *c*-lattice parameters can vary between -0.6 % and +0.3 % within a section of a tooth as a function of position in both the transverse (Al-Jawad et al., 2007) and occlusal plane (Egan et al., 2013). The *a*-lattice is largest at the surface, it decreases with depth of the enamel. The *c*-lattice parameter on the other hand displays the inverse trend, whereby it is smaller at the surface (Al-Jawad et al., 2007). Lattice parameters in developing enamel are larger and display homogenous distribution in comparison to fully mature enamel (Simmons et al., 2013).

Fluoride has anti caries properties, however, an increase in Fluoride levels above the optimal levels can lead to Dental Fluorosis. High resolution X-ray powder diffraction on the Australian beamline was used to collect diffraction patterns from powdered enamel sample affected by Fluorosis. Dental Fluorosis is a developmental disturbance of enamel as a result of excess ingestion or inhalation of Fluoride, which can also affect bones. Enamel appears stained and discoloured, with surface irregularities. Incorporation of excess Fluoride ions into the crystal lattice causes a decrease in the lattice parameters. Greater understanding into the crystallographic parameters from this study can be used as a model to distinguish the difference between Fluorosis and AI and improve clinical diagnosis as well as aid prevention and treatment regimes.

Synchrotron radiation facilities only require a small amount of the powdered sample in comparison to conventional laboratory sources (one tenth in this case, 10 mg) to obtain

sufficient data for analysis. This makes it ideal for studying samples with small amounts of enamel, hypoplastic enamel. The intense flux and the large range (with image plates) available at the synchrotron make high resolution data collection far more rapid than conventional X-rays (Blau et al., 2002).

5.3 Enamel at the Nanoscale and Micron length scales

Preferred orientation in healthy and disrupted enamel

Crystallographic and microstructural information of enamel can contribute towards understanding the fundamental processes of biomineralisation and overall tooth development. Its nanometre length scale is a beneficial way in understanding the effects of caries on enamel structure. Studies carried out on pathological tissues are a good way to gain an insight into formation of healthy tissue as well as understanding the structural manifestations of genetic defects.

Thewlis (1940) was the first to examine the crystal orientation using X-ray diffraction in an intact enamel section. The *c*-axis of the HA crystallites are arranged are parallel to the direction which the (002) arcs lie in the 2D diffraction pattern.

Heterogeneity in enamel texture and mechanical properties have been observed by probing a single linear depth track from the enamel surface to the EDJ of an intact tooth section using a combination of Grazing Incidence Synchrotron Diffraction (GISXRD) and Vickers indentation (Low 2004). Preferred orientation displayed by HA can be revealed by the variation of intensity ratios for the three maximum Bragg reflections, (211), (300) and (002). Low (2004) used the R parameter, or texture index, to quantify the degree of texture in enamel. The R values for (300) and (112) can be calculated using the following equations:

$$R_{300} = \left[\frac{I_{(211)}}{I_{(300)}}\right]/1.63$$

Equation 5.1

$$R_{112} = \left[\frac{I_{(211)}}{I_{(112)}}\right]/1.94$$

Equation 5.2

Texture is present when R is greater or less than 1.0, however crystals are randomly orientated when R = 1.0. This principle is similar to Equation 3.8. Differences occur in the texture index of the two Bragg reflections. The (300) reflection sees very little variation in texture with increasing enamel depth, whereas the texture index in the (211) reflection is more depth dependant, highlighting a gradual reduction in texture corresponding to loss of crystallinity and microhardness from surface to EDJ (Low, 2004).

The spatial distribution of preferred orientation can be mapped in dental enamel using synchrotron X-ray diffraction (Al-Jawad et al., 2007, Al-Jawad et al., 2008, Low et al., 2008, Raue and Klein, 2010, Raue and Klein, 2011, Simmons et al., 2011, Al-Jawad et al., 2012, Simmons et al., 2013). This can be used to determine the magnitude and direction of enamel crystals based on the intensity and location of the Debye ring respectively. Furthermore, the degree of tilt (out of plane, perpendicular to the tooth section) can be calculated using the method described in Simmons *et al* (2011). Al-Jawad *et al* (2007) mapped the spatial variation (150 µm resolution) in crystal preferred orientation within a whole section of a human permanent premolar. Preferred orientation within the tooth sample was determined by Rietveld refinement analysis. The highest degree of crystal alignment was seen in the buccal cusp and inner side of the lingual cusp of the section, whereas the cervical edges of the crown displayed less order. Areas of highly arranged apatite crystals correspond to the occlusal biting surfaces whereby by it encounters the greatest mechanical load. The highly anisotropic and heterogeneous distribution of HA crystals occurs not only within a tooth section but throughout the whole tooth, as was demonstrated by Simmons *et al* (2011).The direction and magnitude of enamel crystallites in 6 sequential sections (500 µm thick) of a maxillary first premolar were measured and analysed using a similar experimental set up and data analysis method to Al-Jawad *et al* (2007) but at a lower spatial resolution, 300 µm. The sections, parallel to the mesial-distal

plane of the tooth displayed variations in texture direction and magnitude as a function of position across the tooth crown. Preferred orientation in the (002) direction varies with respect to both the distance from the buccal and palatal end slices and the position on an individual tooth section. Crystals are aligned perpendicular to the EDJ in the cervical region of the buccal, palatal and central slices, whereas in the cuspal region the crystallites oriented parallel to the EDJ. The buccal and palatal slices exhibit a higher degree of tilt (out-of plane) and less texture in comparison to the central slices. Texture is present in both enamel and bone (Wenk & Heidalback 1999).

Xue *et al* (2008) used laboratory microdiffraction instrument to collect 2D images at different points from a healthy and carious affected deciduous molar, in order to demonstrate spatial resolution can be achieved with a laboratory beam source. There was an increase in crystal size, calculated using reflection (211), from EDJ to enamel surface. Preferred orientation, comparing the ratio of intensities of the (300) and (002) Bragg reflections, was evident in bulk enamel. Six points were measured across the whole sample, both enamel and dentine, with 500 µm between each point. This study is an example of the advancement of laboratory sources, as it uses a non-destructive method to collect diffraction data. Although the main advantage to using a laboratory source is the accessibility to the equipment, as qualifying for beam time is often very competitive, the speed of data collection is slow, allowing only small amounts of data to be collected. The quality and quantity is also compromised as there is a loss of spatial resolution.

Data collected from the technique of X-ray diffraction can be used to observe three dimensional crystallite orientations in enamel to help detect the caries sensitivity and deviations in mechanical properties. Sakae *et al* (2011) used a laboratory source to analyse the crystallite orientation at the surface and subsurface of molar teeth. By using the same method to get 2D patterns but rotating and tilting the sample the three dimensional orientation can be obtained. This study looks at the relationship between enamel prisms and crystallites; this was achieved by selecting regions whereby the enamel prisms run parallel to each other.

The study of the arrangement of prisms and crystallites in the prisms is of utmost clinical significance as it can affect the mechanical properties and caries susceptibility. This can furthermore give an indication of the process of biomineralisation at a molecular level, the role of the different proteins. Crystal orientation maps were calculated using (002) and (213) planes. Crystallites at the surface of the tooth are orientated parallel to one another and tend to deviate at the subsurface region (Sakae et al., 2011). The number of molar teeth was not specified, which affects the reliability of the results. This study observed the changes in the divergence of prism at only two points. Data collection for these two points took 6 hours, by using a high intensity beam 2D patterns can be collected from an entire section of a tooth at a resolution of 150 μm in 8 hours (Al-Jawad et al., 2007) such that other studies (Al-Jawad et al., 2007, Al-Jawad et al., 2008, Simmons et al., 2011) have been able to map an entire section and a whole tooth respectively. The common theme in two studies described above seems to be insufficient data collection as a result of time. This is a drawback of laboratory X-ray sources as the intensity of a synchrotron source cannot be achieved in a lab. The data collected are accurate and reliable, however in order to observe small changes across the enamel surface it is critical to study more points at a higher resolution (micro or nano-focused) and using a small beam spot size, all which can only be achieved in a realistic data collection timescale at synchrotron facilities. Position sensitive synchrotron X-ray diffraction and high contrast X-ray microtomography have been used to study the crystallographic parameters and mineral concentration respectively in enamel at different developmental stages (Simmons et al., 2013). Investigating and understanding the spatial and temporal progression of human enamel biomineralisation at a crystallographic level can aid development of biomimetic materials. Three archaeological tooth specimens across different time points of the maturation stage (early, mid and complete maturation) were measured at a 150 μm resolution. Data displayed an inverse correlation between mineral content and spatial organisation. Mineral content increases and becomes more homogenous as the enamel matures whereas the organisation becomes more complex and heterogeneous.

Synchrotron X-ray microdiffraction has also been used to evaluate the influence of a rare group of metabolic disease, mucoploysaccharidosis (MPS) on the texture pattern in

deciduous human enamel. MPS results from the absence or malfunctioning of lysosomal enzymes needed to break down glycosaminoglycans molecules, which aid bone development (Al-Jawad et al, 2012). Type IVA has manifestations in both primary and secondary dentition. Basic dental histological investigations have demonstrated that MPS IVA is abnormally thin and pitted with increased porosity correlating to the Straie of Retzius. Texture analysis of the SXRD data revealed that there are differences in mineral crystallite orientation in MPS affected enamel as compared to control specimens. The gradation of crystallite organisation seen in healthy enamel as a function of distance from the enamel surface, is absent in MPS affected enamel giving clues as to the point in amelogenesis where the most disruption occurs.

Other texture studies carried out enamel are in agreement with the above findings, using the (001) pole figures. Raue *et al* (2012) found texture reached its maximum at the cuspal region, both buccal and palatal cusp of a molar sample. The lowest texture value was found to be by the fissure of the tooth. The cervical edges and the inner cuspal regions display low texture. The orientation changes continuous from flat inclination to vertical direction following the morphology of the tooth. Again, the same trend is seen in the incisor tooth, whereby the highest degree is seen at the tip of the surface, the occlusal region and the bulk centre of the enamel. The highest degree of HA preferred orientation occurs in the region subjected to the greatest mechanical load, the cusps of the molar tooth and the cutting edge of the incisor. Crystallites are oriented so that their *c*-axis points to the surface to the tooth.

The studies discussed have shown Synchrotron X-ray diffraction to be extremely useful when applied to enamel, intact tooth sections can be mapped to give an array of information, such as lattice parameters and preferred orientation, while keeping spatial distribution in mind. The application in this case has been on healthy enamel. This project aims to build on these studies by using the strengths of the SXRD technique and applying it to enamel affected by AI. Furthermore, crystallographic information obtained from healthy enamel can be compared with to AI affected enamel.

Carious enamel

In the last decade, enamel affected by caries, or artificially induced caries-like demineralisation and subsequent synthetic remineralisation processes have been investigated using synchrotron x-ray diffraction (Seredin et al., 2013, Gaiser et al., 2012, Deyhle et al., 2011, Yagi et al., 2009, Tanaka et al., 2010). Two recent studies carried out by Yagi *et al* (2009) and Tanaka *et al* (2010) took advantage of synchrotron radiation to study the effect of demineralisation and remineralisation respectively, at a submicron and atomic level. Experiments were conducted on the BL40XU beamline at SPring8, Japan, to measure the changes in the amount of hydroxyapatite crystallites in subsurface lesions (Yagi et al., 2009, Tanaka et al., 2010). This study is an example of how different types of X-ray scattering methods can be used in conjunction with each other to provide complementary information. Transversal microradiography (TMR) was the primary standard technique used to measure mineral content (as absorption correlates to mineral density), however a major limitation of this technique is that it does not provide any information on crystal structure; therefore wide angle X-ray diffraction (WAXS) and small angle X-ray scattering (SAXS) were used to elucidate this information. WAXS specifically quantifies the amount of hydroxyapatite crystallites and SAXS characterises the presence of voids caused by the loss of the HA crystallites.

Artificial lesions (demineralised and/or remineralised) and sound zones were created on the same bovine enamel samples to reduce the likelihood of natural variability between teeth. Following treatment, samples were sectioned to 150 µm and exposed to X-ray beams, a small beam spot size of 6 µm was used, and such precision is unique to synchrotron diffraction.

The results from each of the three separate methods were in agreement with one another, indicating the reliability and validity of such methods. In addition a good sample size was used, though this was not clearly specified, and results were averaged out, which again is evidence for its accuracy. All show a decrease in enamel density at the direct site (around 35-40 µm) of the subsurface lesion and an increase in voids at the same site.

The initial objective of this study, to quantify changes of hydroxyapatite crystallites at the site of a subsurface lesion using TMR, WAXS and SAXS, was successfully achieved.

Explanation as to why bovine enamel was used instead of human enamel was not provided; a possible reason may be the size of the tooth facilitated the different treatments on the same piece of enamel. Experiments such as this on human enamel could be of great clinical significance. The depth of information given means that the experimental set up could easily be reproduced to study other aspects of the enamel such as changes in texture and crystal size.

The data collected by Yagi *et al* (2009) and Tanaka *et al* (2010) are excellent examples of the depth of information present within the SXRD dataset. Alongside the information they presented, they could possibly have extracted even further information from their experiments on the effect of demineralisation on enamel microstructure. For example, analysis of the (002) reflection alone would hold enough potential to study changes in crystallite orientation (texture) in the subsurface lesion, whilst Rietveld refinement of the diffraction patterns could give information on changes in crystal size, texture and lattice parameters simultaneously.

After successful characterisation of caries affected dentine, Deyhle *et al* (2014) applied the method of scanning SAXS to characterise caries affected enamel, allowing for the identification of distinct zones with varied absorption and scattering behaviour indicative of varied porosity and pore morphology. The orientation and anisotropy of the SAXS signal was unaltered throughout both lesions with crystallite orientation preserved throughout the lesions. This facilitates the identification of preventative remineralising strategies with the potential to reform the original nanostructure.

Retention of organisation has important implications for the potential for interventions to not only remineralise demineralised enamel as well as in the original organisational form at the nanostructural level.

5.4 Diffraction Tomography to study dental enamel

Recent advancement in the study of tooth structure applies high energy X-ray diffraction computed tomography to observe the internal crystalline structure of enamel. The use of high energy X-rays allows the collection of diffraction images as well as absorption

tomography from an intact tooth sample, without the need of any sample preparation. A recent study conducted on the ID15 beamline at the ESRF showed the potential of this technique in dental research (Egan et al., 2013) as high energy beamlines (ID15 operates at 90 keV) provide energy to penetrate through the full thickness of a whole tooth. It has clearly shown that dental caries appears as an amorphisation of the HA crystal. The non-destructive nature of this technique means rare and fragile samples can be observed in greater depth.

5.5 XMT Studies using Synchrotron and Laboratory Sources

The monochromatic beam at synchrotron facilities provides absolute and accurate Linear Attenuation Coefficient (LAC) measurements at high resolutions without the need for calibration (Wong et al., 1996). Additionally the monochromaticity of the X-ray makes it ideal for attenuation and quantification studies of calcified tissues. They are particularly suitable for 3D microtomography (Elliott et al., 1998). Synchrotron microtomography is an extremely powerful method for studying mineral loss in bones and teeth and observing microscopic defects, however access is restricted and limited time is available due to the high demand.

Microtomography studies carried out on mineralised tissue using synchrotron radiation, have been used in a variety of ways including investigating carious lesions (Dowker et al., 2004); imaging dental fissures (Dowker et al., 2006); determining the microstructure of hominoid enamel (Tafforeau, 2007); quantifying mineral density of teeth and bones (Ito et al., 2003); and measuring the stresses within materials (Almer and Stock, 2005). The precise measurements of attenuation coefficients and greater sensitivity to changes in mineral as a function of time and position (Delbem et al., 2009) make it an accurate technique. The benefits of this technique allow accurate measurements of enamel and bone from healthy to severe, allowing a greater understanding of the development of lesions. As previously mentioned, monochromatic radiation provides accurate LAC values which are used to derive mineral concentration. Despite the efficiency in processing and analysing results as it does not require any correction for beam hardening or artefacts, when viewed broadly, submitting proposals and travelling to such facilities can be time consuming. The

characteristics of synchrotron radiation allow rapid data collection and provision images at high contrast and spatial resolution (micro-meter level). Furthermore, its non-destructive nature not only simplifies sample preparation, but also allows further analysis using different techniques to be applied to it. The penetration depth allows structures that maybe invisible to standard microtomographic techniques (Tafforeau et al., 2006).

The work discussed focuses on tomography of samples carried out using synchrotron radiation. All have shown that this is an accurate technique which rapidly provides a large amount of data. The studies have highlighted that tomography is not just restricted to quantifying mineral concentration, but is diverse in its ability, making this an extremely powerful method of study. However, this is an expensive facility and obtaining beam time is highly competitive, often restricting the number of studies that can be carried out. Additionally, the studies mentioned above have all used one of the top three third generation synchrotron facilities.

X-ray Microtomography can be used with a lab source to study, caries, enamel/dentine defects and mineral concentration. This is more widely used due to its ease in accessibility. With continual enhancement of the lab scanners such as correction in beam hardening, and artefacts and precise calibration, accurate data can be obtained. Over the years, laboratory XMT has proven to be successful in quantifying the mineral concentration and observing internal defects.

An example of laboratory XMT used in dental research is the study carried out by (Fearne et al., 2004) where X-ray microtomography was applied to quantify the mineral concentration of molars with idiopathic enamel hypomineralisation. This is an example of the different ways X-ray microtomography can be applied in dental studies. The main clinical significance of this the fact that hypomineralisation can often be under diagnosed or misdiagnosed, as the enamel appears to be of normal thickness yet poorly mineralised. This type of analysis can reveal a great deal about the process of enamel formation. Location of deficiencies in enamel can identify the stage where the defect occurs.

Using XMT Fearne *et al* (2004) were able to show a mineral density map and able to show where the defects were and correlate it to an enamel formation malfunction. It has clearly demonstrated the enamel thickness is the same as healthy enamel but has a lower mineral concentration.

The contour map of the mineral distribution of a 15 µm axial section presented in this paper highlighted lower mineral concentration in all but mesial region. The extent of severity varies throughout the enamel, from only isolated areas to the low mineral concentration throughout the entire thickness. Line profiles taken from a severely affected region and a relatively healthy area (mesial) from the same tooth, showed a 20 % reduction in mineral concentration from the hypomineralised region. Line profiles taken from healthy tooth showed increasing mineral concentration from ADJ to the surface. The characteristics suggest that disturbances may occur after the initial stage of enamel formation. this is an example at the extent to which this method can be applied (Fearne et al., 2004).

Laboratory XMT has a number of advantages, the main one being its accessibility, which allows different types of research to be carried out at ease. The visual display of information is a fundamental aspect in dentistry; the ever evolving graphics make analysis more precise and accurate as it produces cross sectional slices of uniform thickness. Additionally the rendered surface images along with the ability to rotate and transverse through an object ensure detailed analysis can be carried out.

Tomography is generally preferred when examining tooth sections, as physically sectioning can be time consuming; and results in loss of material between each slice which destroys the integrity of the sample. A study conducted by Dowker *et al* (1997) highlights the strengths of XMT and the resulting images and show it can be used as an educational tool. The high resolution of the XMT system can display Information on dental morphology, cariology, cavity preparation and restoration. Data obtained from scans can be used to provide quantitative mineral densities (Davis and Wong, 1996), illustrate the effects of errors in endodontic techniques (Dowker et al., 1997) and identify complex structures, such as developing root canals. By observing tooth samples from different planes and orientations, the extent of carious lesions can be determined (Cochrane et al., 2012).

Reconstructed images resulting from the data collected give far more accurate slice images that manually section enamel as each slice thickness is uniform and tissue will not be lost during sectioning.

Commercial XMT scanners are widely available for laboratory use, these include Skyscan and Scanco. They are simple to use and provide a similar data to that of the MuCAT systems, however due to the absence of the TDI mode, commercial scanners are not immune to ring artefacts and calibration is less accurate.

Chapter 6: Materials and Methods

In this chapter, the experimental methods (facilities and instrumentation) are described together with a detailed description of the data processing systems, for which the theoretical principles have been explained in Chapters 3 and 4. The precise experimental set-up parameters varied for each study according to the objective, specimen type and beamline used, thus these will be stated in the experimental setup section of their respective chapters.

6.1 Synchrotron beamlines used

There are currently 70 synchrotron light sources worldwide, each with varying energy levels and number of beamlines. These facilities offer a flux, energy range and resolution unachievable by conventional (laboratory) radiation sources. The three most powerful third generation sources include European Synchrotron Radiation Facility (ESRF, Grenoble), Advanced Photon Source (APS, Illinois) and Super Photon Ring 8 GeV (SPring-8, Japan). Such facilitates operate throughout the whole year with time being split into periods to accommodate users (delivering beam in different filling modes), machine dedicated time and shutdown. The two beamlines used for this thesis were XMaS (BM28) at the ESRF, and 2-ID-D at the APS.

6.1.1 XMaS (BM28) beamline (ESRF)

The ESRF, located in Grenoble, is an international research institute operating the most powerful synchrotron radiation source in Europe, accelerating electrons at an energy of 6 GeV and a current of 200 mA with a storage ring circumference of 844 m and housing 40 tangential beamlines.

BM28, most commonly known as XMaS (X-ray Magnetic Scattering), is the UK- CRG (Collaborative Research Group) beamline, supported by the Engineering and Physical Sciences Research Council (EPSRC) and managed by the Universities of Liverpool and

Warwick. The beamline is situated on a bending magnet and comprises of a unique combination of instrumentation to cater for magnetic and high resolution diffraction, with tuneable x-ray energies ranging from 2.5 to 15 keV (covering a wavelength of 4.96 to 0.82 Å). Alterations in the optics setup (Fig. 6.1) (Brown et al., 2001) allows the beamline to operate in both white beam as well as focussed and unfocussed monochromatic modes with beam spot size ranging from a minimum of 20 x 20 µm to a maximum of 3 x 8 mm.

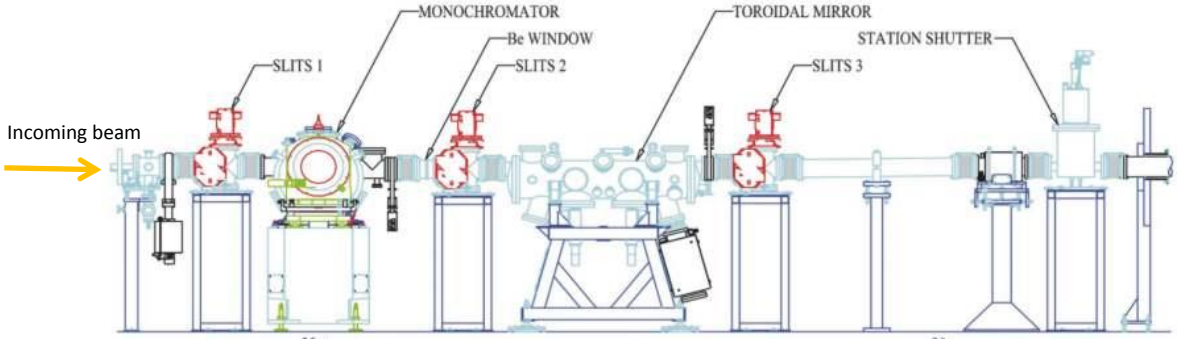

Figure 6.1: Schematic representation of the optics hutch for the XMaS beamline (Image taken from http://www2.warwick.ac.uk/fac/cross_fac/xmas/description/).

Experimental setup

The studies presented in Chapter 8, 9 and 10 were conducted on the XMaS beamline (Fig. 6.2) and made use of a monochromatic beam at 15 keV, achieved by using both the Si (111) double-crystal monochromator mounted in a crystal cage and the toroidal focussing mirrors. The final microfocussed incident beam size was defined by mounting vacuum tube slits close to the sample, which enabled a range of beam-spot sizes from 20 to 150 µm with reduced background scatter.

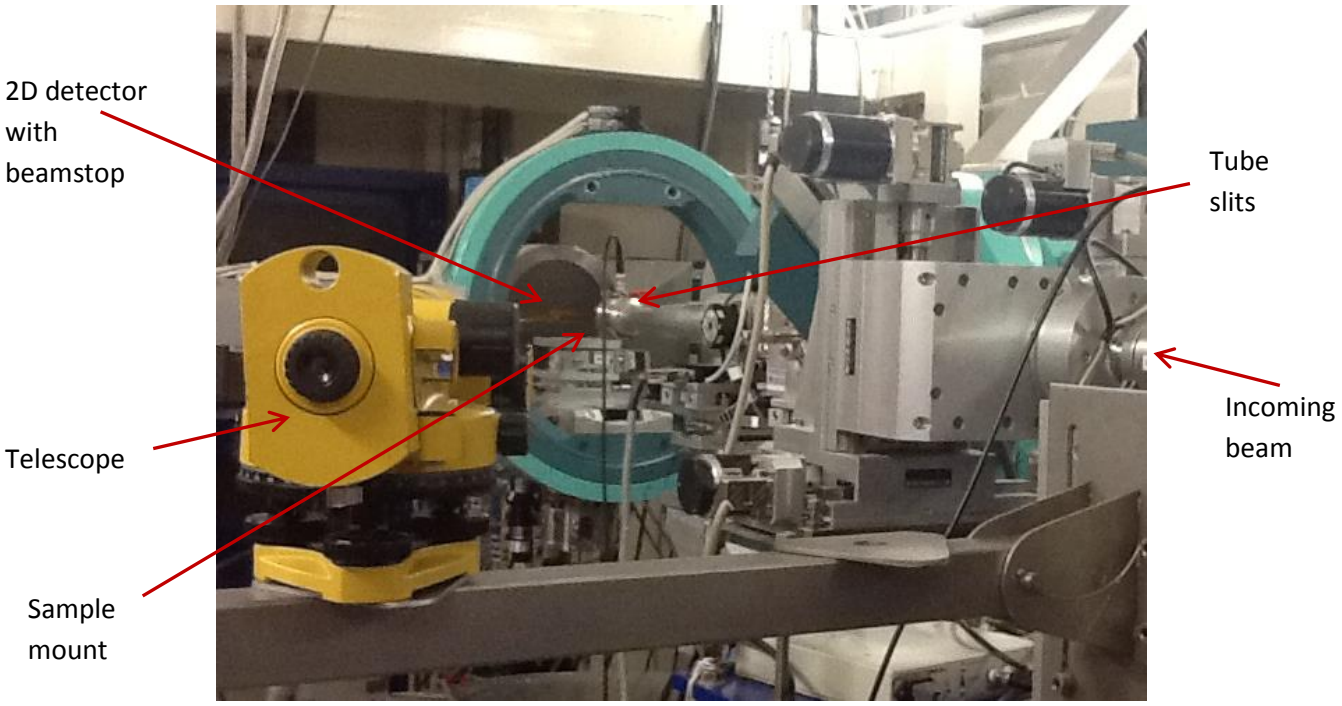

Figure 6.2: Photographic image of the experimental hutch, illustrating the standard setup for transmission geometry diffraction studies on the XMaS beamline for this thesis.

A MAR165 CCD (corresponding to 165 mm detector diameter) camera placed behind the sample (sample to detector distance to be specified in each chapter), used one 4 k x 4 k chip, permanently bonded to a single fiber-optic taper. The camera read the chip from four channels (quadrants) simultaneously, resulting in a 2048 x 2048 pixel image in 2.5 seconds. A lead beam stop was positioned in the centre of the 2D detector with kapton tape to prevent damage by the beam.

6.1.2 2-ID-D Beamline (APS)

The Advanced Photon Source (APS) at Argonne National Laboratory, Illinois, provides the brightest X-ray beams in the Western Hemisphere. The third generation synchrotron radiation facility reaches energy as high as 7 GeV and has 1104 m circumference with 34 beamline stations.

The 2-ID-D beamline (which runs simultaneously with 2-ID-E) at APS is devoted to sub-micron high-resolution X-ray imaging studies, specialising in micro- and nanodiffraction, fluorescence mapping and micro-XANES. The beam is sourced by an undulator insertion device, which provides a high brilliance source for nanofocussing and can reach an energy range of 5 to 32 keV (wavelength range 2.48 to 0.39 Å) with a 0.1 x 0.1 μm^2 focussed beam.

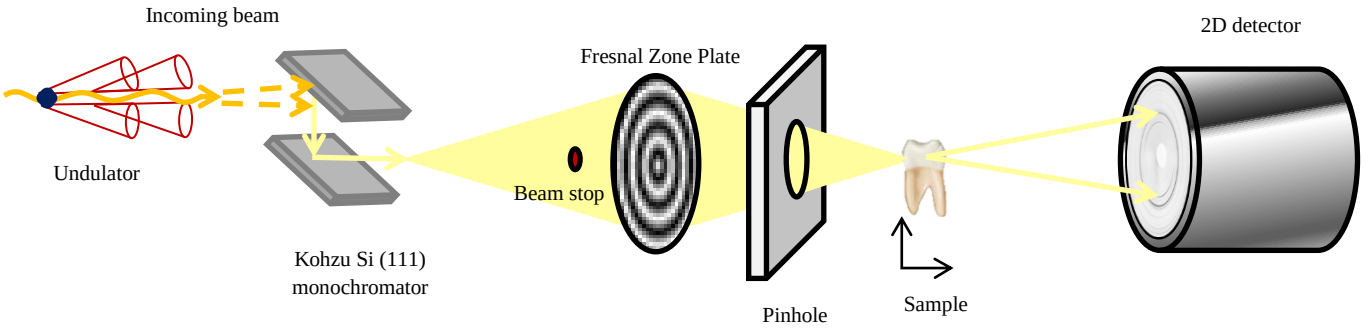

Figure 6.3: Schematic representation of 2-ID-D experimental setup.

Experimental setup

Figure 6.3 shows the experimental setup for micro-diffraction on the 2-ID-D beamline, used to collect data presented in chapter 7. A double crystal monochromator Si (111) and Fresnel zone plate optics were used to attain a focussed fine narrow beam. A pinhole was placed in the path of the beam to reduce the beam spot size. Samples were mounted vertically on an Al plate to be scanned in transmission geometry. A large area CCD 2D detector was placed behind the sample to collect the 2D diffraction pattern.

6.2 Synchrotron data processing and analyses

Visual inspection of 2D diffraction images can immediately determine the presence of preferred orientation. Figure 6.4 shows a typical example of 2D diffraction patterns obtained from enamel (Fig.6.4a) and dentine (Fig. 6.4b). Variations in intensity around the Debye-ring of Bragg reflections are an indication of crystal preferred orientation, a trait

observed in enamel patterns. In contrast a thick broad reflection with continuous intensity, with no azimuthal variations, shows lack of crystal orientation, such most obviously seen in powdered diffraction patterns. The number of Debye rings on the diffraction pattern corresponds to the number of Bragg reflections.

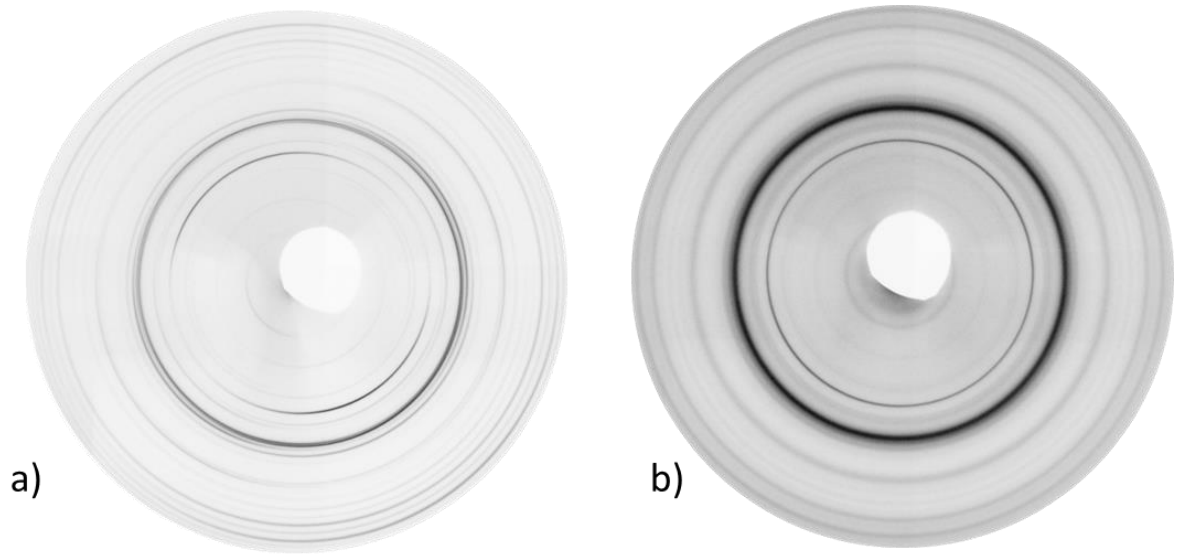

Figure 6.4: 2D diffraction pattern representative of a) enamel and b) dentine.

How the data was processed after collection was determined by the subsequent analysis needed. In order to extract the required crystallographic parameters, two quantitative analyses were performed:

1. Profile fitting (to measure the FWHM) of the azimuthal intensity around the 002 reflection
2. Rietveld refinement of the entire diffraction pattern

6.2.1 FIT2D processing software

All 2D diffraction image files (collected as .edf, .mccd or .tiff files) were processed using FIT2D, an ESRF software package written by AP Hammersley, allowing specialist 1 and 2 dimensional data analysis (Hammersley, 1997). It was initially used to visualise individual

data files and construct composites in order to separate enamel files from those collected in air or dentine patterns.

FIT2D was most importantly utilised for calibration and correction of detector distortions and beam centre. A powder diffraction pattern from standard material with known lattice parameters was used to calibrate for instrument parameters (LaB_6, CeO_2 and Si), such as sample to detector distance and X-ray wavelength. Accurate starting values were provided for finite refinement. Accuracy of the refined parameters was determined by evaluating the 2D polar transform (Fig. 6.5), where vertical lines should be straight (Fig. 6.5a), any deviation from a straight vertical lines (Fig. 6.5b) indicates inaccuracy in the refinement of the beam centre position, the detector tilt angles, or spatial distortion in the detector. This procedure was undertaken carefully for each dataset to ensure optimum calibration of the instrument parameters.

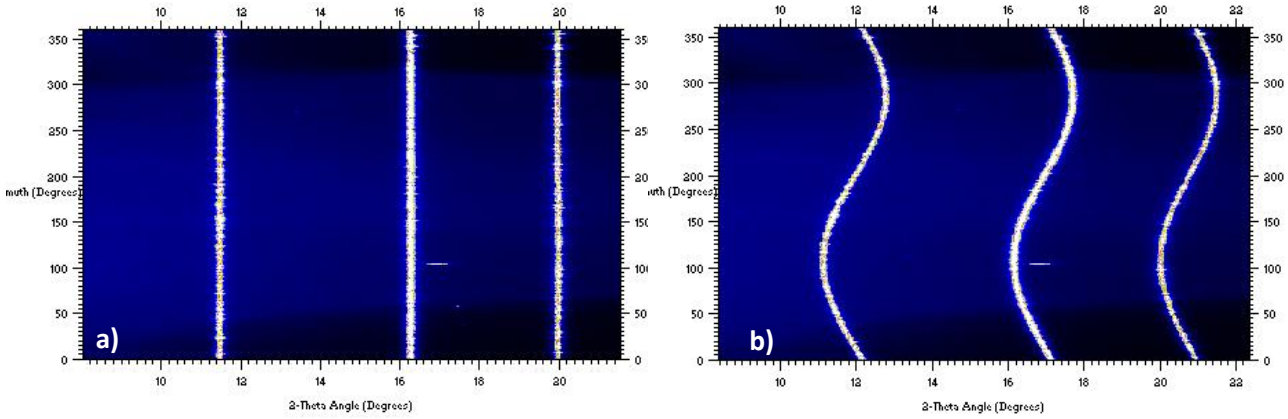

Figure 6.5: 2D polar transforms taken from a LaB_6 calibrant data file showing the difference in the vertical line between a) accurately and b) inaccurately refined instrument parameters.

6.2.2 Full Width Half Maximum (FWHM)

FIT2D was used to perform azimuthal integration (cake) around 360° giving a 1D graph for further analysis.

The distribution of intensity in the (002) Bragg reflection azimuthally around the Debye-ring can be used to quantify both texture direction and magnitude along the *c*-axis of the

enamel crystallites. The (002) reflection was radially isolated and integrated over 360°. The intensity was plotted versus the azimuthal angle and Gaussian peaks (Equation 3.9) were fitted to calculate the FWHM of the two peaks and averaged using Origin (OriginLab, Northampton, MA). By repeating this analysis for each diffraction image across the whole specimen, changes in peak width were used as a method to quantify the preferred orientation as a function of position within the enamel region of interest.

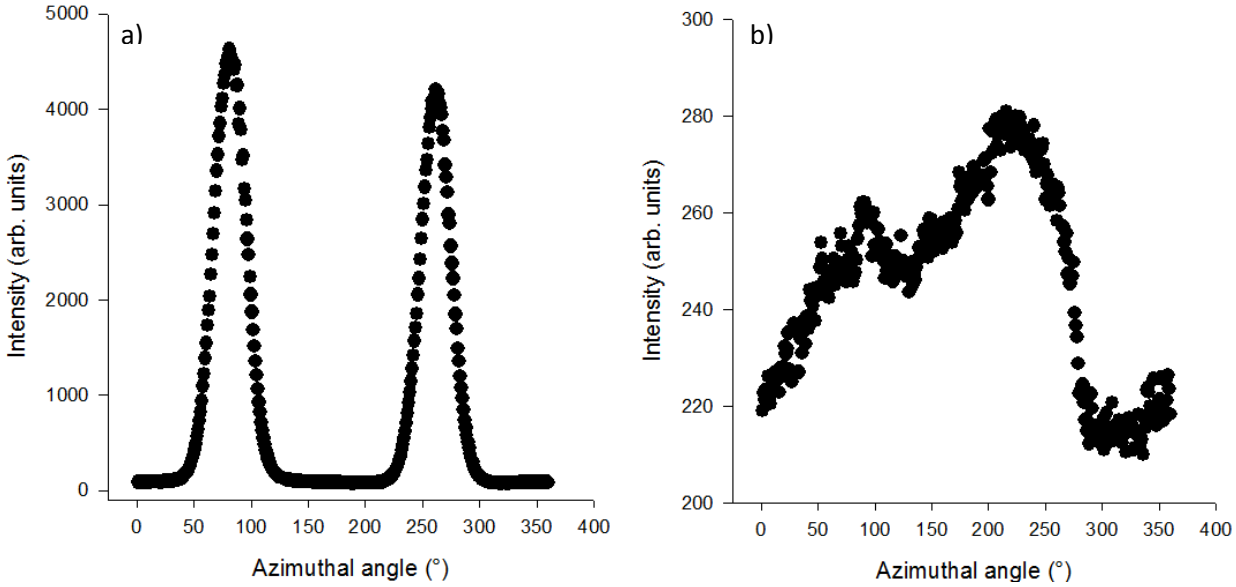

Figure 6.6: Intensity versus azimuthal plots to represent the FWHM of the (002) reflection from a) enamel and b) dentine.

Sharp, well defined and intense peaks (Fig. 6.6a) generate low FWHM values and are typical of highly ordered crystals (high texture), whereas broad peaks (Fig. 6.6b) generating high FWHM values indicate a lack in the degree of crystal order.

6.2.3 Rietveld refinement of enamel diffraction patterns

Fit2D was used to perform radial integration of 2D diffraction images in order to produce 1D diffraction patterns (Intensity versus 2θ) for Rietveld refinement.

The Rietveld method extracts information on crystal structure, such as lattice parameters and size, and texture from diffraction images. This is advantageous over conventional

texture analysis method that relies on individual diffraction peaks, particularly for low symmetry materials with many overlapping peaks and images with poor peak to background ratio (Darling et al., 1968). Using the Rietveld method minimises the effect of variation in sample volume since all reflections are used to obtain a fit. The details of the Rietveld refinement method are described in Section 3.6.4.

For data refinement the following three files are required:

1) Instrument parameter file
2) Model phase file
3) Experimental data file

The instrument parameter file (.prm) contains the characteristic information for the specific experimental setup. The file was created from the standard calibrant material and defines instrument parameters, such as the X-ray wavelength, sample to detector distance and peak shape profile. Once refined, instrument parameters were kept fixed for refinements of data. The experimental data files (in ascii format) are generated by radial integration of the 2D diffraction images through to create one dimensional Intensity vs 2θ diffraction patterns.

Since Rietveld in a structural refinement not structural solution methods, some prior knowledge of the crystallography of the sample measured is necessary in order to select the correct model phase, (in this case HA values taken from (Young and Mackie, 1980). This sets the initial starting values for lattice parameters and crystallite size and the model is refined until a best fit is achieved.

6.2.4 General Structure Analysis System (GSAS)

There are number of Rietveld refinement software packages available. The most commonly used are TOPAS (Coelho 1997), FULLPROF (Rodriguez-Carvajal, J. 1993), and GSAS (General Structure Analysis System) (Larson and Von Dreele., 2000). GSAS was used to carry out the least square refinement for quantitative phase analysis presented in this thesis.

GSAS, created by Allen C. Larson and Robert B. Von Dreele (Larson and Von Dreele 2000), is a comprehensive software package for fitting structural models to single crystal and powder diffraction data collected from X-ray and neutron sources. It is a compilation of

several programs, each designed for specific types of crystallographic calculations. EXPGUI (Toby., 2001) is the Windows-based graphical user interface (GUI) editor for GSAS experiment files. Each algorithm associated with GSAS can be accessed with EXPGUI through the EXPEDT interface, which is the interactive editor for GSAS. EXPEDT sets up an experimental file (.EXP) and controls all other programs within GSAS from a series of menus which provides a choice of refinement options and calculations to be performed. The diffraction data were be prepared for subsequent least squares analysis, to be carried out by GENLES (least squares refinement program), using the POWPREF program, which maps reflections to data by associating the position, width, incident intensity, refinement weight and a list of contributing reflections with each observation (data point) in a powder pattern. GENLES constructed a single full least squares matrix and vector using multiple data sets. It outputted a summary of the least-squares results on a list file (.LST) and generated an updated version of the experiment file. The diffraction pattern could then be viewed using the powder pattern plotting program, POWPLOT (LIVEPLOT in EXPGUI) which displays observed, calculated and difference curves with reflection markers.

For each data set, the following procedure was carried out manually for one diffraction pattern. Once a satisfactory fit was achieved, the refined patterned was used as a representative to begin refinement of several hundred diffraction patterns in batch mode:
A diffraction pattern from the bulk of the enamel was selected. The background parameter was refined first, lattice parameters and crystallite size (Lorentzian particle broadening term) were refined next. Texture was refined last using the spherical harmonics function and preferred orientation values for the (002) reflections were extracted.

The batch file was written using DOS and was built from a sequential list of EXPEDT commands matching the strict parameter refinement order described above. The goodness of each fit was monitored closely using the value of X^2 (goodness of fit increases as it reaches unity as per equation 3.17) and visual inspection of the plots using the POWPLOT program.

6.3 XMT system (the *MuCAT2* system)

This section describes the particular experimental procedure for collecting X-ray tomography data from tooth samples, and the processing for mineral density quantification of enamel samples. All data were collected using the 4th generation XMT scanner called MuCAT2 (Davis et al., 2010).

MuCAT2 system

The MuCAT2 system uses a conventional impact X-ray source tungsten target. It uses a 225 kV microfocus X-ray generator with 5 μm focal spot size from X-tek, part of Nikon Metrology (Tring, Hertfordshire, UK). The demountable source allows X-ray filaments and targets to be easily changed and thus can be run at a higher power setting than a sealed source with a similar spot size. The specimen and camera are mounted on mechanical stages supplied by Physique Instrumente (Palmbach, Karlsruhe, Germany). A cooled slow scan CCD camera (Spectral Instruments Inc, Tucson, Arizona, USA 800S series) with a 16 megapixel Fairchild CCD485 sensor is coupled via a fibre-optic faceplate to a 100 μm thick columnar caesium iodide scintillator (Applied Scintillation Technologies, Harlow, Essex, UK). The geometric magnification can be varied to give reconstructed voxel (volume element) sizes of between 5 and 30 μm. The temperature inside the X-ray unit is kept at 26°C ± 0.1°C to maintain dimensional stability during each scan.

The detection system comprises of a 100 mm (approximate) columnar caesium iodide scintillator made by Applied Scintillation Technologies (Harlow, Essex, UK), coupled via a parallel optical-fibre faceplate (Davis and Elliott, 2006) to a 800-series thermoelectrically-cooled CCD camera made by Spectral Instruments (Tucson, Arizona). The camera incorporates a 16 megapixel Fairchild CCD485 sensor, of size 60 μm square. This sensor has a pixel size of 15 m, binned initially on the chip and later in software to 60 μm.

6.4 Data collection

As detailed in Chapter 4, 3D tomographic images are a series of 2D projections stacked together. Samples were mounted on the turntable in the path of the X-ray beam so that a

projection could be recorded as the camera moved across the X-ray beam and simultaneously the CCD read out at each incremental rotation angle across 360°. Before each scan, dark and light field reference projections were taken in order to identify systematic errors due to CCD dark current, amplifier offsets and the beam intensity profile. At the end of each scan, data collected was saved as a set of 32-bit floating point values in a .mcd file format, which also contained a text header with scan metadata ready for processing and reconstruction.

Variables affecting data collection, such as the number of projections, exposure time, image resolution, the X-ray tube voltage and current were dependent on the sample being scanned; therefore the particular experimental parameters for each sample measured are specified in the respective chapters.

6.4.1 Calibration

A 10 step Al wedge (Fig. 4.3b) was used to calibrate the system and reduce the effects of beam hardening (as described in Chapter 4). Additionally, a high purity (99.999%) Al wire, approximately 1 mm in diameter (Alfa Aesar) was placed vertically beside every specimen to provide a standard marker LAC measurement (published LAC = 1.5336 cm^{-1} at 40 keV). During the reconstruction stage, average and standard deviation measurements of the Al wire LAC values were taken in order to normalise each voxel of the reconstructed image. Thus for calibration, the LACs of the specimen in the final reconstructed image were normalised to the measured Al LAC at the accelerated voltage.

6.4.2 Data Processing and Reconstruction

Pre-processing stage

The pre-processing stage applied correction for polychromatic radiation to the data contained within the .mcd files collected from MuCAT2 applied. Data was normalised to the monochromatic LAC value of aluminium. This stage applied the dark and light field corrections. Data were corrected so that the values were relative to the accelerating voltage used. Cone beam corrected data were saved as a .con file, and a .cra text file containing the scan metadata (dimensional parameters) was created. A correction for the systematic errors

in horizontal shift and movement of the sample rotation stage was then implemented, based on the procedure described in Davis et al (2010), resulting in the output of an iteratively revised .con file.

Reconstruction stage

An in-house cone beam reconstruction program (ConeRec) was used to apply a modified Feldkamp algorithm to reconstruct the corrected projections, calculating and locating the centre of rotation, which then remained constant, outputting the binary .bin file and the metadata file .siz file, which contained voxel dimensional information. The central slice was reconstructed first due to TDI (Time Delay Integration).

Reconstruction images were trimmed and cropped with the MTRIM.EXE program (run from IDL® Research Systems Inc., Colarado, USA script MTRIM.PRO) to reduce the data volume and convert the reconstructed LAC values to the 256 grey levels (0-255) and to generate X-Y and X-Z projections as well as a grey-level LAC histogram file. The projections were displayed on a 10 x 10 voxel-spaced grid to aid in selection of appropriate cropping values, while the grey levels were plotted as a histogram to allow selection of an appropriate scale factor and greyscale offset. These cropping and greyscale variables were passed to the executable, which outputs the .tom file.

Interactive Data Language, or IDL, is a scientific programming language and development environment (Boulder, Colorado, USA). The language contains a large number of specialised procedures for the manipulation and analysis of large dataset and for displaying results either numerically, in the form of a graph or via an image viewing window.

6.4.3 Visualisation

Reconstructed .tom files could be viewed using various visualisation packages. Single tomographic slices were viewed in Tomview, an in-house analysis tool developed by Dr Graham Davis to read .tom files from *MuCAT2* and present the tomographic dataset in the three Cartesian planes to select individual voxels for LAC readout. A voxel can be defined as the reconstructed volume element with specific dimensions governed by the resolution. ImageJ (Rashband 2006) is an open source image processing program which was used for

quantitative analysis. Drishti (Limaye 2006) is a volume exploration and presentation tool written for visualising tomography and electron microscopy data as 3D rendered image.

Chapter 7: Investigating the Role of Enamelin in the Orientation of Dental Enamel Crystallites during Mineralisation

7.1 Introduction

This chapter aims to elucidate the role of the enamelin protein in the formation of the oriented, hierarchical tissue by characterising the structural properties of human dental enamel from patients affected by the genetic abnormality Amelogenesis Imperfecta (AI), where the precise mutation in the ENAM gene is known. Direct comparisons in mineral concentration, crystallographic texture, lattice parameters and microstructure have been made between healthy human enamel and pathological AI case where the enamelin protein is not present in functional amounts, in order to correlate the physical and clinical phenotype to the genetic lesion.

7.2 Experimental set up

Sample collection and preparation

Exfoliated deciduous enamel sections were donated by R. Shore from Leeds Dental School (Shore et al., 2010). These samples were collected from individuals belonging to different families in northern Sweden with a known mutation in the ENAM gene, resulting in the local hypoplastic form of autosomal dominant (AD) Amelogenesis Imperfecta. The underlying gene defect was characterised as a nonsense mutation g.2382A>T p.K53X (Mardh et al., 2002). Patients from whom these tooth samples were collected were heterozygous with respect to ENAM (Mardh et al., 2002). Specimens were received sectioned longitudinally in the labio-lingual plane, using an Accutom 5 cutter with a peripheral diamond cutting disc and had been polished to a thickness of 50 µm. Type-matched control deciduous teeth were collected with informed consent from patients treated at Barts and the London Dental Hospital paediatric clinics. Teeth were sectioned longitudinally in the labio-lingual plane, using a wet diamond saw. Samples were then polished to achieve a sample thickness of 50 µm using fine grit size silicon carbide paper (P1000, P2500).

A total of 4 deciduous incisor tooth sections (Table 7.1) were measured in this study, which included two local hypoplastic AI (with ENAM mutation) and the type matched control.

Sample	Description	FDI	Anatomical classification
ENAM82	**LOCAL HYPOPLASTIC ENAM MUTATION**	**82**	**Mandibular (second lateral) deciduous incisor right**
ENAM51	**LOCAL HYPOPLASTIC ENAM MUTATION**	**51**	**Maxillary (first central) deciduous incisor right**
HEALTHY82	**CONTROL**	**82**	**Mandibular (second lateral) deciduous incisor right**
HEALTHY51	**CONTROL**	**51**	**Maxillary (first central) deciduous incisor right**

Table 7.1: List of samples measured in this study, describing the phenotypic defects and tooth type.

Mineral concentration

As previous measurements had already been carried out on these samples in order to determine the specific underlying genetic mutation (Mardh et al 2002) and its effect on structure and chemical composition (Shore et al 2010) samples were received sectioned. The enamel sections were mounted onto the flat surface of a Perspex rod (20 mm diameter), with sticky wax and aluminium wire (0.5 mm diameter) attached to the side of the rod (Fig. 7.1). Samples were scanned on the *MuCAT2* system, operated at an accelerating voltage of 60 kV, beam current 0.27 mA, which after beam hardening correction would be equivalent to 35 kV monochromatic radiation. Samples were scanned with a voxel size of 15 µm and reconstructed on a double density grid (7.5 µm voxel size) to prevent loss in resolution during realignment. The scan parameters for each of the samples have been listed in Table 7.2.

Sample	No. of projections	Reconstructed dimensions x, y, z (voxels)	Scan time (hours)
ENAM82	601	538 x 428 x 40	4
ENAM51	601	518 x 308 x 36	4
HEALTHY82	601	570 x 690 x 88	4.5
HEALTHY51	601	790 x 550 x 108	4.5

Table 7.2: Scan parameters for each tooth section, which includes the number of projections, reconstructed dimensions and scan time.

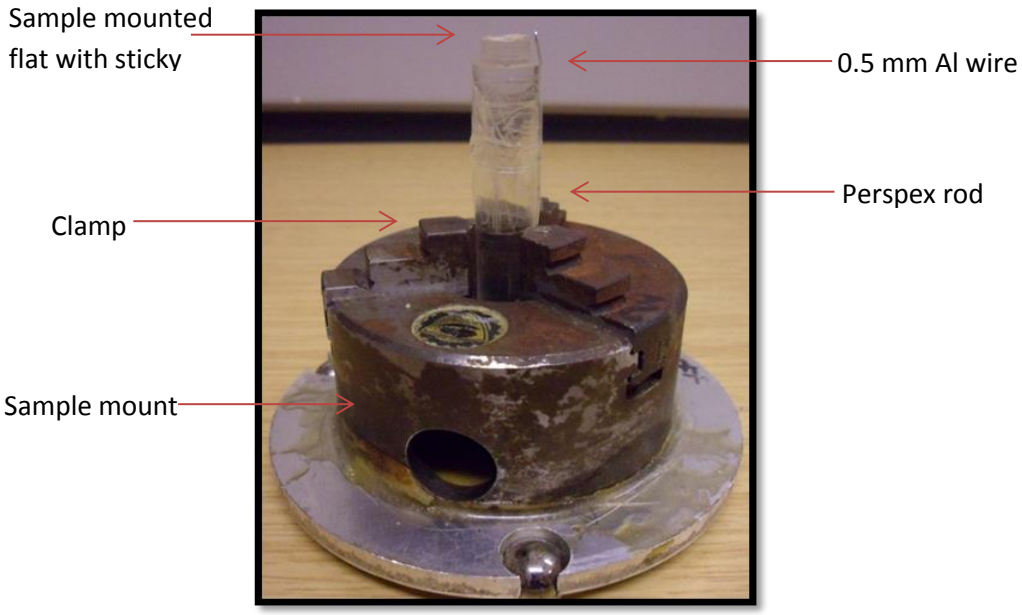

Figure 7.1: Photograph showing method of sample mount on *MuCAT*.

Beamline experimental set up

Intact tooth sections were measured on beamline 2-ID-D at the Advanced Photon Source (APS) (described in chapter 6, section 6.1.2), using X-ray energy of 15.03 keV, equivalent to a wavelength of 0.825 Å (Equation 3.2). Samples were scanned in transmission geometry. Enamel sections were mounted onto an Al plate, and placed on the X-Y-Z scanning stage, to allow movement of the sample perpendicular to the beam direction. A 2048 x 2048 pixel MAR 2D CCD detector was positioned behind the sample such that the sample to detector distance was 162.95 mm to obtain a 2θ range of 5-27^0, this was sufficient to include the main HA peaks, (002), (211) and (300), needed for texture analysis and Rietveld refinement. A micro-beamspot, defined to 10 x 10 µm was directed at the sample and scanned with a 40 µm step size to make an approximate 2 x 4 mm grid of diffraction patterns for each sample. Each diffraction pattern took 16 seconds to collect (including 7 seconds CCD camera processing). Table 7.3 summarises the dimensions of the regions measured and number of diffraction patterns collected for each tooth sample.

Due to the strict time constraints at the facility, only the labial region of each tooth sample (Fig. 7.2) was measured. Focusing on a reduced the region of interest allowed high quality data to be collected at a higher spatial resolution.

Figure 7.2: Schematic representation of a typical deciduous incisor, highlighting the labial side (red box), region measured on the beamline for crystallographic analysis. The red line represents the track for phase analysis (Fig. 7.4).

Sample	No. of diffraction patterns	Dimensions of area measured (mm)	Scan time (hours)
ENAM82	**2052**	**3.8 x 1.4**	**9.5**
ENAM51	**2068**	**4.7 x 1.1**	**9.5**
HEALTHY82	**1200**	**3.8 x 0.8**	**5.5**
HEALTHY51	**1458**	**2.7 x 1.4**	**6.5**

Table 7.3: Table summarising the data collected and time taken for each of the sample measurements.

Texture quantification

Every 2D diffraction pattern containing enamel signal was integrated radially over 360° to create a 1D Intensity vs. 2θ diffraction spectra in preparation for refinement. An instrument parameter file was created using CeO_2 as a standard calibrant. After achieving a good fit for peak shape and position (method described in chapter 6 section 6.2.3), an automated batch processing script was written to input and refine parameters from each data file. The final refined values were extracted and plotted.

Scanning Electron Microscopy

Samples were etched in 35 % orthophosphoric acid for 15 seconds to remove the smear layer. The samples were then washed using distilled water, before being fully dehydrated with graded ethanol 25 %, 50 %, 75 %, 90 % and 3 x absolute for 30 minutes each. Samples were stored in a desiccator overnight then carbon coated. The SEM was operated at 10 kV with a 10 mm working distance.

7.3 Results

Mineral concentration

Figure 7.3 shows a high contrast tomographic XMT virtual slice from each one of the 4 deciduous incisors samples scanned (data collection and reconstruction described in section 6.4). Subtle differences observed in the greyscale describe the general trend in the mineral concentration distribution. The mineral concentration of the enamel samples was determined using equation 4.3, where the LAC of pure HA mineral at 60 kV is 4.39 cm^{-1} (Berger et al 2010). In general, healthy enamel displayed evidence of an increasing mineral concentration gradient from EDJ to surface. Across the entire section measured, mineral concentration was in the range 1.74 - 2.41 g cm^{-3} for HEALTHY82 (Fig. 7.3b) and 2.16 - 2.81 g cm^{-3} for HEALTHY51 (Fig. 7.3d). The enamel appeared to be intact with no particular physical damage. It should be noted that some areas in the healthy enamel (marked with an arrow), such as the tip of HEALTHY82 and a small region on the palatal side of HEALTHY51 were darker. This was not due to lower mineral concentration, but due to partial volume effect. These errors are the result of a loss of contrast in the reconstruction. This was caused by the fact that the section were very thin and were not laid flat enough (slight bending of the thin sections) during scanning.

The mineral concentration of the two AI affected enamel samples ranged from 1.70 - 2.80 g cm^{-3} and 1.30 - 2.74 g cm^{-3} for ENAM82 (Fig. 7.3a) and ENAM51 (Fig. 7.3c) respectively. The same trend was observed in the ENAM enamel as the HEALTHY enamel whereby there was evidence of an increasing mineral concentration from close to the EDJ travelling towards the surface. The tip of ENAM51 (indicated by the red arrow) showed the highest mineral concentration in relation to the rest of the enamel. Few patches of lower mineral concentration were observed throughout the bulk. Severely damaged and cracked regions (highlighted by red boxes), were present on both sides of the enamel. ENAM82 resembled healthy enamel as it was less disrupted than ENAM51, but had a large restoration, identified by the brighter region on the bottom right side (outlined by a blue box). In all samples, areas close to the cemento-enamel junction (CEJ) were more mineralised than towards the cusp. There was a significant difference in the lower mineral concentration

range between ENAM51 (1.30 g cm^{-3}) and its corresponding control sample, HEALTHY51 (2.16 g cm^{-3}). The mineral concentration ENAM51 was much lower than HEALTHY51.

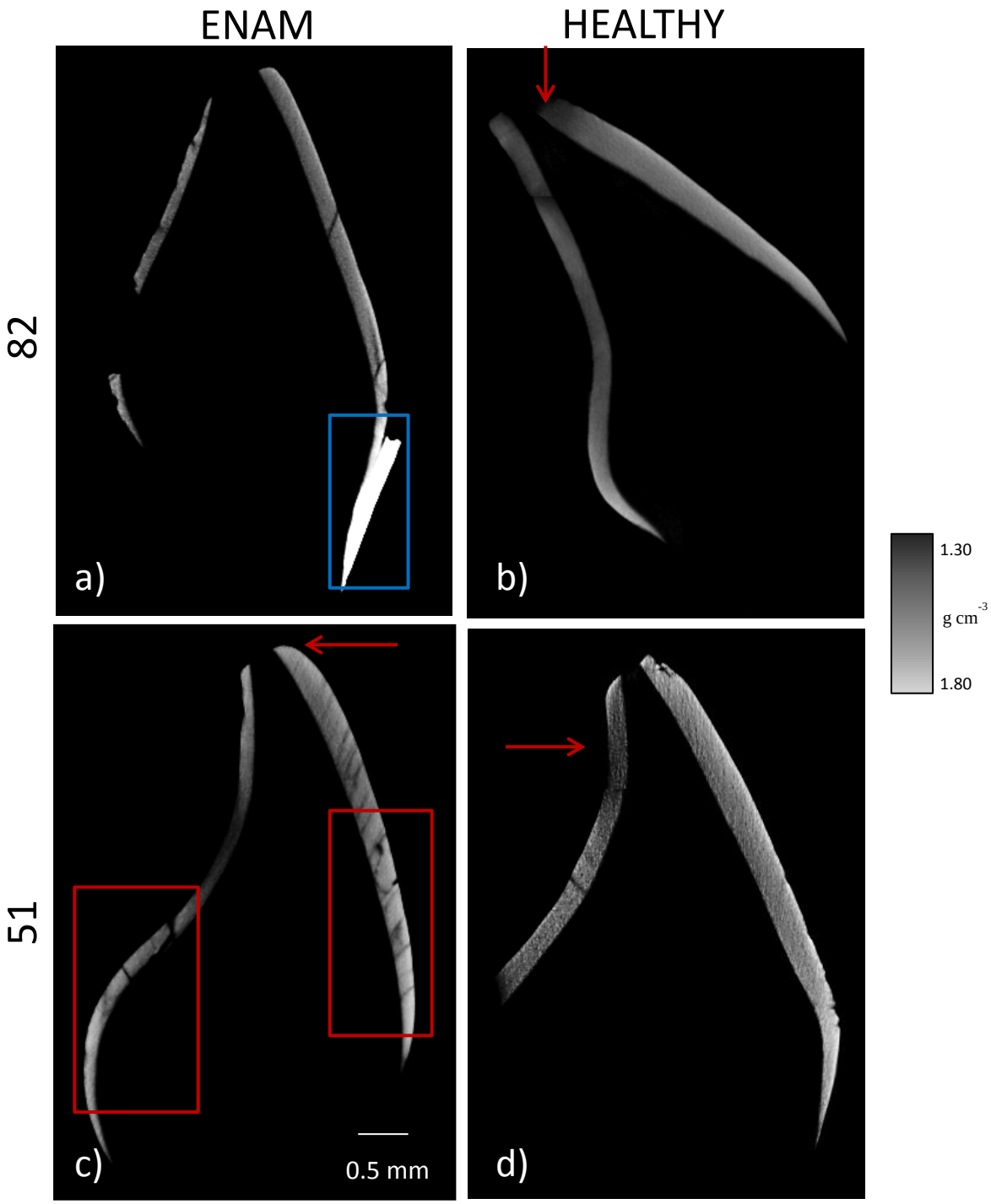

Figure 7.3: High contrast X-ray microtomography images showing the mineral concentration distribution in samples a) ENAM82, b) HEALTHY82, c) ENAM51 and d) HEALTHY51.

Identification of an additional phase

The 1D diffraction patterns of the AI affected enamel samples (ENAM82 and ENAM51) showed the presence of extra Bragg peaks in addition to those attributed to characteristic HA phase, indicating the existence of another phase only in these samples. The two most prominent peaks were present at the 2θ scattering angles 16.6^0 and 18.35^0. The intensity of these peaks relative to the HA peaks was seen to vary as a function of position, generally being more intense in the bulk of the enamel compared to the EDJ and the enamel surface. The intensity of the additional peaks also increased travelling from the tip down towards the CEJ. Figure 7.4 shows a track of diffraction pattern, 0.65 mm below the cusp tip (indicated by the red line in Fig 7.2), taken through the thickness (EDJ to surface) of ENAM82. The additional phase was identified as Whitlockite (WH) ($Ca_9(Mg)(PO_4)_6PO_3OH$), a Mg-substituted calcium phosphate. This was determined by matching powder diffraction patterns. Although other phases, such as monotite and tricalcium phosphate were likely matches to the observed data, WH had the best crystallographic fit. WH has a rhombohedral crystal structure in the space group R3c (Trigonal crystal system, 3 glide translations) with lattice parameters a = 10.35 Å and c = 37.085 Å. The WH phase was only observed in the ENAM mutated enamel and not at all in the control samples. All the WH reflections between 2θ range 8-26° are displayed in Figure 7.6, indicated by cyan tick marks.

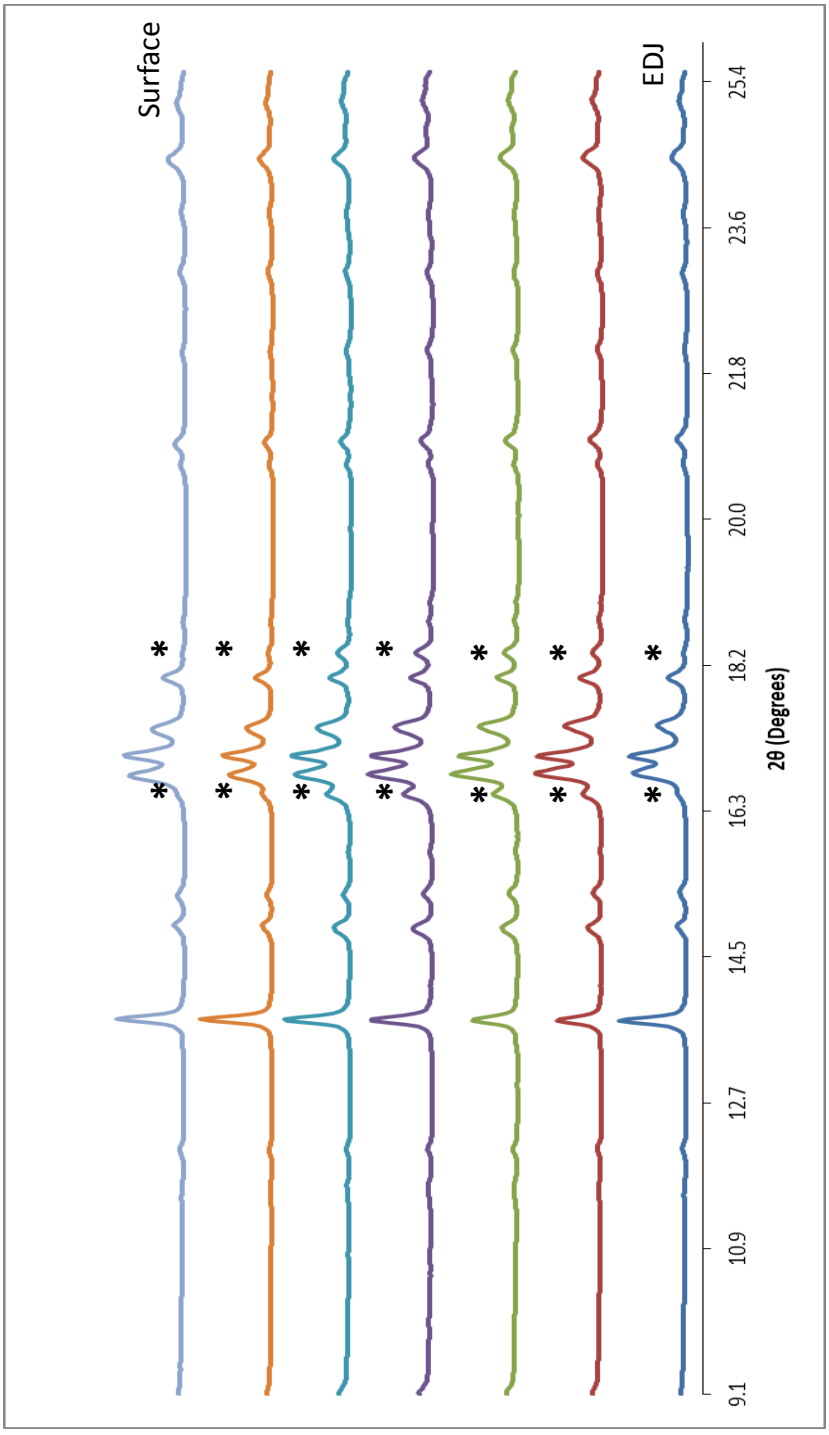

Figure 7.4: Diffraction spectra showing the presence of an extra phase, identified by two prominent peaks (marked with an asterisk). The additional phase was observed only in the ENAM mutated enamel. Changes in peak intensity occurred as a function of position from enamel surface to EDJ.

Figure 7.5 shows the changes in the relative weight fraction (W_p) of the two phases, WH and HA, from surface to EDJ. The track is representative of that shown in Figure 7.4, taken from ENAM82. The W_p (Equation 3.18) for multiphase mixtures were automatically computed during the least-squares refinement using the GSAS software.

The graph (Fig. 7.5) shows the bulk of the enamel, between 75 µm and 125 µm, had the highest W_p of WH in comparison to the surface and the EDJ. The error bars lie within the data points and describe the uncertainty in fitting during refinement.

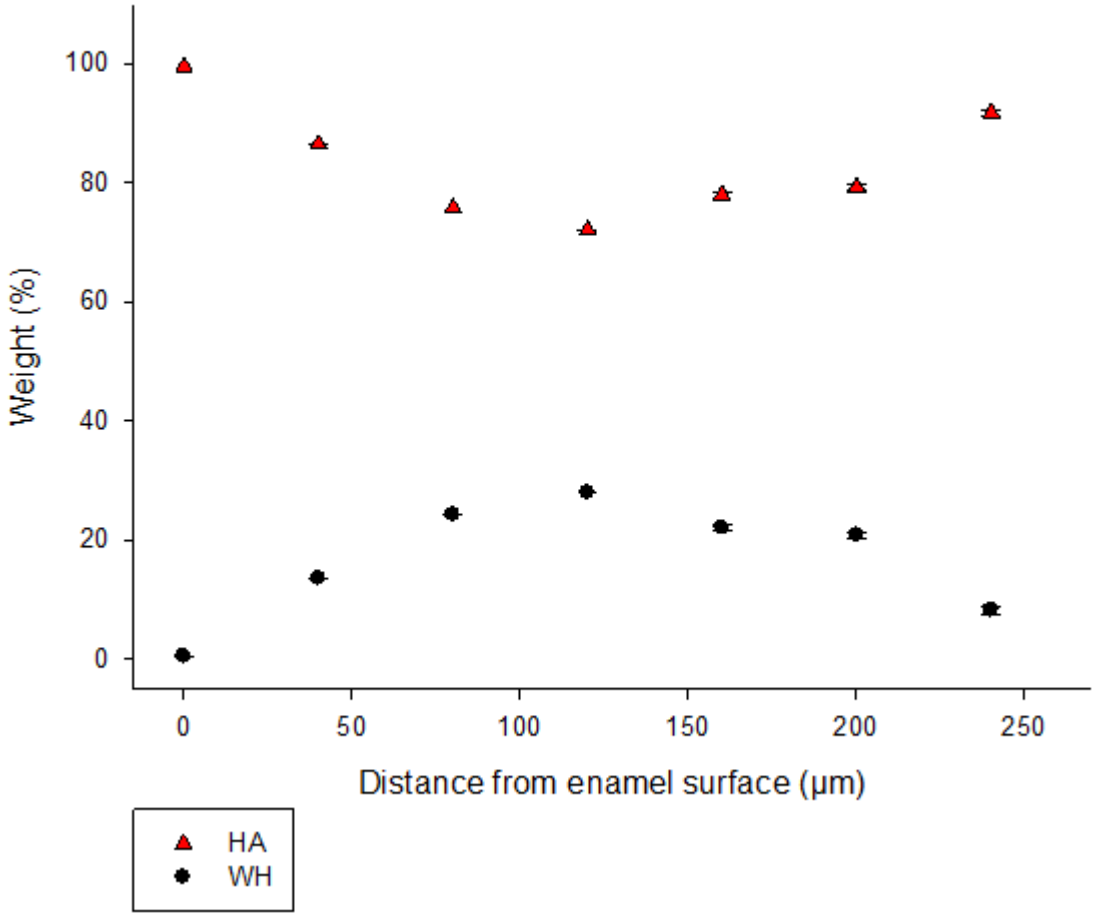

Figure 7.5: Graph showing the relative percentage of Whitlockite and Hydroxyapatie in ENAM82 enamel as a function of position.

Crystallite preferred orientation

The magnitude of preferred orientation within the samples was determined by refining each enamel diffraction pattern. Figure 7.6 and Figure 7.7 show the typical refinements of a 1D diffraction pattern taken from a similar region in the AI affected and healthy enamel respectively. The crosses represent the observed data points; the solid line represents the calculated diffraction pattern. The tick marks below the diffraction pattern indicate the positions of the calculated HA (pink) and WH (cyan) Bragg peaks and beneath is the difference plot of the calculated and the observed profiles. Note, only the AI affected samples were refined with both HA and WH since there was no evidence of WH in the healthy enamel. Furthermore, only texture of HA was studied. The refined crystallographic parameters from the two files are listed in Table 7.4. The low X^2 value (<1.0) is likely to be due to an overestimation in the standard uncertainties, such as summation of data when converted into 1D underestimating the collection statistics.

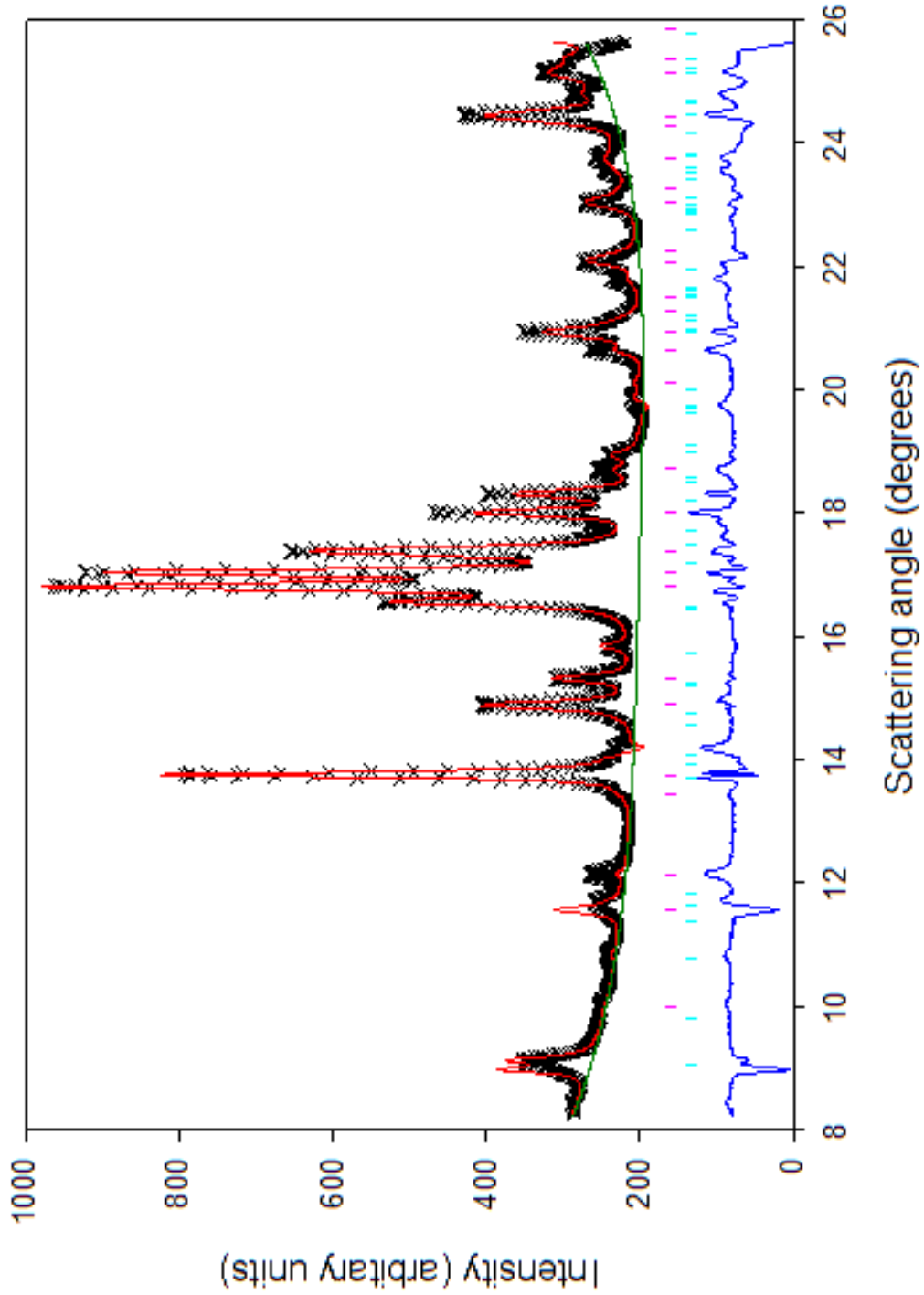

Figure 7.6: Rietveld refinement of a 1D diffraction pattern, taken from ENAM82. This shows the observed data (crosses), the calculated diffraction pattern (red solid line), the difference curve (blue solid line) and the tick marks indicating the 2θ peak positions for the calculated diffraction pattern of HA (pink) and WH (cyan).

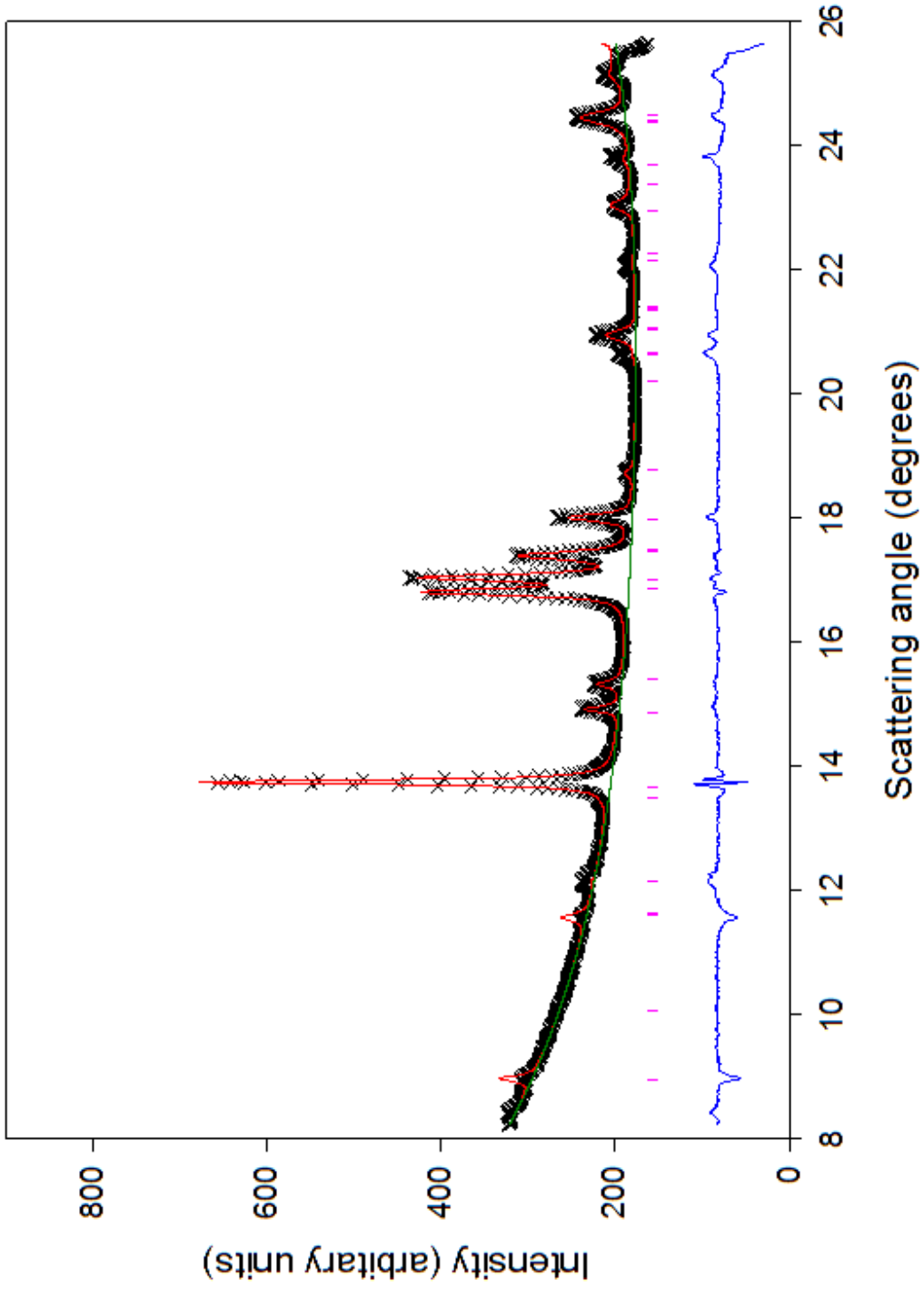

Figure 7.7: Rietveld refinement of a 1D diffraction pattern, taken from HEALTHY82. This shows the observed data (crosses), the calculated diffraction pattern (red solid line), the difference curve (blue solid line) and the tick marks indicating the 2θ peak positions for the calculated diffraction pattern of HA (pink).

Parameter	Hypoplastic enamel	Healthy enamel
Space group	$P6_3/m$ & R3c	$P6_3/m$
HA a lattice parameter (Å)	9.4471 ($\pm 3.98 \times 10^{-4}$)	9.4470 ($\pm 4.38 \times 10^{-4}$)
HA c lattice parameter (Å)	6.8870 ($\pm 3.38 \times 10^{-4}$)	6.8892 ($\pm 1.86 \times 10^{-4}$)
α, β, γ lattice angles (^{0})	α=β=90°,γ= 120°	α=β=90°,γ= 120°
WH a lattice parameter (Å)	10.3622 ($\pm 1.03 \times 10^{-3}$)	NA
WH c lattice parameter (Å)	37.1696 ($\pm 5.15 \times 10^{-3}$)	NA
$(002)_{(SH)}$ (for HA)	2.17 ($\pm 1.00 \times 10^{-1}$)	2.85 ($\pm 1.27 \times 10^{-1}$)
X^2 Chi	0.6	0.2

Table 7.4: Refined structural parameters, with errors in brackets, for a typical diffraction pattern of ENAM mutated and healthy enamel.

Crystallite texture in the labial side of deciduous incisor sections was quantified using the Rietveld refinement method. The 002 reflection exhibits the greatest variation in intensity (strongest variation). Thus, for each enamel diffraction pattern, the 002 texture coefficient (C_2^{00}) was extracted to produce a 2D spatial distribution contour map. Figure 7.8 represents the change in the magnitude of crystallite preferred orientation in the 002 diffraction peak for each tooth sample. The 2D maps were created using the spherical harmonics function to obtain preferred orientation (Equation 3.7). Values extracted from the equation describe the degree of crystallite preferred orientation. Higher values represent greater alignment. Although a clear difference was observed in the crystallographic texture distribution pattern between the AI affected enamel and the healthy enamel, all samples displayed evidence of an anisotropic crystallite arrangement.

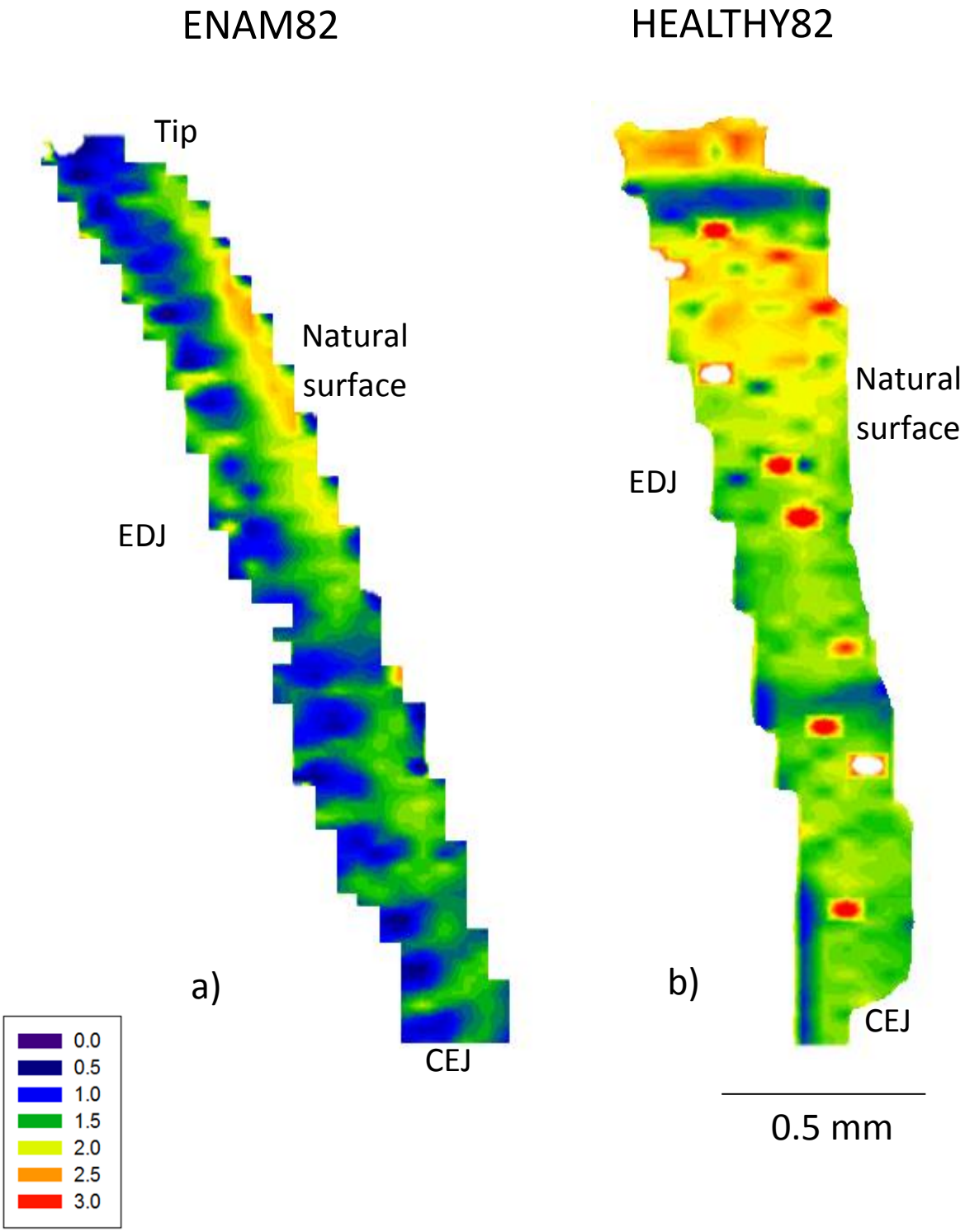
ENAM82
HEALTHY82
Tip
Natural surface
EDJ
CEJ
a)
b)
Natural surface
EDJ
CEJ
0.0
0.5
1.0
1.5
2.0
2.5
3.0
0.5 mm

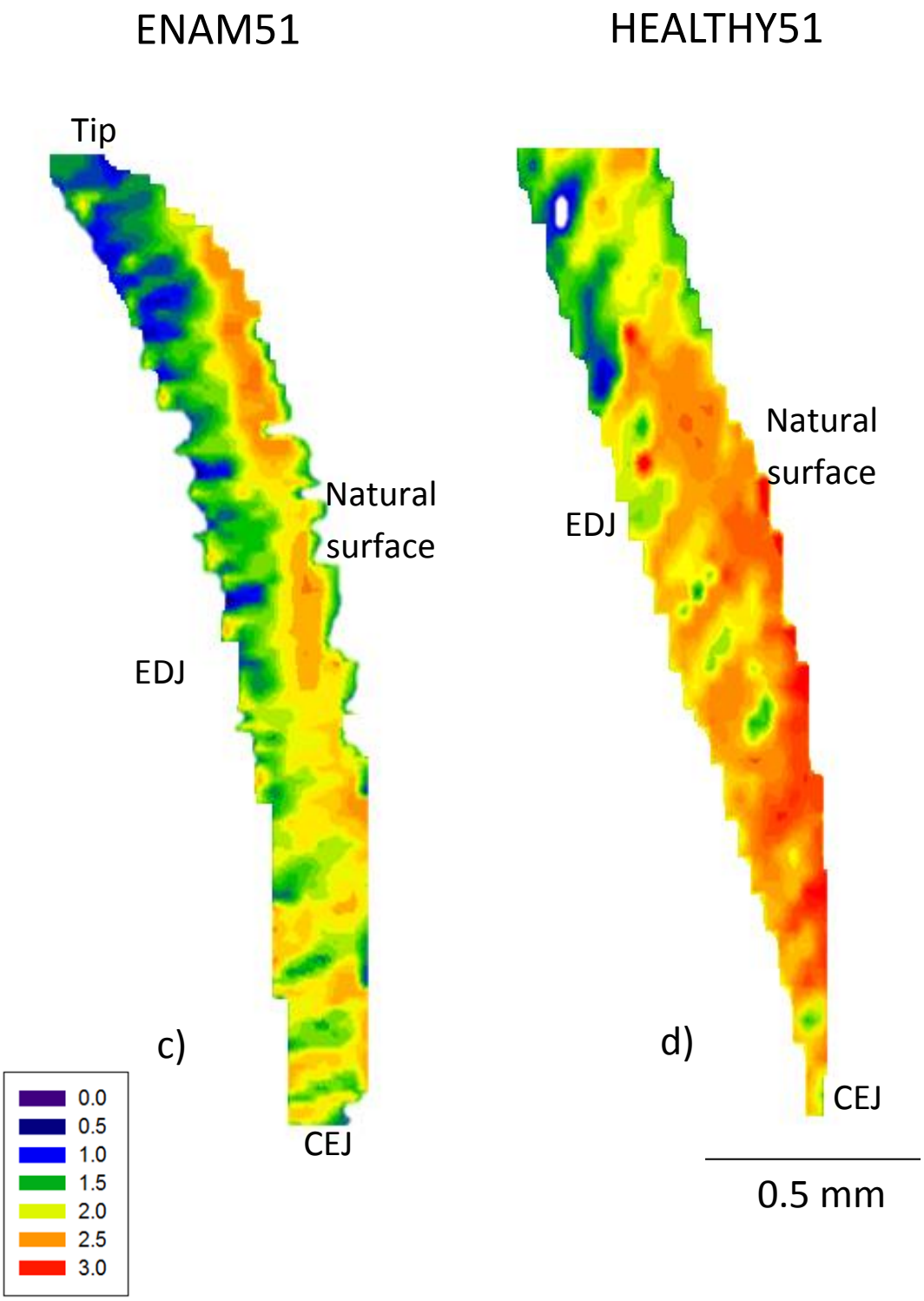

Figure 7.8: Texture distribution contour maps showing the magnitude of preferred orientation in the (002) reflection of the HA phase along the labial region of a) ENAM82 b) HEALTHY82 c) ENAM51 and d) HEALTHY51.

The AI affected, hypoplastic enamel (Fig. 7.8a and c) displayed similar traits to one another, and that is, a generally lower texture distribution compared to their type matched healthy control (Fig. 7.8b and d). A lack of preferred orientation was seen across the entire region of ENAM82, with the exception of an area close to the surface in the top half, below the tip. The lowest degree of preferred orientation in the ENAM51 enamel was seen at the tip of the tooth and close to the EDJ in the top third from the tip. The surface and region close to the CEJ showed higher values of preferred orientation parameter. Within the strongly textured areas, heterogeneity was observed, with regions of lower texture. Crystallites in the healthy enamel were highly ordered and aligned, giving it a high degree of crystallographic texture. Greatest texture was seen in the upper third of the HEALTHY82 enamel and the lower region of HEALTHY51. In HEALTHY51 the region with preferred orientation was almost homogenous.

HA Lattice parameters

The *a*- and *c*- lattice parameter values were extracted from the Rietveld refinement procedure described above. The contour maps presented in Figure 7.9 and Figure 7.10 show the spatial trend in the *a*- and *c*- lattice parameters respectively in the measured enamel samples. Although the AI affected enamel presents lower lattice parameter values than healthy enamel, the general spatial trend was the same as that of healthy enamel, whereby *a*-lattice parameter increases and the *c*-lattice parameter decreases moving away from the EDJ and towards the enamel surface. The data files was analysed in small independent batches, therefore these trends are real and not an artefact of the data analysis order.

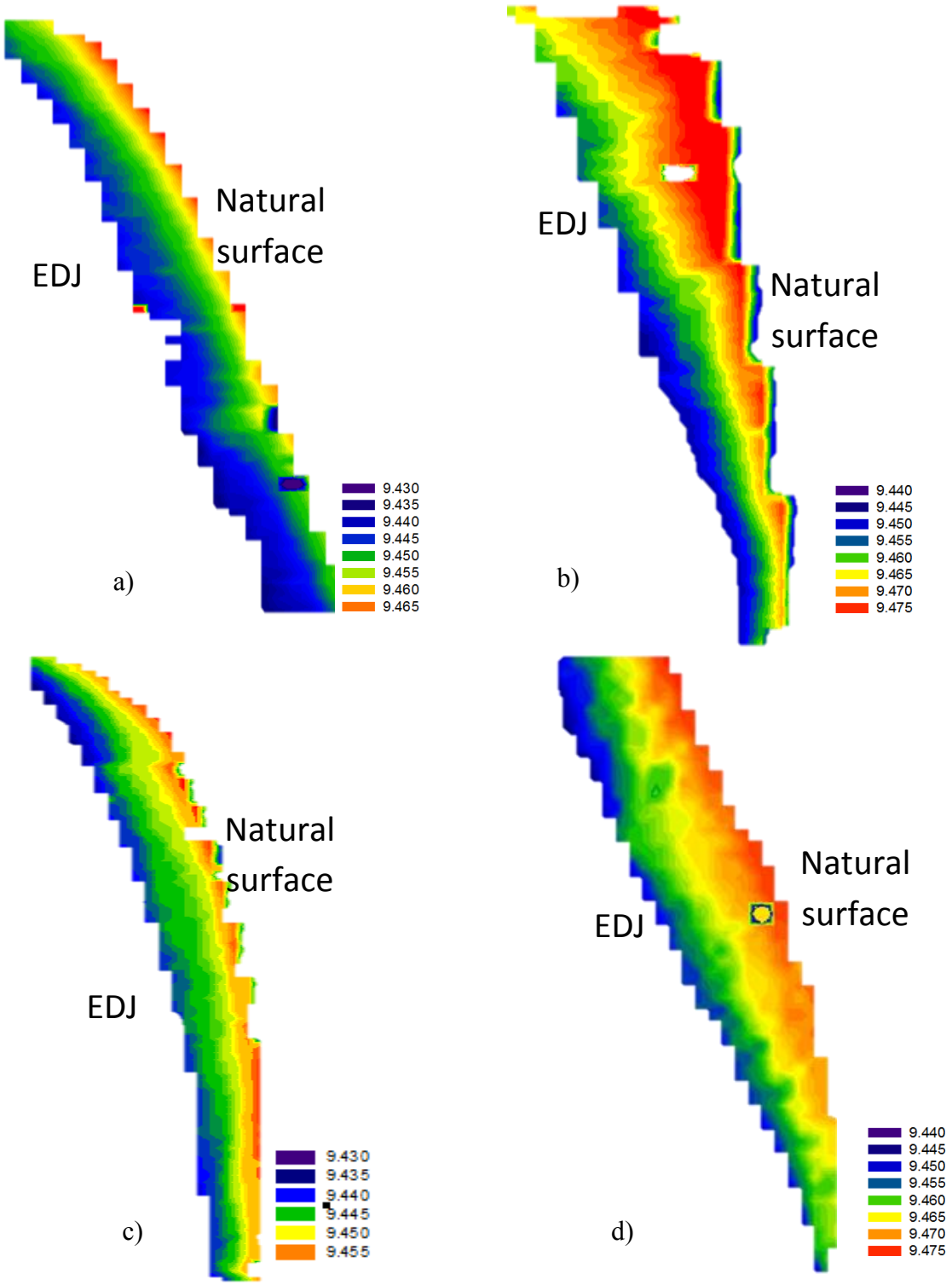

Figure 7.9: *a* lattice parameter contour maps as a function of position for a) ENAM82 b) HEALTHY82 c) ENAM51 and d) HEALTHY51.

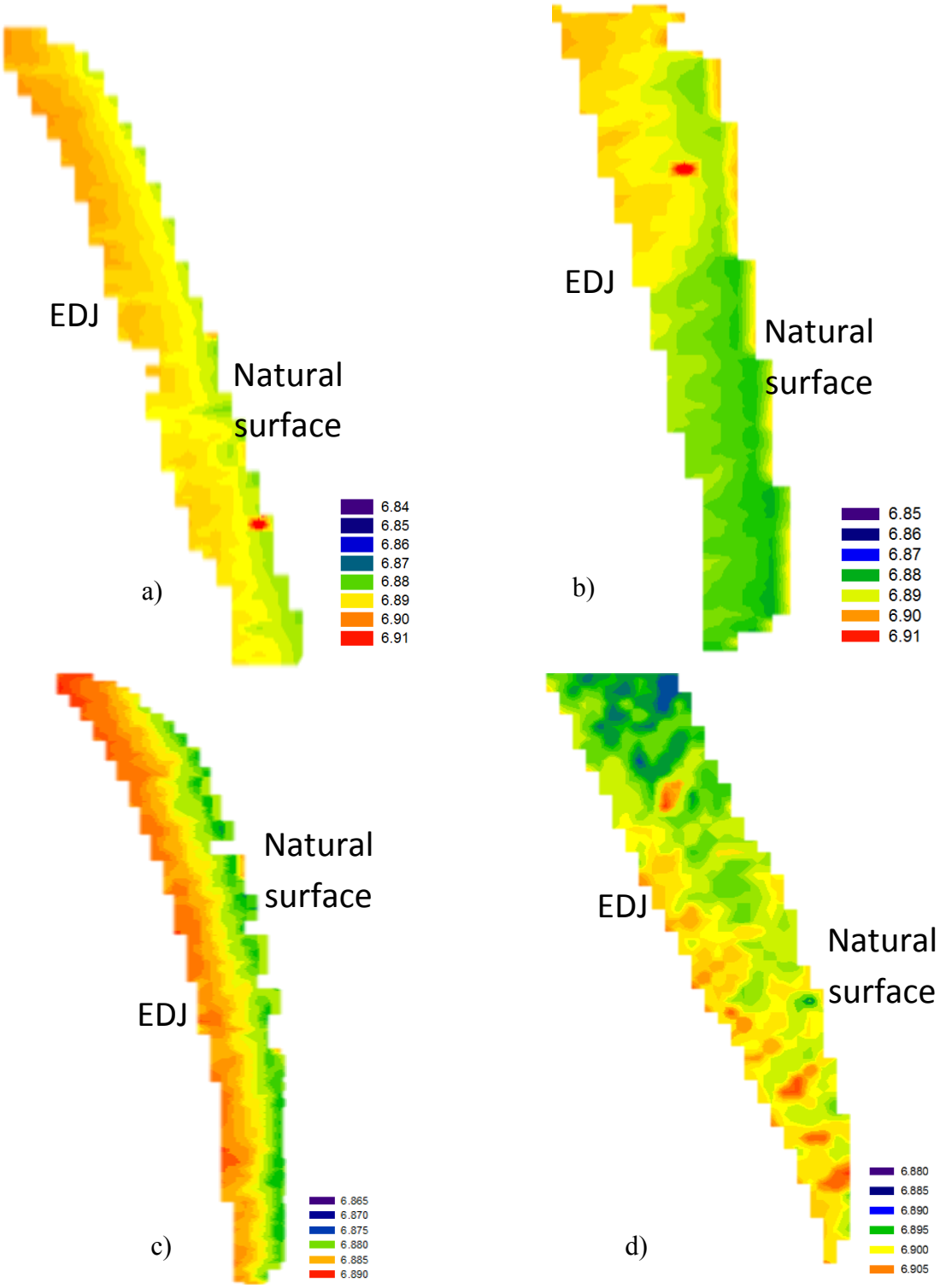

Figure 7.10: *c* lattice parameter contour maps as a function of position for a) ENAM82 b) HEALTHY82 c) ENAM51 and d) HEALTHY51.

Enamel microstructure

The scanning electron micrographs (Fig. 7.11) show the microstructural organisation of ENAM82 (Fig. 7.11a), HEALTHY82 (Fig. 7.11b), ENAM51 (Fig. 7.11c) and HEALTHY51 (Fig. 7.10d). Images were taken from the bulk of the enamel samples.

AI affected enamel exhibited an overall lack of microstructural organisation and a fusion of crystallites without distinctive boundaries, giving an amorphous appearance. Healthy enamel on the other hand exhibited tightly packed ordered crystals with distinct boundaries and the presence of a prismatic structure.

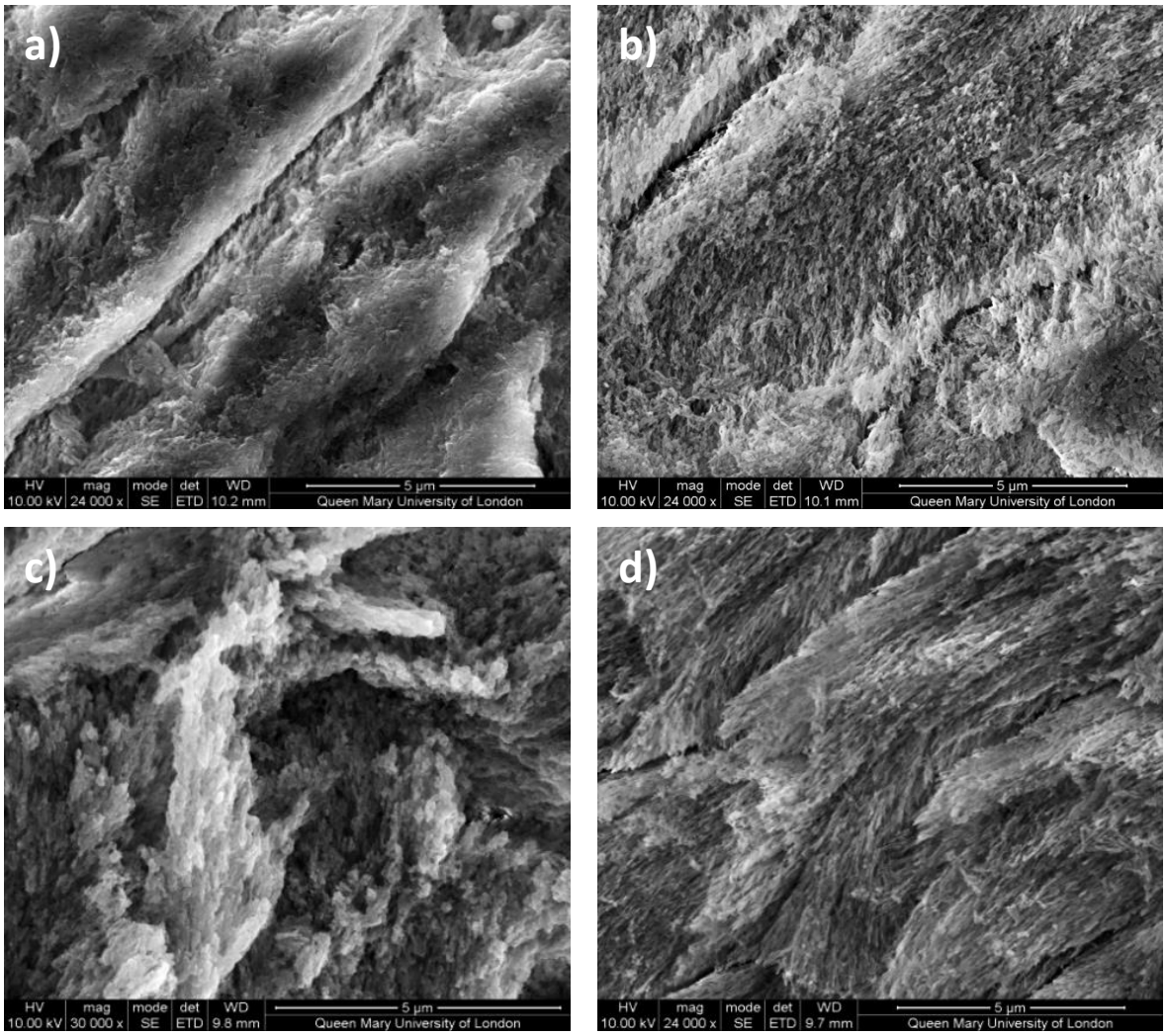

Figure 7.11: Scanning electron micrographs of a) ENAM82, b) HEALTHY82, c) ENAM51 and d) HEALTHY51, showing the difference in microstructure between AI affected and healthy enamel.

7.4 Discussion

Amelogenesis is a complex extracellular process that regulates the nucleation, growth and organisation of enamel crystallites to produce a highly mineralised material with a unique hierarchal structure. This chapter focused on understanding the initial stage of enamel formation, the secretory stage, which involves secretion of an organic matrix by the ameloblasts, composed of proteins, and acts as a structural framework. The matrix plays an important role in the mechanical design of biomineralised tissues during enamel formation (Mann, 2001).

At a molecular level, enamel biomineralisation is regulated by the interaction between the abundant hydrophobic amelogenin and the hydrophilic enamelin molecules, the former provides a skeletal framework and the latter is involved in controlling the crystal nucleation and growth. The hydrophobic and hydrophilic proteins account for both the structural and functional constituents of the matrix respectively (Margolis et al., 2006). Enamelin is one of two non-amelogenin proteins, the other being ameloblastin, secreted by the ameloblasts during the secretory stage of Amelogenesis. The presence of glycine, aspartic and serine makes enamelin an acidic glycoprotein, controlling crystallite nucleation. The intact protein is only observed at the mineralisation front, suggesting it also plays a role in crystallite elongation (Hu and Yamakoshi, 2003).

From the results presented in this chapter, the most striking difference seen between the affected and healthy enamel was in the preferred orientation (Fig. 7.8) and microstructural organisation (Fig. 7.11), which validate that enamelin protein is an integral part in structural organisation in the organic matrix mediated biomineralisation. All samples showed some level of heterogeneity in the crystallite alignment. Gradation of enamel crystallite orientation has previously been seen in a healthy deciduous incisor tissue (Al-Jawad et al 2012). Consistency in the texture pattern shown in the two hypoplastic AI samples (ENAM82 AND ENAM51) indicates that the ENAM mutation which produces a truncated protein has a disruptive effect localised at the incisor tip and EDJ region. The effect of the mutation was not seen at the surface region of the samples, where enamel was strongly textured. This shows that a degree of functionality is maintained at surface. This is likely to

be due to the amelogenin compensating for the defective enamelin, as it has the potential to function independently by self-assembling into uniform nanospheres to control the growth and spatial organisation of the crystallites (Fincham et al., 1995). Very little correlation was seen in the mineral concentration and preferred orientation of ENAM82 and HEALTHY82. Similarities in the mineral concentration range, (Fig. 7.3) between the ENAM (AI affected samples) and their type-matched healthy control enamel, imply that a healthy level of mineralisation can potentially be achieved, even in the absence of a fully functional enamelin protein. This also shows that this particular ENAM mutation does not influence nucleation of crystallites during the secretory stage. Additionally, AI samples follow the same trend as healthy enamel, which emphasises that crystallite chemistry was not affected by the mutation. The small variation in the lattice parameters can be attributed to the impure nature of the carbonated apatite. From this it can be deduced that a nonsense mutation in the ENAM gene simply alters crystallite packing and organisation.

The extra phase present in the enamel of the AI affected enamel was identified as Whitlockite. As WH was observed across the entire region, most prominent in the bulk of the enamel, it is likely to be a developmental feature rather than just the remnants of calculus from the oral environment. The build-up of this can be due to the increased porosity and lack of texture in the AI enamel. In addition, the presence of Magnesium within the enamel prevents crystallite growth and elongation resulting in defective hypoplastic enamel.

The necessity of enamelin in the matrix during enamel formation was demonstrated in human enamel (Pavlic et al 2007) and using ENAM-null mice, whereby enamel is completely absent as mineralisation in the matrix did not occur (Hu et al. 2008). ENAM mutation is dose dependent (Wright et al., 1992). Enamel phenotype is more severely affected if both alleles are affected rather than the one. Samples measured in this study were from patients who are heterozygous (Mardh et al 2002) for this nonsense mutation. Therefore regions of healthy mineralised and aligned crystallites are still present.

The likely reason for differences in ENAM51 and ENAM82 is varying severity of symptoms in different individuals. This would imply that the same mutation can affect different individuals differently.

The variation in mineral concentration range in the healthy enamel suggests inter tooth differences. HEALTHY51 displays a higher mineral range than HEALTHY82, which may be due to tooth position, 51 is a central incisor whereas 82 is lateral. Similarities in the mineral concentration range, (Fig. 7.3) between the ENAM (AI affected samples) and their type-matched healthy control enamel, imply that a healthy level of mineralisation can potentially be achieved, even in the absence of a fully functional enamelin protein. This also shows that this particular ENAM mutation does not influence nucleation of crystallites during the secretory stage.

When comparing the mineral concentration range of ENAM82 with HEALTHY82, it can be seen that the bottom range of the affected enamel is only slightly lower than that of its corresponding control; however the upper range is in fact higher than healthy enamel. In contrast to this, the range of ENAM51 was overall lower than HEALTHY51, suggesting mineralisation varies from tooth to tooth.

Whitlockite has very recently been found in developing enamel. Therefore the presence of this phase is AI enamel could be giving information about the developmental disruption. If the normal biomineralisation route is WH to HA, perhaps the enamel doesn't fully convert from WH to HA as it is supposed to in these AI subtypes.

HEALTHY82 and HEALTHY51 have different texture distributions. 82s were both lower than 51s. This has been seen in different tooth morphologies in permanent dentition previously (Al-Jawad et al., 2007, Simmons et al, 2013). This highlights the importance of choosing a type-matched control and the need to evaluate texture spatial distribution in healthy enamel as well as affected, even when all are incisors.

7.5 Conclusions

Specialised X-ray techniques were used to study the variation in enamel microstructure in enamel affected by local hypoplastic AI with known mutation in the ENAM gene. Results support the idea that functional enamelin is required for correct crystallite organisation throughout the bulk of the enamel. A nonsense mutation in the ENAM gene produces a protein that is capable of interacting with amelogenin to nucleate crystallites to a near healthy mineral concentration.

Chapter 8: Physical Characteristics of Enamel Affected by Hypomaturation Amelogenesis Imperfecta

8.1 Introduction

The purpose of this study was to characterise the structural properties of human dental enamel clinically diagnosed with the pathological hypomaturation subtype of Amelogenesis Imperfecta (AI), by quantifying the spatial distribution of preferred orientation and mineral concentration and relating these to the clinical phenotype. Defining the defects that occur during the intricate stage of enamel maturation can improve understanding of this disorder as well as provide a unique opportunity to identify the developmental pathways required for normal tooth development and give insights into the basic principles underlying this extreme case of mammalian biomineralisation.

8.2 Experimental setup

Sample collection and preparation

Three intact human maxillary first premolar samples were used in this study, two clinically diagnosed with the hypomaturation subtype of AI (labelled HYPO1 and HYPO2) and one type matched sound sample (HEALTHY). All enamel samples for this study were collected with informed consent from patients being treated at Barts and The London Dental hospital. After extraction, teeth were stored in 70% ethanol.

Mineral concentration measurements were first taken on the whole tooth samples using XMT, before each tooth sample was sectioned longitudinally using a wet diamond blade to approximately 200 µm and then further polished to achieve a thickness of approximately 60 µm for texture analysis using SXRD.

MuCAT2 setup

Whole tooth samples were scanned on the MuCAT2 system (Section 6.3). The roots of each tooth were securely wrapped in cotton wool and placed into a plastic tube and covered with a lid, to secure the tooth from any movement and ensure stability during scanning. A

0.5 mm thick, Al wire was placed next to each sample within the plastic tube for accurate calibration. The plastic tube was mounted onto the removable kinematic stage with the long axis of the tooth parallel to the axis of rotation for the XMT.

The system was operated at an accelerating voltage of 90 kV, 0.18 mA, which after beam hardening correction would be equivalent to 40 kV monochromatic radiation. An X-ray filter comprising of a 1.2mm thick Al and 0.5 mm thick Cu sheet was inserted in front of the beam to reduce the spectral spread. Samples were measured with a voxel size of 30 µm each taking approximately 4.5 hours scan time.

The scan parameters for each sample have been listed in Table 8.1.

Sample	No. of projections	Reconstructed dimensions x, y, z (voxels)	Scan time (hours)
HYPO1	**601**	**338 x 258 x 649**	**4.5**
HYPO2	**601**	**388 x 258 x 628**	**4.5**
HEALTHY	**601**	**368 x 258 x 679**	**4.5**

Table 8.1: Scan parameters for each tooth section, which includes the number of projections, reconstructed dimensions and scan time.

Beamline experimental setup

An X-ray energy of 15.1 keV, equivalent to a wavelength of 0.82 Å was used with a beam spot size of 150 x 150 µm. 2D diffraction patterns were collected with a 2048 x 2048 MAR CCD detector positioned behind the specimen at a distance of 173 mm allowing a 2θ range of 5-25°. Beam time was allocated in 16 bunch mode, where 16 highly populated and equally spaced electron bunches circulate, during this mode the ring is filled approximately every 8 hours. The intensity of the beam reaches 90 mA and has a lifetime of 10 hours. Lanthanum hexaboride (LaB_6) was used as a calibrant. A whole crown section (approximately 60 µm thick) taken from middle region of each tooth sample was measured on the XMaS beamline at the ESRF (setup described in section 6.1.1). Sections were mounted onto a glass slide and placed on to a travelling platform (Fig. 8.1), moving in two orthogonal directions perpendicular to the beam. A diffraction pattern was collected every 13 seconds (5 seconds counting time and 8 seconds CCD camera processing time).

A total of 3408 diffraction patterns were collected for the two affected tooth specimens, including air, enamel and dentine patterns (1920 patterns for HYPO1 and 1488 patterns for HYPO2). A 4.5 mm x 9.6 mm and 3.6 mm x 9.3 mm grid was constructed for HYPO1 and HYPO2 respectively, taking approximately 6.5 hours to measure each section.

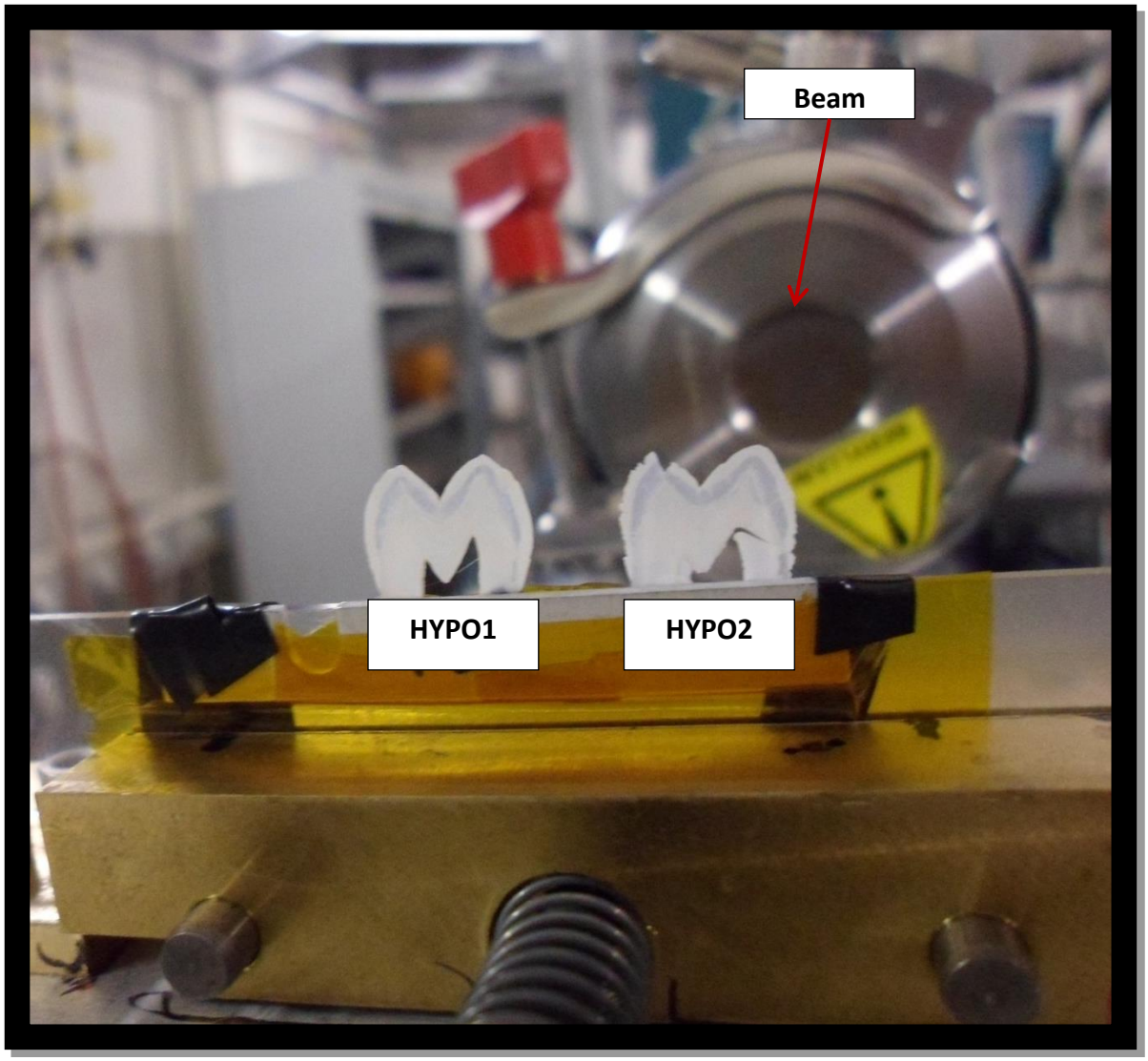

Figure 8.1: Photograph to show HYPO1 (left) and HYPO2 (right) sections mounted on a glass slide and placed on the travelling platform in front of the beam on the XMaS beamline.

8.3 Results

Mineral concentration

By applying equation 4.3 (LAC of pure HA mineral at 90 kV is 3.15 g cm^{-1} (Berger et al 2010)) to the 2D and 3D images obtained from the tomographic data, it was possible to determine quantitatively the spatial distribution of mineral concentration in the enamel. This is given in the scale-bar accompanying each Figure. Figure 8.2 is a 3D representation of each of the three samples measured; these images were produced using the Drishti visualisation software. Although rendered 3D images of the dataset generally only allow qualitative evaluation of the scanned samples, a colour contour was added to the surface of the crown using thresholds to observe the mineral concentration distribution across the outer layer of the enamel, as this was the region most likely to be affected by hypomaturation. It should be noted that the thresholds added mark the lower range of mineral concentration below 2.2 g cm^{-3}. The white regions represent higher mineral concentration. A clear difference is seen in both the topography of the outer surface and in the mineral concentration at the surface between the hypomature and healthy enamel. HYPO1 (Fig. 8.2a) and HYPO2 (Fig. 8.2b) enamel exhibit lower mineral concentration across the surface of the entire crown compared to HEALTHY (Fig. 8.2c) enamel. The HEALTHY tooth (Fig. 8.2c) displays sound enamel, with no visible surface damage. Areas of slightly low concentration (approximately 2.2 g cm^{-3}) are seen at the tip of the buccal cusp, in the fissure and at the lower surface (red arrows). It should be noted that these regions are generally highly susceptible to demineralisation.

HYPO1 (Fig. 8.2a) displayed severe wear and damage by surface loss of enamel, most prominently around the lingual cusp (marked by an arrow). The positions of the chipped enamel do not correspond with the position of damage that can be caused during tooth extraction (lower on the tooth crown, close to the root). This confirms that these physical defects are real effects of hypomaturation, not a result of extraction. Chipping of the enamel suggests a weak and brittle surface, which can correlate to the particularly low mineral concentration in that region. HYPO2 (Fig. 8.2b), similarly exhibits overall low mineral

concentration, with some regions more greatly affected than others, including the cervical regions. No further physical defects were observed on the hypomature enamel surface.

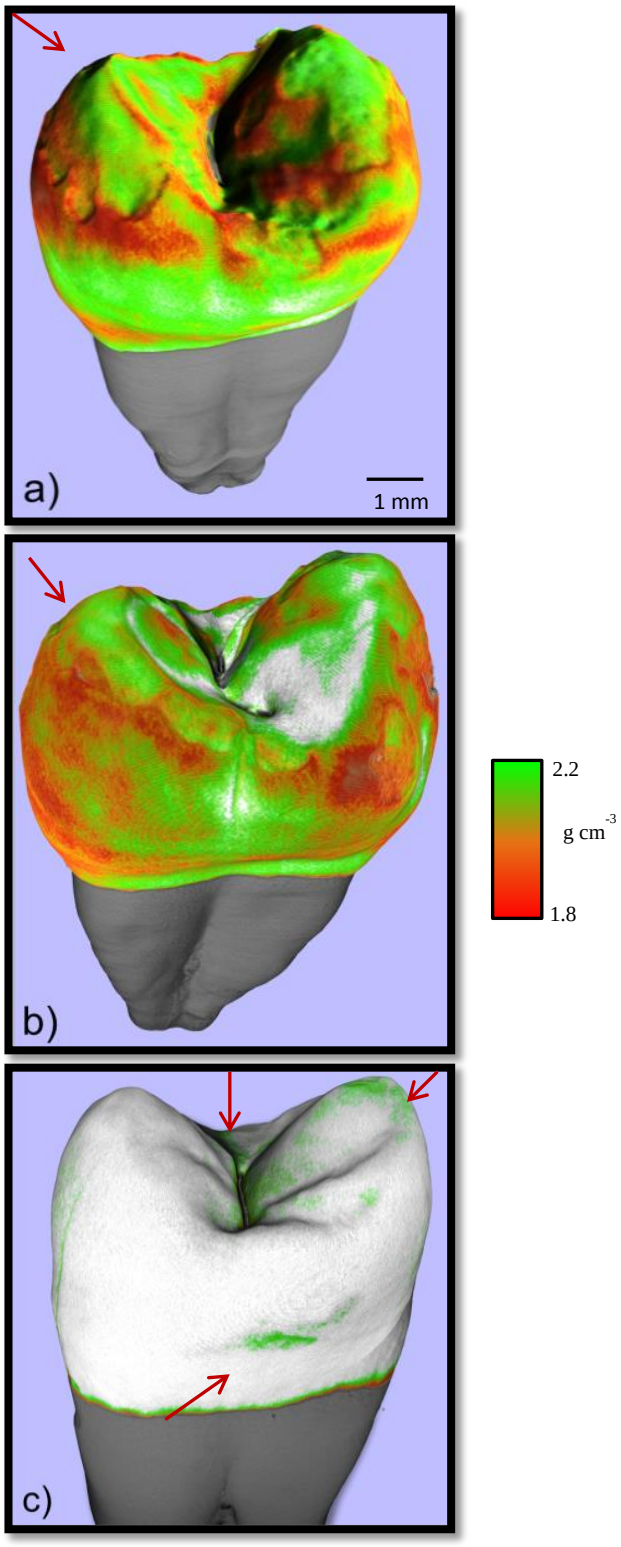

Figure 8.2: Surface rendered 3D image representing a) HYPO1 b) HYPO2 and c) HEALTHY enamel.

Figure 8.3 and Figure 8.4 show high contrast XMT slices taken from the occlusal (XY) and longitudinal (XZ) plane of each scanned tooth sample respectively. The 2D images provide valuable information of the internal structure and mineral concentration distribution, allowing any subsurface defects to become visible. The images in Figure 8.3 represent the occlusal plane of HYPO1 (Fig. 8.3a), HYPO2 (Fig. 8.3b) and HEALTHY approximately 2.2 mm below the buccal cusp tip. An interesting feature was observed in HYPO1 and HYPO2; a dark band was present around the entire enamel surface forming a halo-like outer layer. This band was quite uniform in thickness (approximately 0.8 mm) and almost completely covered the bulk enamel in a lower mineral concentration surface layer of 1.70 g cm^{-3}. No other abnormalities in mineral density were seen in the hypomature enamel. Furthermore HYPO1 and HYPO2 exhibited similar enamel thickness to HEALTHY (Fig. 8.3c) enamel. The HEALTHY enamel displays a sound and mineralised surface layer, with the presence of a slight decreasing gradient in the grey level from surface to EDJ.

The 2D tomography slices presented in Figure 8.4 were taken from the mid region of HYPO1 (Fig. 8.4a), HYPO2 (Fig. 8.4b) and HEALTHY (Fig. 8.4c). The greyscale distribution implies that HYPO1 and HYPO2 have an overall lower mineral concentration in comparison to HEALTHY enamel. The longitudinal cross sections show similar features to Figure 8.3, whereby the surface of HYPO1 and HYPO2 show the same darker band. The surface regions which are not darker (close to both cusps) correspond to the areas of chipped enamel seen in the 3D reconstructed images (Fig. 8.2a and Fig 8.2b). Once again, there was no evidence of any further damage. In the HEALTHY (Fig. 8.2c) enamel a large crack was seen spanning out from the lingual pulp horn towards the surface close to the CEJ. This feature seen was likely due extraction rather than caries, as the dentine in the area did not show any signs of trauma.

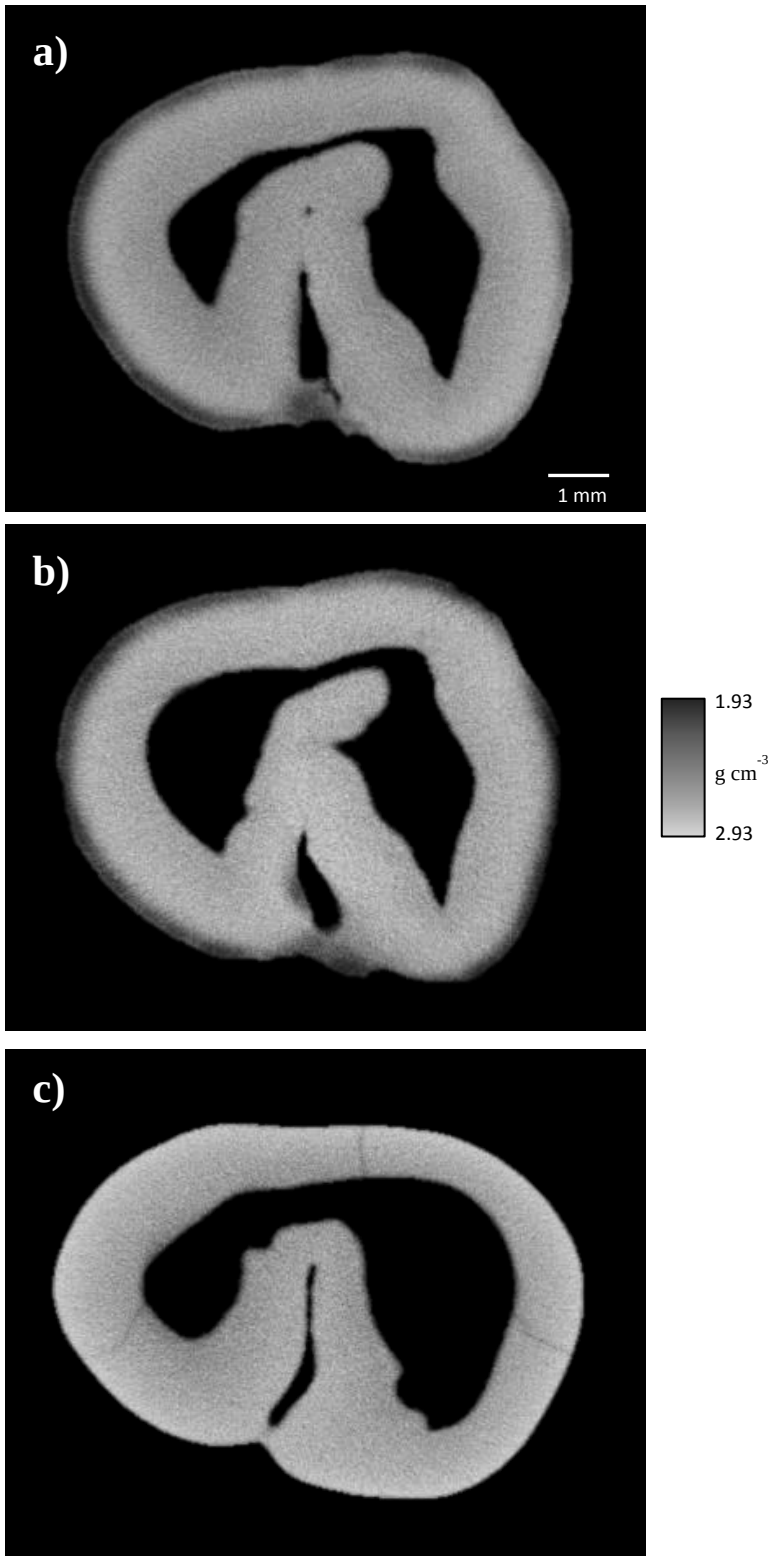

Figure 8.3: High contrast tomographic images taken from the occlusal plane (XY) of a) HYPO1, b) HYPO2 and c) HEALTHY enamel tooth sample, 2.2 mm below the cusp.

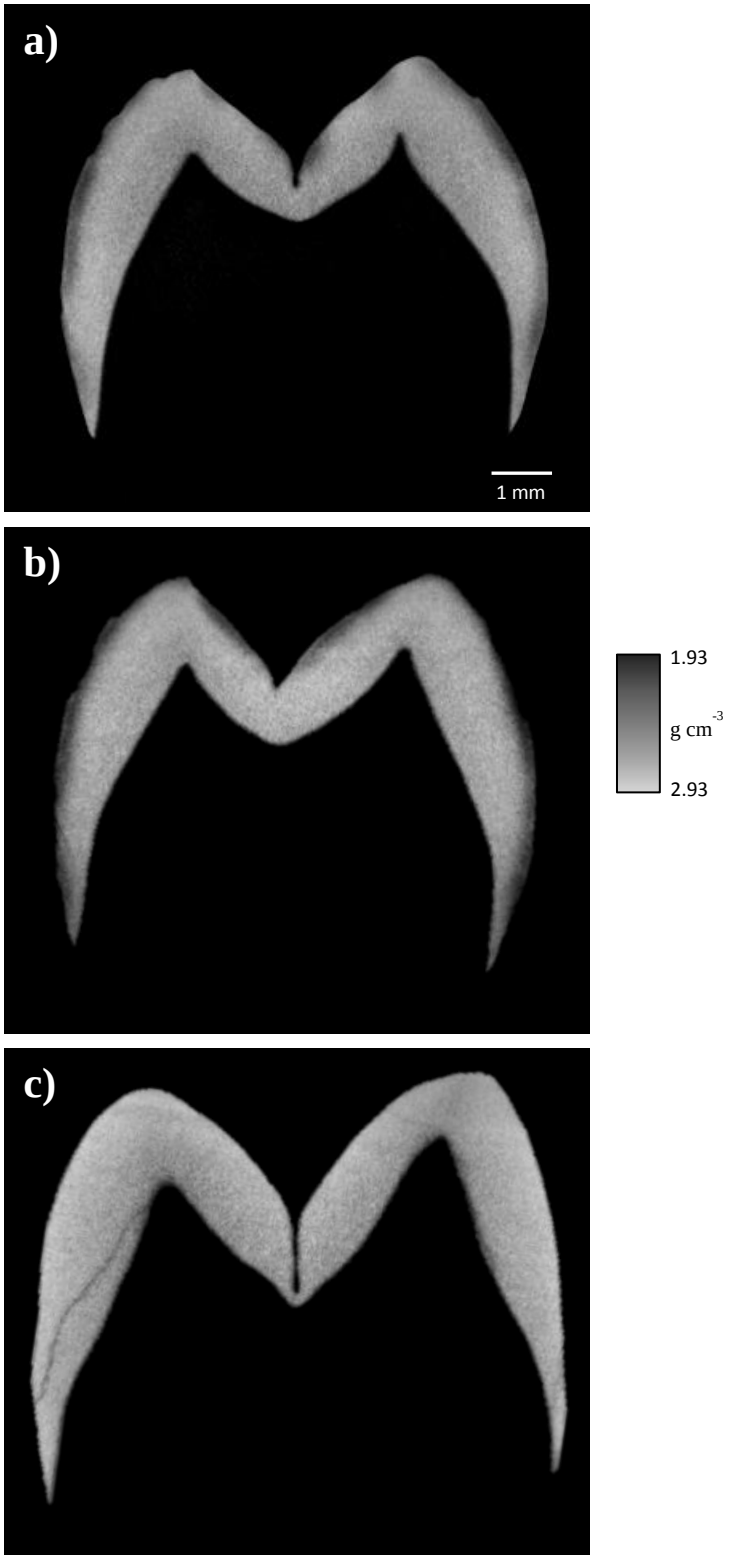

Figure 8.4: High contrast tomographic XMT images taken from the mid region (XZ plane) of a) HYPO1, b) HYPO2 and c) HEALTHY enamel.

A line profile (Fig. 8.5) was taken through the cervical region of HYPO1 (red), HYPO2 (blue) and HEALTHY (black) to accurately quantify and compare the mineral concentration range (Table 8.2) between the three samples. The 2D images show the region where the mineral concentration values were extracted (line colour on the image corresponds to the line profile colour in the graph). The mineral concentration ranged from 1.93 – 2.53 g cm^{-3} in HYPO1, 2.17 – 2.65 g cm^{-3} in HYPO2 and in HEALTHY enamel was 2.93 – 2.35g cm^{-3} from the surface towards dentine. The graph in Fig 8.5d confirms that although HYPO1 and HYPO2 have enamel of normal thickness, both display differences in mineralisation compared with HEALTHY enamel. Although the surface of HYPO1 and HYPO2 was the region most affected, the lowest mineral concentration was observed within 500 µm of the enamel surface, which corresponded to the dark band seen in the 2D hypomature images (Fig. 8.3a and b, Fig 8.4a and b), at the direct surface was an intense peak of high mineral concentration (HYPO1 1.95 g cm^{-3} and HYPO2 2.00 g cm^{-3}) The remaining enamel layer displayed homogenous mineral density with very little variation across the depth of the track. This was a contrasting trend to HEALTHY enamel, as firstly, highest mineral concentration was at the surface (500 µm) of HEALTHY sample, secondly a steadily decreasing gradient was observed on displayed approaching the EDJ. HYPO1 has the overall lowest mineral concentration than the other two samples; however, the bulk enamel of HYPO2 has a slightly greater mineral concentration than HEALTHY enamel (Table 8.2).

Sample	**Mineral concentration (g cm^{-3}) range Surface to EDJ**	**Highest mineral concentration (g cm^{-3})**
HYPO1	1.93 – 2.53	2.63
HYPO2	2.17 – 2.65	2.89
HEALTHY	2.93 – 2.35	2.94

Table 8.2: Mineral concentration values extracted from the line profile (Fig. 8.5).

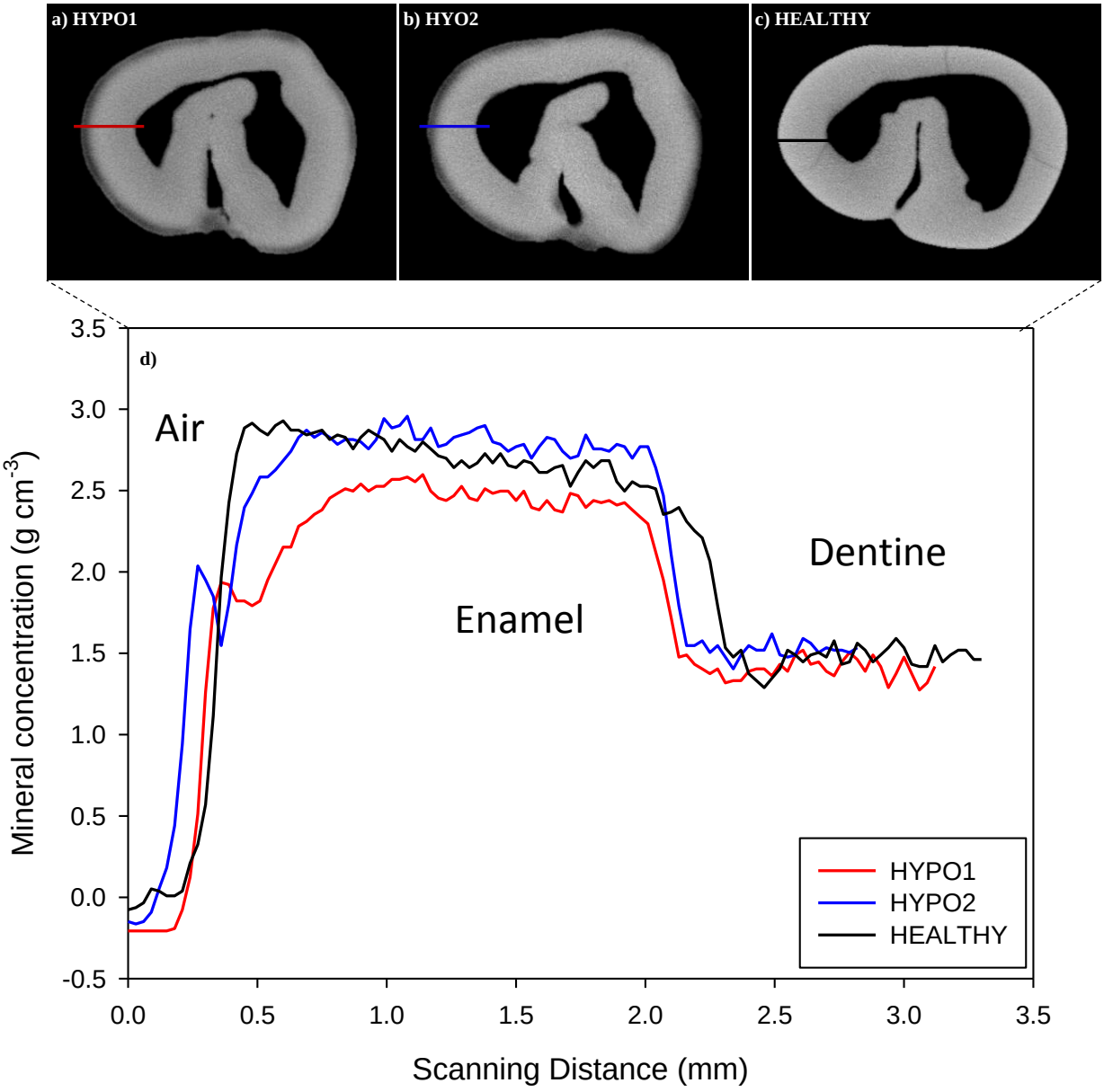

Figure 8.5: a)-c) 2D tomographic images showing where the line profiles were taken; d) Plotted line profiles taken from the cervical edge of HYPO1 (red), HYPO2 (blue) and HEALTHY (black) enamel.

Texture quantification

The spatial distribution of preferred orientation in enamel was extracted from Rietveld refinement and used to construct 2D contour maps to determine the texture pattern in hypomature enamel. This was done using equation 3.7, where C_L^{mn} is C_2^{00}, which corresponds to the 002 reflection. Data collected for the HEALTHY type-matched control could not be analysed due to poor quality. The poor counting statistics (due to low flux) meant that the data for this particular sample could not be refined. Figure 8.6 is an example of a typical diffraction pattern from the HEALTHY sample. Due to the increasing background and indistinguishable peaks seen throughout the data set, no further analysis could be conducted. Therefore, the HYPO1 and HYPO2 texture distribution maps will be compared to a previously published texture map of a lower second premolar (Al-Jawad et al., 2007). Although this is not strictly a type-matched control specimen, it is a premolar and given the issues with the data described above it is the best reasonable control sample to use for comparison. This is an example of instrument limitations. The HEALTHY sample was measured on beamline B16 at the Diamond Light Source. Due to time restrictions, the sample could not be scanned on the XMaS beamline. Although full effort was made to ensure experimental set up of B16 was similar to that of XMaS (energy and beam spot size), variation occur between different facilities. Tube slits were place to define the beam; however this resulted in lower flux and greater exposure. The counting time was increased to compensate but data quality was poor.

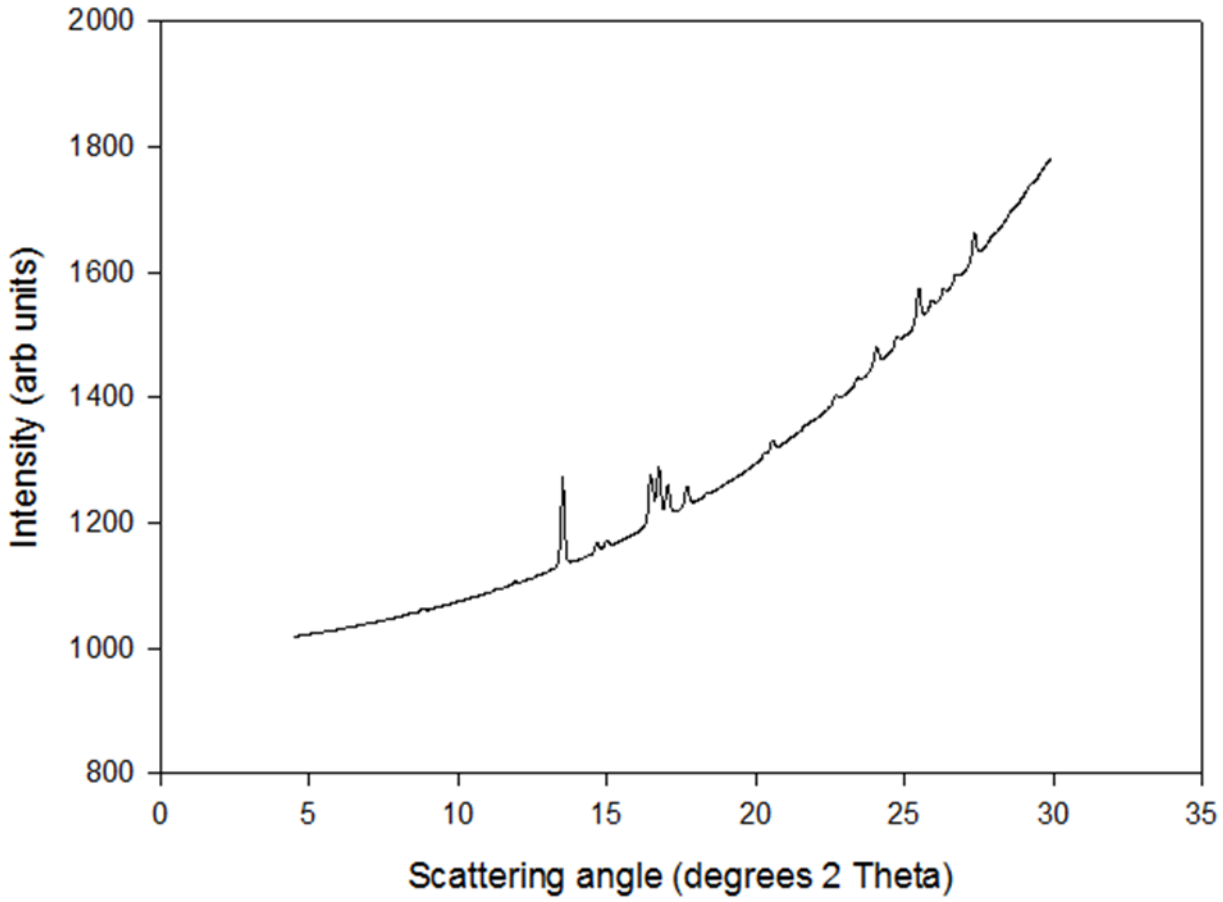

Figure 8.6: Diffraction pattern taken from HEALTHY enamel. This data set could not be analysed due to poor counting statistics.

The texture distribution maps (Fig. 8.7), of the two AI hypomature samples HYPO1 and HYPO2 show similar features, where the lowest texture values were observed in the cuspal region and along the surface the cervical regions and close to the tooth fissure, forming a band like appearance. In both samples, the enamel displays an anisotropic distribution with varying organisation seen as a function of position; crystallites tend to have a higher degree of texture deeper in the enamel, approaching the EDJ. The difference in scale between HYPO1 and HYPO2 highlights that HYPO1 was severely affected. The HYPO2 sample exhibits a small region of high crystallite order below the buccal cusp at the apex of the dentine horn. It should be noted that the texture map of HYPO2 has a small section missing from the top left side. This was due to enamel loss during sample preparation. Enamel samples of that thickness are prone to damage. Referring back to Figure 8.2b, that particular region had was already chipped and damaged. The control sample exhibits a different trend in texture to that of the hypomature AI in that highest texture was observed in the cuspal region, with the degree of texture decreasing towards the EDJ and cervical region.

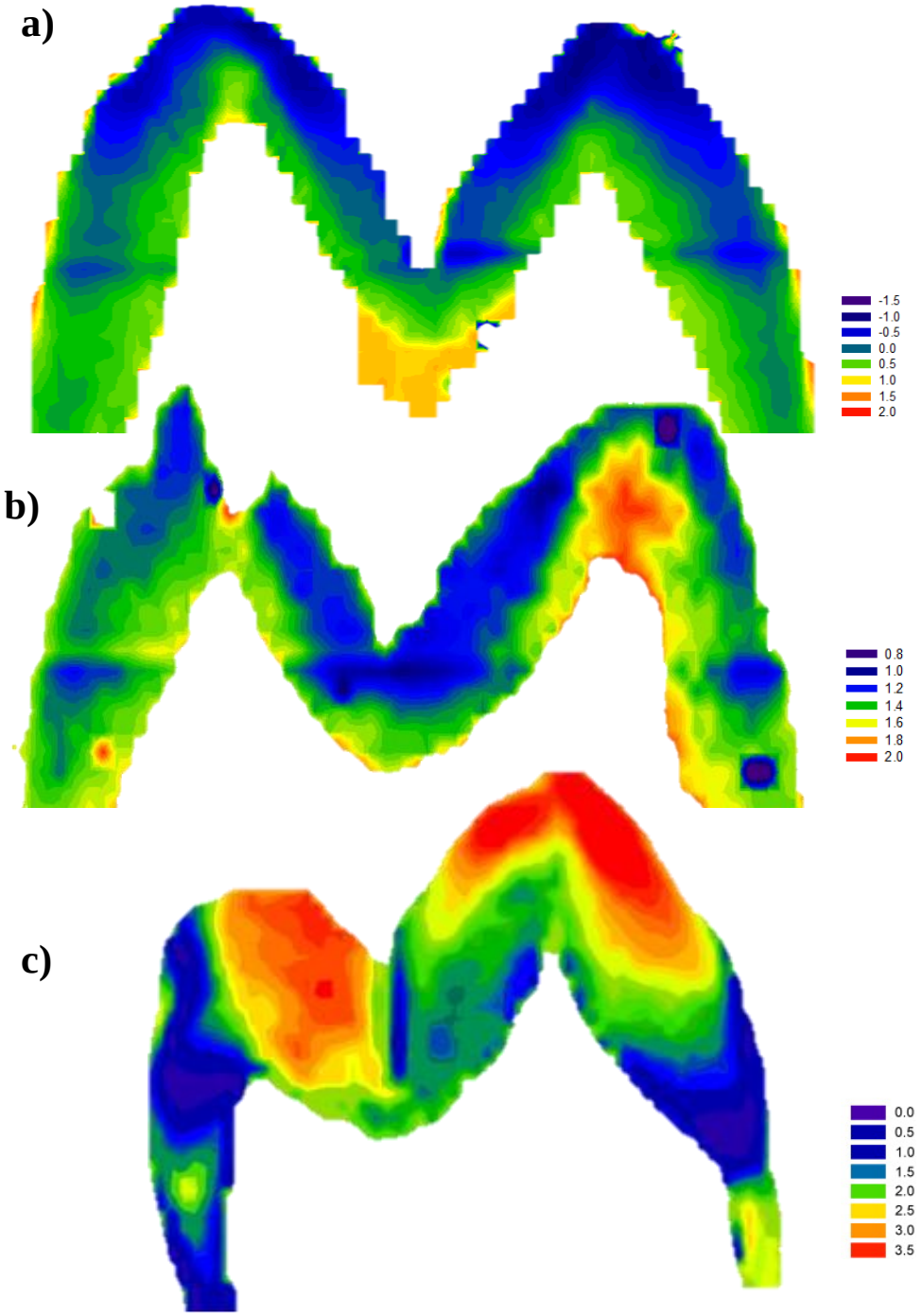

Figure 8.7: Texture distribution contour maps showing the magnitude of preferred orientation in the (002) reflection across the crown from a section of a) HYPO1, b) HYPO2 and c) Healthy enamel (Al-Jawad et al., 2007).

In order to visualise the changes in texture, line profiles (Fig. 8.8) were taken through the depth of the enamel (surface to EDJ) from the buccal and lingual regions of the HYPO2 section. Track 1 (Fig. 8.8a) and Track 3 (Fig. 8.8c) (vertical and horizontal to the lingual dentine horn respectively), show the outermost surface (between 0-150 µm from the outer enamel edge) to have the highest texture compared to the bulk of the enamel. This corresponds to the mineral distribution plot (Fig. 8.5), where highest concentration was present at the direct surface. Both vertical and horizontal tracks on the lingual side showed similar trends. Beyond 150 µm, a dramatic decrease in texture occurred until 500 µm after which the texture values began to increase. The region of low texture between 150 and 500 µm resembled the areas of lower mineral concentration seen in Figure 8.5. Track 2 (Fig. 8.8b) and 4 (Fig. 8.8d), from the buccal side, did not show the high surface texture seen on the lingual side. The enamel displays the lowest degree of texture at the surface with a gradual increase travelling towards the EDJ.

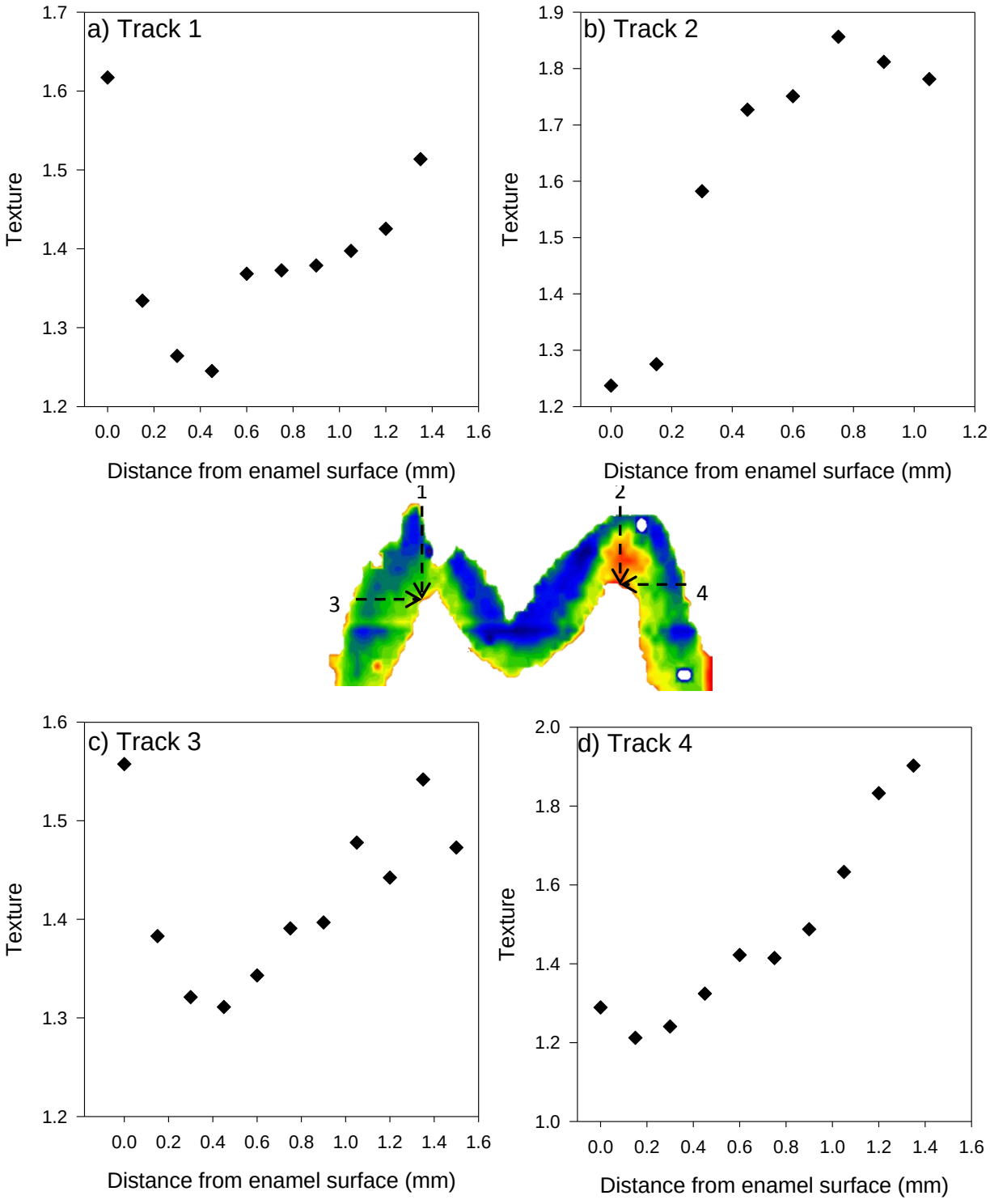

Figure 8.8: Line profiles from HYPO2 enamel section highlighting the texture variation as a function of position along four tracks.

Enamel microstructure

The scanning electron micrographs presented in Figure 8.9 are representative images revealing the microstructural organisation of the apatite crystallites from hypomature enamel (HYPO1 in Fig. 8.9a and c) and healthy enamel (HEALTHY Fig 8.9b and d) taken from the cuspal and cervical region. Hypomature enamel displays a difference in both individual crystallite shape and size and in the organisation of crystallites in different regions of the crown. In HYPO1, at the cuspal region, close to the enamel surface which correspond to the area of lower mineral concentration and a lack of preferred orientation, crystallites appear to be short, thick, tablet-like in shape and disordered with respect to each other. However in the bulk of the enamel of HYPO1, crystallites were long thin and needle like, organised and bundled into prismatic structures and resembled much more closely the ultrastructure of healthy enamel. An interesting feature was noticed continuously in the hypomature enamel, whereby a partition between the two distinctive morphologies existed (indicated in Fig. 8.9c by a red dashed line).

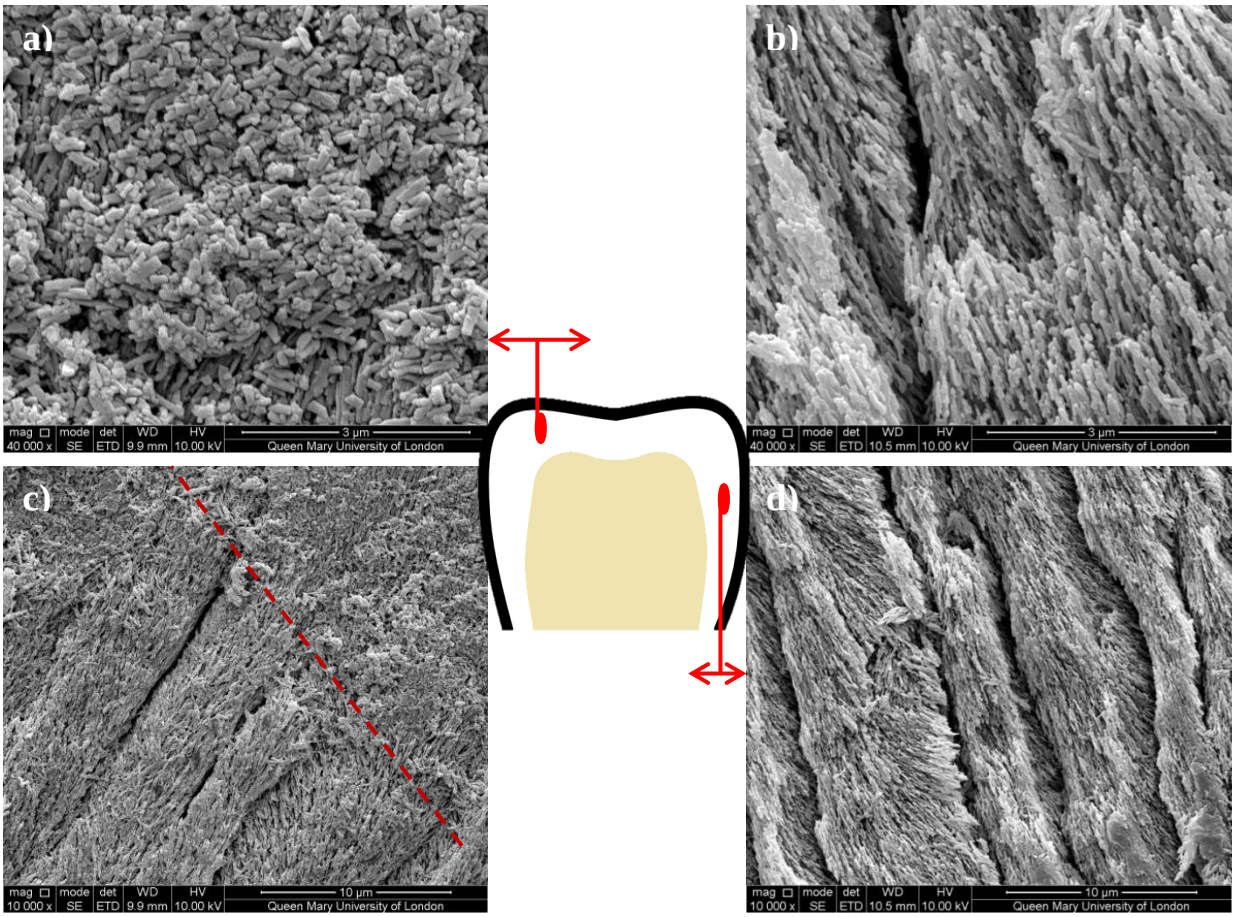

Figure 8.9: SEM images comparing the microstructure of hypomature enamel with healthy enamel, from the tooth cusp of the a) AI affected and b) healthy enamel and from the bulk of the cervical region from c) AI affected and d) healthy enamel.

8.4 Discussion

The maturation stage of amelogenesis is a critical step in the formation of a strong and mineralised, fully functional tissue. It is essentially marked by the morphological transition of ameloblasts, causing the secretion of enamel proteins to be terminated and initiates the secretion of the KLK4 protease for degradation (along with MMP20 protease present from late secretory stage) of the organic matrix. This allows growth of the HA enamel

crystallites in thickness and width as well as hardening of the enamel layer from the influx of mineral ions.

The hypomaturation subtype of AI is likely to arise as a result of a disturbance in the maturation stage of enamel formation due to a mutation in the gene encoding the proteases, which alters its catalytic ability in the breakdown of the matrix, ultimately reducing mineralisation and modifying preferred orientation.

The results presented in this chapter clearly show that the hypomature subtype has the greatest effect on the surface of the enamel layer, within 500 µm. This region displayed the lowest mineral concentrations (Fig. 8.5) and crystallite texture (Fig. 8.7). The ring of lower mineral concentration observed only around the surface of the hypomature tooth suggest that defects of hypomaturation possibly make the enamel surface more porous and unable to undergo any post eruptive surface maturation. HYPO1 showed greatest severity in damage at the surface in comparison to HYPO2. Although it is difficult to know which aspect of this is a feature of the maturation process directly, and which is post-eruption wear, as a consequence of the compromised structure of the enamel, it can be assumed that it is a feature of the maturation process as the control sample remained intact.

Generally, healthy enamel displays the highest degree of crystallite alignment at the surface rather than close to the EDJ (Low 2004). However, in this case the opposite trend was seen, where the degree of crystallite alignment increased travelling through the bulk of the hypomature enamel. Al-Jawad *et al* (2007) showed that the entire buccal cusp and inner side of the lingual cusp of a permanent premolar to be the regions with greatest crystallite alignment, as these exposed areas bear the greatest loads during mastication. The enamel surface of the hypomature sections, including the cusps, was the region which had the least crystallite order, indicating that hypomaturation can result in a loss of function and a brittle surface (Fig. 8.2). Simmons *et al* (2013) observed the progression in enamel maturation by measuring the mineral concentration and texture distribution from three different stages of maturation. At every stage of development, the cusps of the molars were the regions with higher crystallite alignment in comparison the rest of the tooth section. This suggests that disruption caused during the maturation stage does not simply cause incompletion of the

process, but in fact alters the microstructural organisation. Texture distribution of the AI hypomature was low throughout the whole crown, suggesting that the maturation not only dictates the mineral concentration but also has an effect on the organisation. Evidence of prismatic structure in the AI enamel (Fig. 8.9c) indicates the presence of some order. The complete and overall lack of crystallite alignment suggests that disruption occurred as ameloblast secrete the protease and travel from EDJ to surface. The texture data presented in this study suggests that the hypomaturation subtype does not necessarily mean that the defect during enamel formation is strictly isolated to the maturation stage. Disruption during the secretory stage is also possible due to the lack of crystal organisation. The texture tracks taken along HYPO2 show that the buccal and lingual sides were different. This trend was previously seen in healthy enamel using SXRD (Al-Jawad et al., 2008) and in the mechanical properties, through nanoindentataion measurements (Cuy et al., 2002).

8.5 Conclusion

Specialised X-ray techniques were used to characterise the structural features of enamel, clinically diagnosed with the hypomature subtype of AI. Hypomature enamel had uniform mineral layer in the bulk enamel, lacking any gradient. There was an overall lack in crystallite alignment across the tooth section. The most severely affected region was at the enamel surface.

Chapter 9: Recovery of Crystallographic Texture in Remineralised Dental Enamel

9.1 Introduction

Dental caries is the most prevalent disease encountered by people of all ages around the world. Little is known about the crystallographic effects of demineralisation and remineralisation. The motivation for this study was to develop understanding of the caries process at the crystallographic level in order to contribute towards a long term solution. Combining microstructural and crystallographic characterization aids the understanding of caries and erosion processes and assists in the progress towards developing therapeutic treatments to allow affected enamel to regain structural integrity.

To date, little attention has been given to recovering lost preferred orientation of the apatite crystallites, which is crucial for restoring normal and lasting function of the enamel tissue. This chapter presents the application of novel X-ray techniques to understand the crystallographic features of de- and remineralised enamel by comparison with healthy enamel, thus exploring the demineralisation pathway, the mechanism of remineralisation and characteristics of the remineralised hard tissue.

9.2 Experimental setup

Sample collection and preparation

Whole tooth specimens were collected with written consent from patients undergoing routine orthodontic extraction at Barts and The London Dental Hospital (approved by the Queen Mary University of London Research Ethics Committee, UK). The extracted teeth were stored in 70% ethanol, and then washed with distilled water before use.

Four type-matched permanent human mandibular first molar tooth samples were included in this study (Fig. 9.1); a) enamel with artificially demineralised lesion; b) artificially demineralised then remineralised enamel; c) naturally carious enamel (identified by the

presence of a white spot lesion); and d) healthy enamel region. For consistency and direct comparability, the same tooth type was used, and a region of interest within each tooth was chosen to be spatially equivalent (see boxes in Fig 9.1). The healthy region was selected by ensuring it was not in close proximity to any lesions.

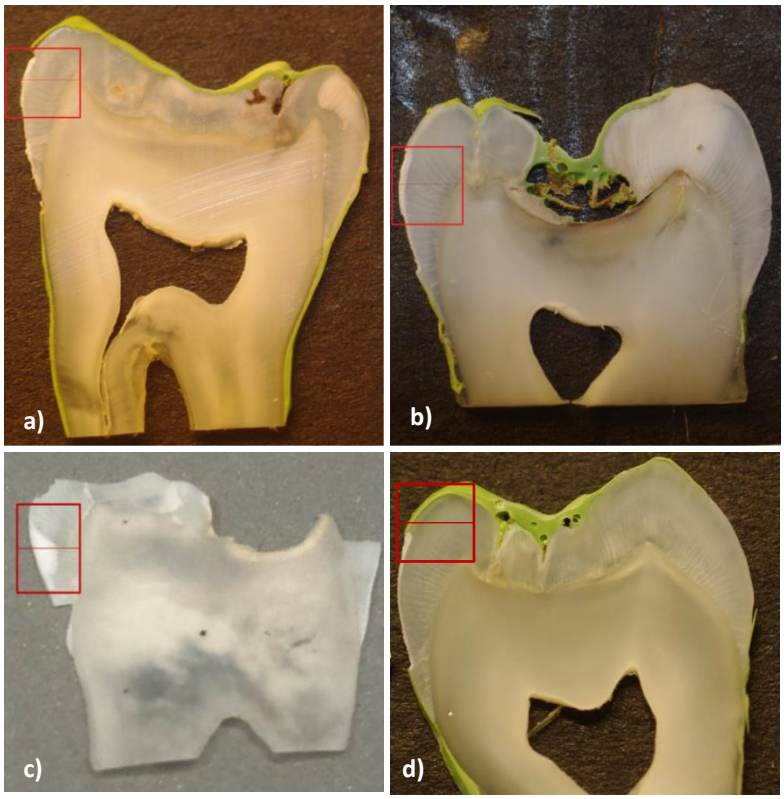

Figure 9.1: Digital photographs of enamel samples a) artificially demineralised, b) artificially remineralised and c) naturally carious and d) healthy enamel, outlining regions of interest (box) selected for SMR measurement. The line within the box represents the track measured using SXRD.

The details of each specimen treatment including the demineralising and the remineralising solutions are given in Table 9.1. Artificial lesions were created by coating a whole healthy tooth crown in acid resistant varnish leaving a 2 mm x 2 mm window of enamel exposed. The whole tooth samples were then sectioned into 500 µm thick longitudinal slices perpendicular to the exposed area using a wet precision annular saw.

Sample	Treatment	Ingredients	Time
Artificially Demineralised	Demineralisation	Exposed to 100ml of 1% acetic acid, buffered to pH4 using NaOH at room temperature	7 days
Artificially Remineralised	Demineralisation then Remineralised	Exposed to 100ml of demineralising solution immersed in 100ml remineralising solution (2mmol/l $CaCl_2$, 1.2mmol/l KH_2PO_4, 150mmol/l NaCl, 0.05mmol/l NaF)	7 days 7 days
Natural caries	No treatment		
Healthy	No treatment		

Table 9.1: Treatment regimen for tooth samples

Experimental method

2D X-ray diffraction patterns were collected on the BM28 (XMaS) beamline at the ESRF (described in chapter 6 section 6.1.1). An X-ray wavelength of 0.82 Å (equivalent to energy 15.1 keV) was used with a sample to detector distance of 180 mm allowing a 2θ range of 5-25°. A microfocussed 20 µm x 20 µm beam spot was directed on to the mounted sample. Enamel slices were mounted by the root of the tooth section onto a travelling platform to be scanned in two orthogonal directions. Regions of interest (Fig. 9.1) were selected visually according to where the artificial lesion was made. A Topcon telescope (AT-G2, Japan) was used to identify precise regions located using the telescope's cross hair which was aligned with the plane of the X-ray beam.

Each diffraction pattern took 20 s to collect (including 8 s CCD camera processing), and a total of 4839 diffraction patterns were collected.

2D diffraction patterns of dentine and enamel can be distinguished by the Debye ring characteristics. Patterns representative of dentine display uniformity in intensity azimuthally indicating lack of preferred orientation, and broadening of the Bragg peak due to small crystallites. However, enamel diffraction patterns display variations in the intensity azimuthally especially around the 002 Bragg reflection which is indicative of the presence of preferred orientation (Al-Jawad et al., 2007, Thewlis, 1940, Hirota, 1982).

Each diffraction pattern was azimuthally integrated over 360^0 in a narrow 2θ band containing the 002 reflection. Intensity versus the azimuthal angle was plotted and fitted to a Gaussian peak-shape. Changes in the full width half maximum (FWHM) in each azimuthal plot were monitored along a track (Fig. 9.1) from the enamel surface to the EDJ. Variations in the 2θ position of Bragg reflections provide information on changes in crystal chemistry as a result of different treatments (Al-Jawad et al., 2007). The (002) Bragg reflection located at $2\theta_{002} = 13.676°$ was used to measure changes in the peak position.

Mineral Concentration

The scanning microradiography (SMR) system has been developed over a number of years at Queen Mary University of London for direct and accurate mineral concentration measurements (Anderson et al., 1998, Anderson et al., 2004, Elliott et al., 2005, Gao et al., 1993). The X-ray source is a microfocussed X-ray generator (Ag target 40 kV, 1.0 mA tube current) with a small aperture to create an X-ray beam of ~15 μm diameter (Gao et al., 1993). SMR cells containing the tooth slice were constructed from a polymethyl methacrylate sheet and then mounted on the X-Y translational stage. The number of photons in pre-set times at each scan position and outside the tooth slice were counted using a high purity geranium detector with a pulse height analyser (EG & G, Oak Ridge, TN, USA) set to pass AgKα radiation. High resolution area scans (stepsize 20 μm) were carried out on all slices. The projected mass of enamel at each position was calculated from the transmitted X-ray intensity, and published values of the mass attenuation coefficient of hydroxyapatite as previously described (Anderson et al., 1998). Although the absolute

values of mineral concentration at each point were difficult to determine as this is dependent on specimen thickness, the tooth slices were planoparallel and therefore relative differences in mineral concentration arising from acidic attack at a particular point could be compared with unaffected points in the same slice.

Microstructure

The microstructure of the same regions of interest were characterised using SEM. Each tooth slice was etched using 35% orthophosphoric acid for 15 s, (a common procedure used in dental clinics to remove surface contaminants and the smear layer (Banerjee and Watson, 2011), washed with distilled water then mounted on an aluminium stub and sputter-coated with gold.

9.3 Results

002 Preferred Orientation

The (002) Bragg plane is orthogonal to the c-axis of the hexagonal crystallite structure in hydroxyapatite. Since this is the long axis of the needle-like enamel crystallites, evidence of preferred orientation is most strongly seen as variations in the intensity around the Debye-ring of this reflection (Hirota, 1982).

Figure 9.2 shows the changes in the crystallographic texture (FWHM) of the 002 reflection (from the track shown in Figure 9.1) within 400 μm from the natural surface, as a function of position for all four tooth samples. Healthy enamel shows a gradual decrease in FWHM from the surface to deeper within the enamel. The first 80 μm from the surface of the artificially demineralised enamel exhibits significantly higher FWHM values, followed by a steep decrease moving further away from the surface until a depth of 275 μm, after which there is a slight rise. The first 20 μm of the natural caries enamel has similar FWHM values to that of healthy enamel with the highest values seen between 80-100 μm. In the artificially demineralised and subsequently remineralised specimen, the surface enamel has FWHM values similar to that of healthy enamel, and continues to follow the same trend as healthy enamel for most of the track, deviating slightly towards the EDJ.

FWHM data is plotted up to 400 µm from the surface, as this is the region which was affected. Furthermore, the depth of enamel varied according to the region that was studied. It must also be noted that the remineralised enamel was initially artificially demineralised which is a possible explanation for the increase in FWHM deeper into the enamel.

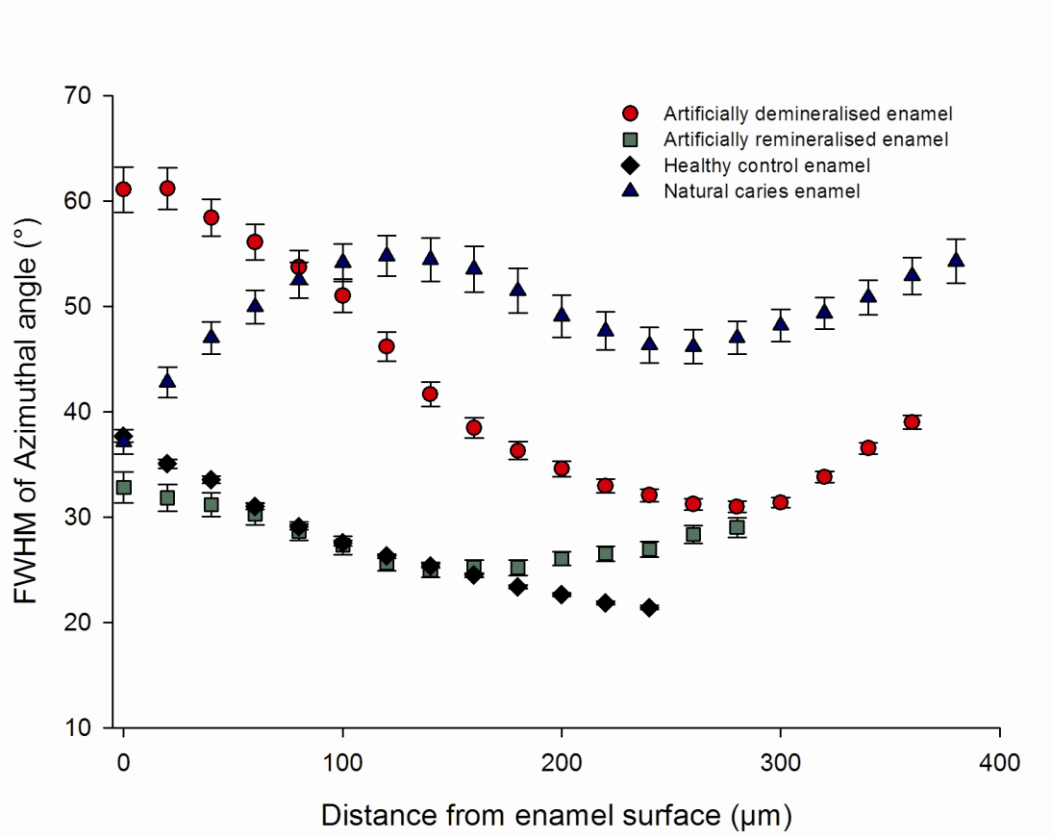

Figure 9.2: Changes in the FWHM. A track (highlighted in Fig. 9. 1) taken through each tooth slice (artificial demineralisation, artificial remineralisation, healthy control and natural caries) from enamel surface to EDJ measuring the change in FWHM of the azimuthal peaks of the 002 reflection. Error bars represent the uncertainty in fit of the 002 peak to the Gaussian function.

002 Bragg Peak position

Figure 9.3 shows the percentage change in the 002 Bragg peak position as a function of distance from the natural tooth surface. There is very little change in peak position within each sample. A slight increase in the 2θ value is seen in the natural caries enamel from a 280 µm depth (<0.5 %) onwards.

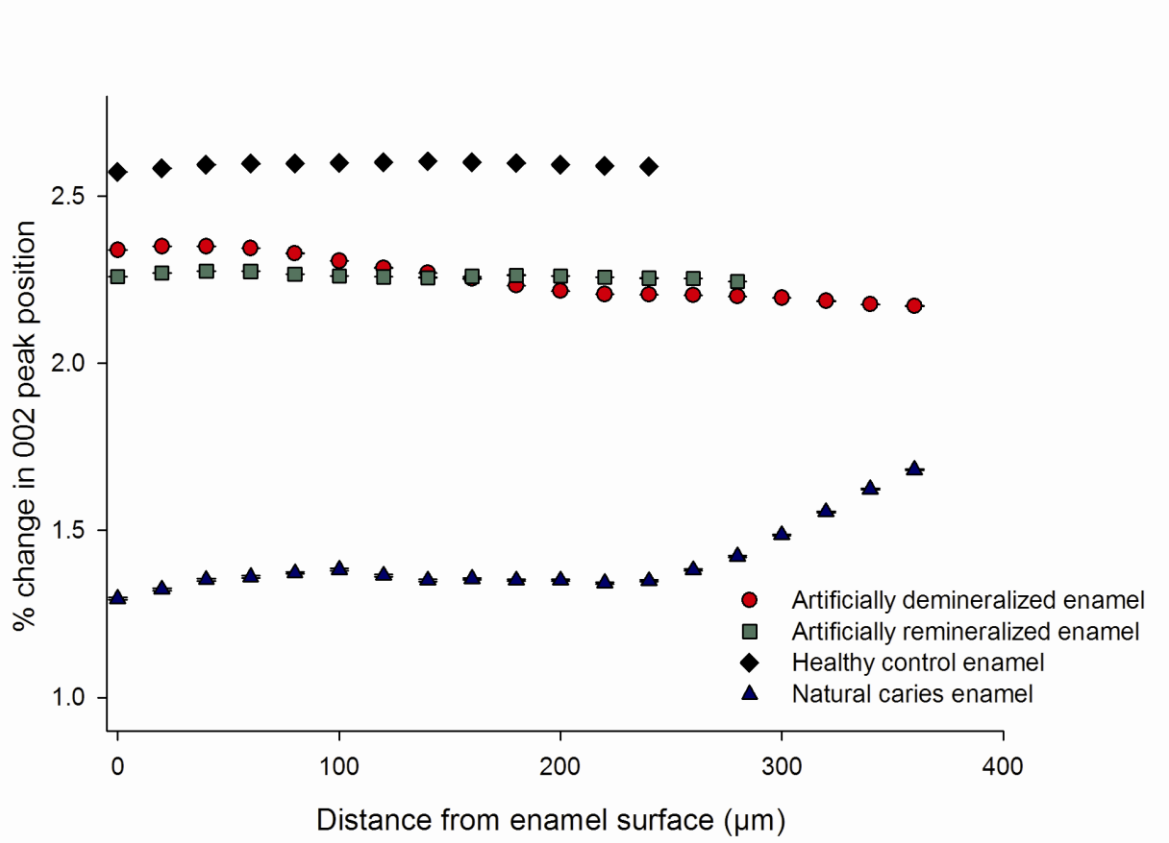

Figure 9.3: Changes in 002 Bragg peak position in a track (highlighted in Fig. 9. 1) through each tooth slice (artificial demineralisation, artificial remineralisation, healthy control and natural caries) from enamel surface to EDJ. Error bars represent the uncertainty in fit of the 002 peak to the Gaussian function.

Mineral Concentration

Figure 9.4 shows the SMR area maps of the percentage mineral concentration for each slice. The maximum value for each enamel slice was defined as 100 % mineral concentration in the unaffected region away from the lesion. The artificially demineralised enamel regions (Fig. 9.4a) can be differentiated from the healthy regions. For example Figure 9.4c, shows a 10-30 % lower mineral mass in the body of the lesion. Figure 9.4b shows the artificially remineralised enamel and the uniformity of the mineral concentration across the tooth is such that the treated area is indistinguishable from the unaffected areas. The naturally carious (Fig. 9.4c) enamel shows a thin, low mineralised barrier isolating the subsurface lesion with an average 30 % mineral mass reduction. Mineral density of the

surrounding enamel is higher and uniformly distributed. The control, healthy enamel (Fig. 9.4d) shows uniform high mineral concentration. It should be noted that the thickness of the slices (500 μm) results in partial volume edge effects at the periphery, but this does not interfere with the measurement of the bulk enamel.

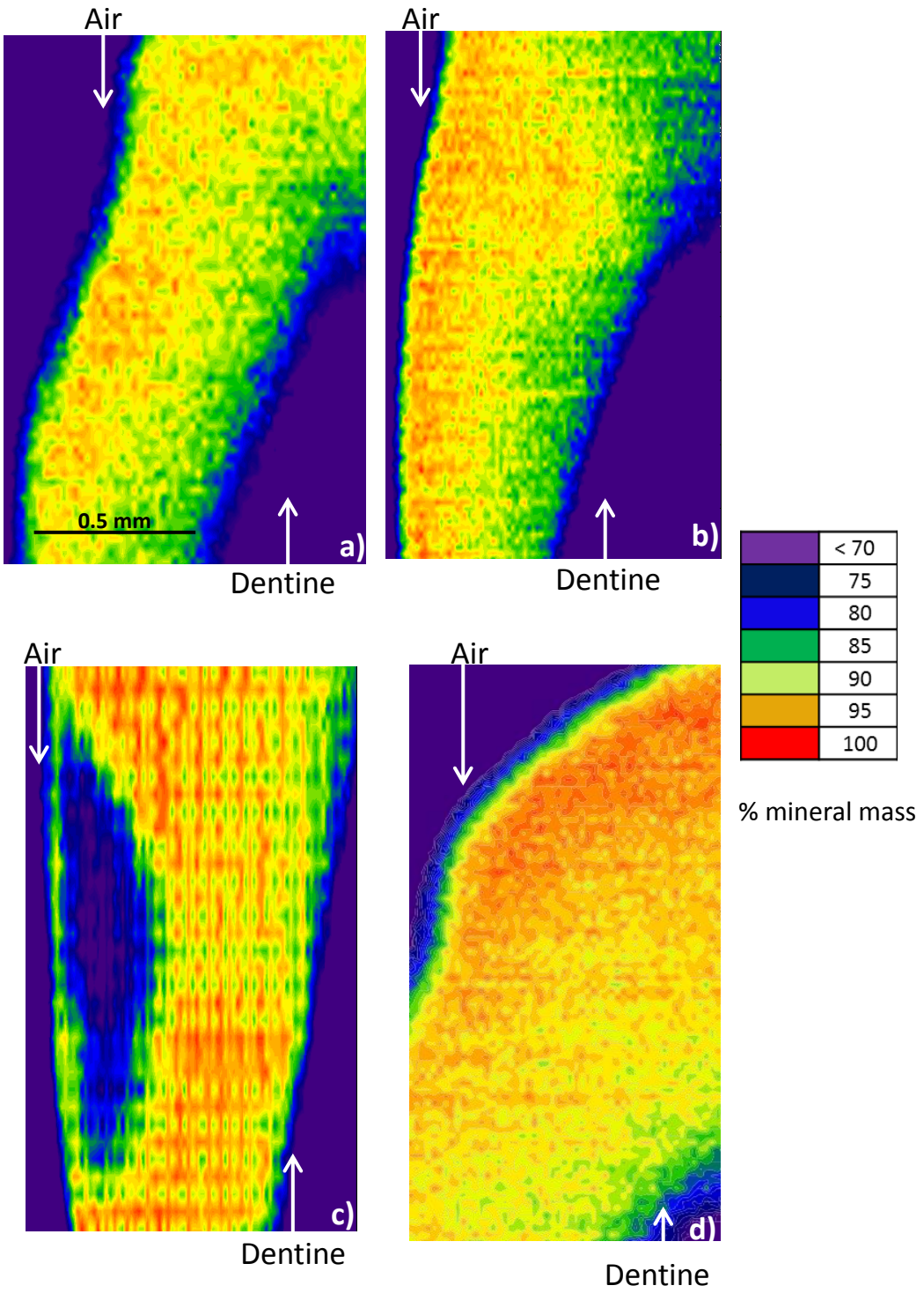

Figure 9.5: Scanning microradiography area scans showing the relative mineral density distribution of a) artificially demineralised lesion, b) artificially remineralised enamel, c) natural caries lesion, d) healthy enamel. The scale bar and colour intensity bar is representative for all images.

Microstructure

Figure 9.5 show representative SEM images close to the natural surface of the named regions in each specimen. The prisms in artificially demineralised enamel (Fig. 9.5a) appear etched where prism cores have been significantly more affected than the walls of the prisms and the interprismatic enamel which remain more intact. The image for the remineralised enamel (Fig. 9.5b) shows thin plate-like deposits arranged in clusters (lacking directional growth), forming a layer over the entire surface of the enamel specimen, with some small crystallites visible underneath. The crystallite morphology of the outer surface of the naturally carious enamel (Fig. 9.5c) resembles healthy enamel (long, thin, ordered crystals). However, moving in towards the bulk of the enamel towards the body of the lesion (inset), there is a loss of microstructural organisation and crystallites have fused together giving an amorphous appearance, with no distinct boundaries. Healthy enamel (Fig. 9.5d) shows long thin, needle like, bundles of crystals with preferred orientation evident.

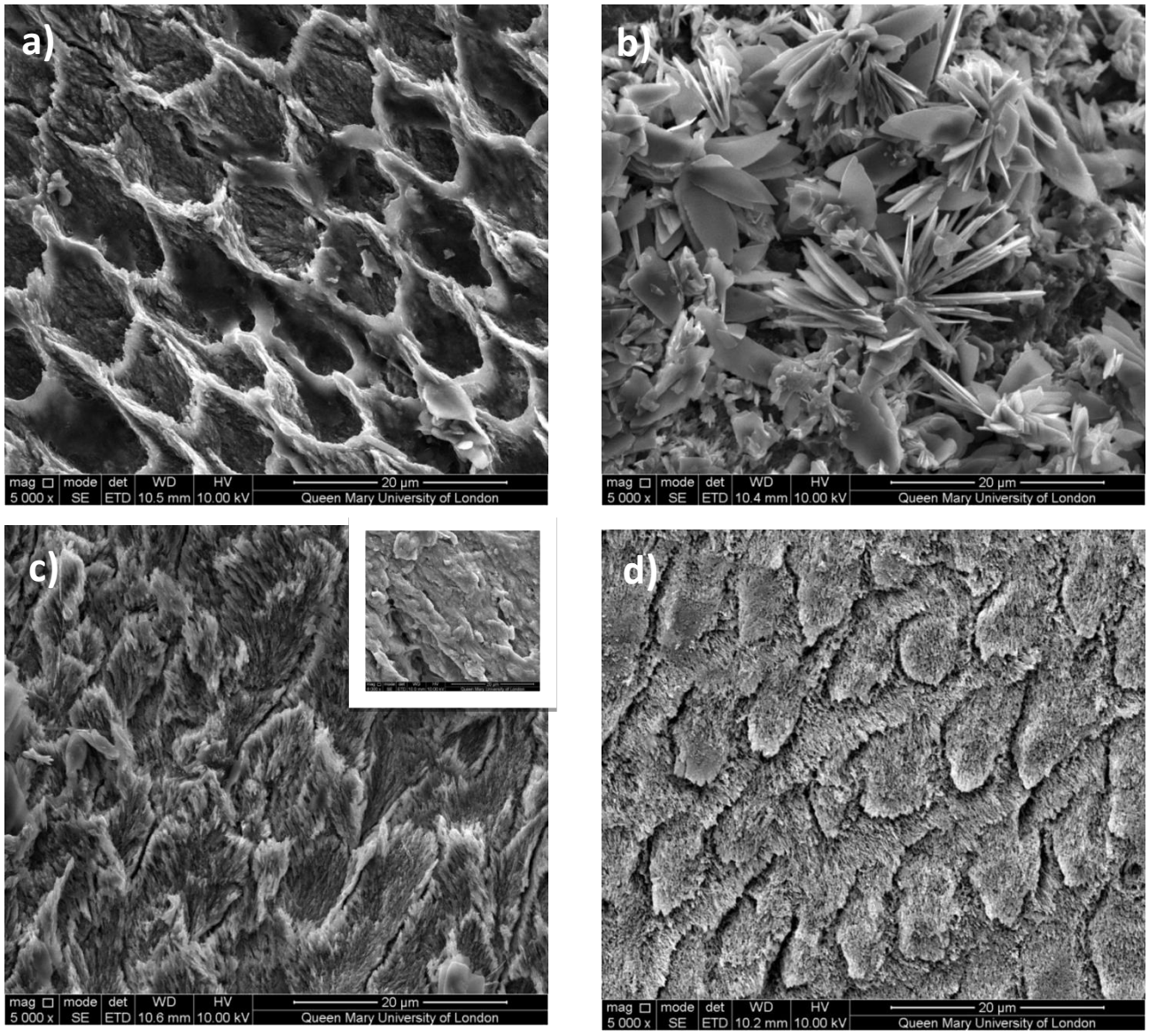

Figure 9.6: SEM images of enamel from the surface of a) artificially demineralised b) artificially remineralised c) naturally carious (surface) and d) healthy region. The inset in c) shows the bulk of the carious region ~150 µm from the surface.

9.4 Discussion

The azimuthal variation in intensity of the scattering signal around the 002 reflection (Fig. 9.2) was related to the arrangement of enamel crystallites in the prisms running from the EDJ to the surface (Al-Jawad et al., 2007).

This study demonstrates that a loss of crystallographic texture occurs as a function of demineralisation in the natural caries and artificially induced lesions. However this loss was seen at different spatial regions between the two specimens, indicating a difference in the mechanism of crystallite dissolution. The surface of the artificially demineralised enamel suffered the greatest mineral loss and also the highest degree of loss in preferred orientation, which was seen within the first 100 μm from the surface (Fig. 9.2, filled circles). The crystallographic trend seen in the natural caries enamel (Fig. 9.2, filled triangles) correlated with the corresponding SMR data (Fig. 9.4) and resembles that observed by polarized light microscopy in previous studies of caries progression (Hicks and Silverstone, 1984, Darling, 1961) where the outermost enamel can remineralise within the oral environment. The natural carious enamel showed crystallite order at the surface where the highest degree of loss in crystallite order occurs between 80-180 μm deep into the bulk of enamel. The surface layer is a characteristic feature of natural carious lesions, with an intact surface, an increase in texture suggests that crystallite order was regenerated naturally in the oral environment. Figure 9.2 (filled diamond) reveals that texture was regained as a result of remineralisation. The similarity in FWHM values and the depth-profiles between remineralised enamel and the healthy control enamel suggests that remineralisation promotes re-formation of crystals in an ordered manner to restore their original orientation. Dissolution roughens the enamel producing kinks, steps and defects on the apatite crystallite surface which can serve as nucleation sites. The Ca^{2+} and PO_4^{3-} ions react with these sites allowing the crystallite to grow on existing crystallite remnants rather than the *de novo* formation of new crystallites (Featherstone, 2008, Tohda et al., 1990, Yanagisawa and Miake, 2003). Growth of partially dissolved crystallites can occur by the surface condensation of free molecules in a supersaturated solution onto larger particles (Czajka-Jakubowska et al., 2009). This SXRD study confirms that calcium and phosphate do not simply precipitate on the surface but in fact integrate into the apatite crystallite

structure giving it preferred orientation. Voegel (1977) and Tohda et al (1987) identified the initiation of dissolution at the core of each individual crystallite, which progressed rapidly along the (002) plane and later developed laterally (Voegel and Frank, 1977, Tohda et al., 1987). This suggests that in early carious lesions the *a* and *b* axes of each crystallite retain some structural framework, allowing the core of the crystallites to be rebuilt during remineralisation. Results from a recent SAXS study have provided some of the first evidence to show a framework scaffold is preserved at a nano length scale to allow structure and direction for the reconstruction of the destructed crystallites during dissolution (Deyhle et al., 2014). The results presented here concur with these findings, quantifying the precise order restored.

Little change was observed in the 002 Bragg peak position in the healthy, artificially demineralised, and artificially remineralised regions (Fig. 9.3). However in the carious enamel a slight change in peak position was observed which can be attributed to the cyclical nature of demineralisation and remineralisation. The dynamics of pH and chemistry in the oral environment may alter the crystal chemistry over time with inclusion and substitution of other ions from the oral environment into the enamel lattice structure, which may also affect the texture.

The SMR contour maps (Fig. 9.4) show a loss in percentage mineral mass in both artificially demineralised enamel (Fig. 9.4a) and natural carious lesions (Fig. 9.4c). The greatest mineral loss in the natural caries samples was seen at the subsurface, isolated between healthy enamel and a mineralised surface layer. The same tend was seen in the microstructure (Fig. 9.5c), where loss of structure was observed in the body of the lesion. Features of the natural caries lesion seen were most probably a consequence of successive periods of cyclic de- and remineralisation over differing time periods when the oral environment favours one or the other process (Applebaum, 1932, Arends and Christoffersen, 1986). Important interactions of the outermost enamel with Ca^{2+} and PO_4^{3-} ions present in saliva and exposure to fluoride in toothpaste promote surface remineralisation (Featherstone, 2008), whilst mineral can be lost throughout the bulk of the enamel. A fully mineralised surface inhibits access of the ions in to the body of the lesion, preventing remineralisation of deeper parts of the lesion, thus forming a subsurface carious

lesion (Deyhle et al., 2014). The mineral loss in the artificial lesion (induced by a demineralising solution for 7 days) displays a different trend to that of the natural caries lesion. A slight decrease in mineral mass (~10 %) is observed at the surface, which is the direct site of attack. This is due to the extreme condition of continuous exposure to the demineralising solution, causing mineral loss from prism cores (Fig. 9.5a). Mineral concentration in the artificially remineralised enamel (Fig. 9.4b) is regained throughout the bulk of the enamel to match that of the healthy region of the specimen.

The microstructural effects of dissolution vary between natural caries and artificially demineralised enamel (Cochrane et al., 2012). The morphology of both inter- and intra-prismatic enamel is different in natural caries and artificially demineralised enamel. This study shows a loss of texture from the artificially demineralised enamel as seen in the diffraction data (Fig. 9.2). This can be explained by the SEM images shown in Figure 9.5b, the demineralised enamel looks very similar to a straight-forward etched enamel surface. The SEM images show that in artificial demineralisation, dissolution occurs predominantly in the prism cores which contain the more highly ordered crystallites. Since the ordered crystallites are preferentially lost, the remaining structure from the prism boundaries will have a lower texture on average. The natural carious tissue lost order in different parts of the prismatic structure, due to the cyclical process of alternating demineralisation and remineralisation events according to the changing oral conditions. Figure 9.5c shows that the microstructure of natural carious enamel following dissolution results in a general loss of prismatic structure in a region ~150 μm from the surface of the tooth. Lower crystallite packing allows easier diffusion of acids and protons into the tissue and mineral ions out (Robinson et al., 2000). The absence of distinct boundaries suggests dissolution has resulted in loss of structure and fusion of crystallites, diminishing preferred orientation.

Although crystallographically similar, the microstructure of remineralised enamel shown in the SEM images (Fig. 9.5b) appears to differ from healthy enamel. The large plate-like crystallites deposits seem to have formed a layer over the enamel crystallites. SEM images probe only the surface topography, potentially masking the more subtle regrowth of crystallites underneath the surface. This limitation is overcome by using SXRD, which allows the measurement of crystallite arrangements as a function of depth within the

sample. Thus, early studies using SEM alone would not have been able to demonstrate that artificial demineralisation differs from natural caries, nor understand the crystallite order following remineralisation.

The general trend seen in the SMR mineral density maps (Fig. 9.4) correspond to the texture distribution observed in Figure 9.2; regions exhibiting lower mineral mass, such as the body of the natural caries lesion and surface of the artificially demineralised, are the regions which lose crystallite order, whereas regions without reduction of mineral mass show higher crystallite order. The artificially remineralised region shows the same mineral mass as that of the control region and higher crystallite order.

9.5 Conclusion

Enamel is susceptible to changes during the caries process which alter the mineral content and crystallographic organisation and microstructure. Characterising and understanding the crystallographic properties of carious enamel is important when developing restorative materials or preventative therapeutics. In this study, the mineral density and crystallographic preferred orientation of enamel have been quantitatively evaluated after demineralisation and remineralisation using specialized X-ray techniques. This study demonstrates that enamel which has lost mineral density and crystallographic texture via apatite dissolution can be restored to its original healthy state by a careful remineralisation regime.

Chapter 10: Restoration of Demineralised Enamel by Synthesis of Ordered Apatite Crystals

10.1 Introduction

The objective of the study presented in this chapter was to synthesise highly ordered apatite crystals mimicking the human enamel structure directly on to the surface of well-characterised demineralised human enamel sections as a method of remineralisation. This chapter describes a two part study; the first was a pilot study, designed to trial three established physicochemical crystal growth methods in order to select one which provides optimum growth of apatite. This was assessed from microstructural characterisation using SEM. The second part was a quantitative measurement using SXRD of the degree of preferred orientation of the resulting synthetic crystals grown via the selected optimum method.

Crystallisation and the subsequent crystals can be influenced by a number of variables, such as temperature, pH, chemical reagents, and substrate surface and incubation time. Yamagishi et al (2005) reported a paste containing synthetic fluoridated apatite (FA) crystals could be used for the repair of caries lesion, which promoted further exploration into methods for acellular regeneration of enamel like layer that can repair and prevent caries. Previous studies have investigated and optimised synthetic growth conditions and mechanisms for synthetic enamel like apatite crystals through precipitation (Chen et al., 2006) and direct growth on metal substrates (Czajka-Jakubowska et al., 2009). Ordered FA crystals have successfully been grown on different substrates under mild hydrothermal conditions, exhibiting variations in growth pattern and morphology depending on the conditions and the substrate surface on which it grew (Czajka-Jakubowska et al., 2009). Yin *et al* (2009) achieved a film of ordered FA crystals directly onto enamel surfaces, using near physiological conditions (Xie et al., 2011), this study demonstrated the evolution of the crystals at different incubation periods (Yin et al., 2009). This shows that a simple solution chemistry approach can regenerate human enamel, without the using any cells or proteins (in particular amelogenin, which governs crystal orientation). By applying this

principle to artificially demineralised enamel (model for dental caries), there lies a potential for a remineralisation regime to restore order back into the destructed architecture that arises from clinical caries.

Synthetic FA crystals have in the past been characterised using a variety of techniques, including FTIR, NMR and XRD (Chen et al., 2005; Chen et al., 2006). Ordered growth of the crystals have been observed using SEM, which is limited to only providing a qualitative representation of the surface area. To date the, there have been no quantitative measure of the degree of crystal order in the regenerated layer.

Therefore the objective of this study was to

1. Trial and test three established methods of crystal growth directly onto artificially demineralised enamel
2. Compare crystal morphology and sample coverage using SEM of each of the three methods and choose an optimal crystal growth treatment.
3. Quantify the degree of preferred orientation at a crystallographic level, using high resolution SXRD

10.2 Experimental design

Sample preparation

Permanent human molars were sectioned longitudinally, in the buccal lingual plane, using an annular saw. Artificial caries lesions were created by immersing each tooth section in 20 mls of 1 vol % acetic acid (buffered to pH 4 using NaOH pellets) for 3 days or 7 days. Once removed from the acid solution samples were thoroughly washed with distilled water and air dried. A small portion of enamel was then sectioned, to serve as a control.

Synthesis of FA nanostructures

The three treatments included in this study were:

1. Ambient pressure at 37°C (Yin et al., 2009)
2. Ambient pressure at 70°C (Wang et al., 2009)
3. Mild hydrothermal conditions (Chen et al., 2006)

These established treatments have previously been applied to other substrate surfaces including dental enamel and have successfully achieved a thin layer of organised FA crystals. These previous positive outcomes guided the selection of these three techniques as a basis for this study of apatite crystal growth on a substrate of demineralised enamel. The flow chart (Fig. 10.1) outlines the experimental process for this study.

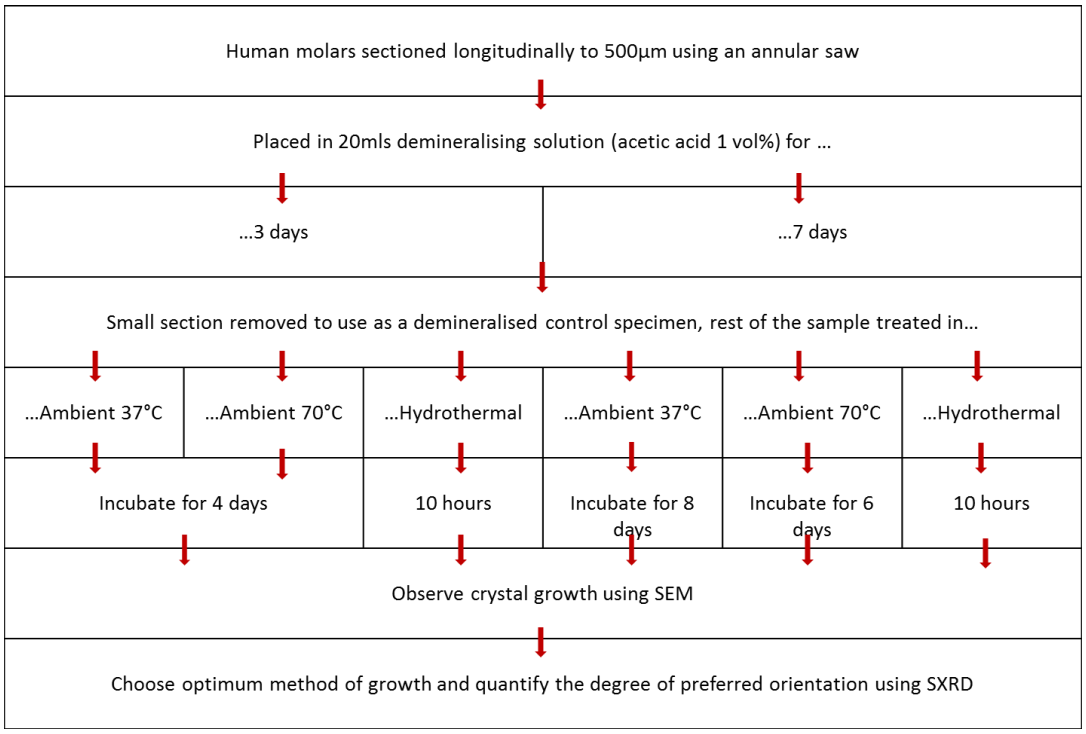

Figure 10.1: Step by step schematic of the experimental design and procedure for this study.

Slight modifications to the incubation time were made to the original protocol in order to observe the evolution of the crystallisation and to obtain desired morphology.

Ambient 37°C method

A solution containing 34 mg of $Ca_3(PO_4)_2$ and 278 mg of HEDTA was stirred for 3 mins, then 12 mg of KF and 82 mg of KH_2PO_4 were added. The final solution was adjusted to pH 6 by adding NH_4OH drop wise. Each artificially demineralised tooth section was immersed in 10 ml of this solution in a sealed glass beaker and placed into a water bath at 37°C, at ambient pressure for either 4 days (for the 3-day demineralised samples) or 8 days (for the 7-day demineralised samples). The tooth section was then rinsed with distilled water and air dried.

Ambient 70°C method

104.6 mg of HA powder and 8.4 mg of NaF powder were mixed with 100 ml of distilled water. The suspensions were stirred continuously; then the powder was dissolved by adding HNO_3 drop wise to the solution. NH_4OH was added drop wise with continuous stirring until it reached pH 6. The suspension with the enamel section was sealed in a glass beaker covered with aluminium foil and placed in a water bath at 70 °C and incubated for either 4 or 6 days.

Hydrothermal method

9.36 g of EDTA-Ca_2-Na_2 and 2.07 g of $NaH_2PO_4.H_2O$ were mixed with 90 ml of distilled water. The suspensions were stirred continuously until the powder dissolved. The pH was adjusted to 6 using NaOH. 0.21 g of NaF was dissolved in 10 ml water then added to the EDTA-Ca_2-Na_2 and $NaH_2PO_4.H_2O$ solution and stirred continuously. Demineralised enamel samples were positioned securely onto a raised stage in the beaker and then placed into an autoclave at 121°C at a pressure of $2.4x10^5$ Pa for 10 hours.

Microstructural Characterisation

The growth pattern and morphology of the synthetic crystals from each of the three treatments were observed under SEM. Samples were sputter coated with gold. From the images obtained, a decision was made as to which treatment would be studied further, based upon the following criteria:

1. Uniformity of coverage of ordered apatite crystals across the whole sample
2. Similarity of synthetic crystal morphology to that of natural enamel
3. Degradation of specimens (treated samples must remain intact to quantitatively measure the degree of order)

Nanoscale and Crystallographic Characterisation

Following the pilot study described above, in order to quantify the degree of preferred orientation, a 500 μm thick section from a permanent human (LL7 Lower left second molar) tooth was artificially demineralised for 7 days. Four tracks (2 horizontal and 2

vertical) across the enamel surface (Fig. 10.2) were measured using high resolution synchrotron X-ray diffraction on the BM28 (XMaS) beamline at the ESRF (described in Chapter 6). The section was then treated to the remineralising solution (Ambient 70°C method), and then the same four tracks were measured again. The intention of this "before" and "after" remineralising approach was to measure the extent of destruction and reconstruction respectively by observing changes in the intensity around the (002) reflection.

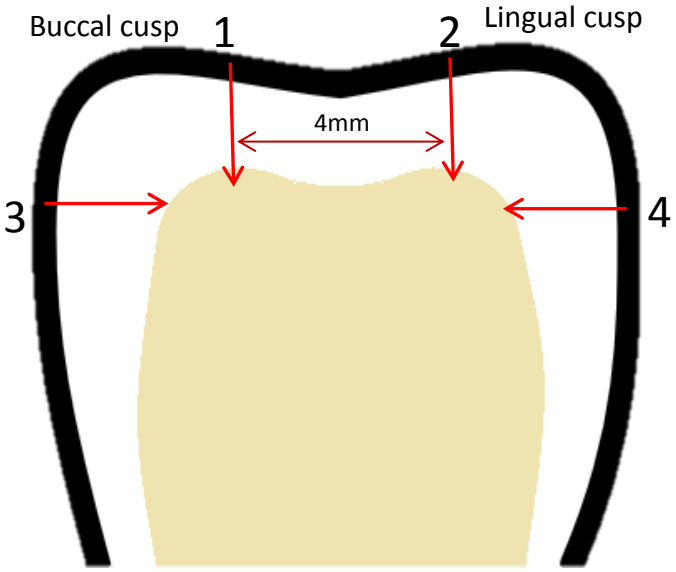

Figure 10.2: Schematic representation of the tracks measured using SXRD before and after synthesis of apatite crystal (ambient 70°C conditions).

Beamline setup

Samples were mounted by clamping the root of the tooth section onto the travelling platform and were scanned in two orthogonal directions. Regions of interest were located using the cross hairs of a telescope aligned to the centre of rotation of the sample. A MAR CCD detector (2048 x 2048 pixels) was placed directly behind the sample and perpendicular to the incoming beam direction in order to collect images in transmission to detect changes across small areas of interest.

Pre growth

An X-ray wavelength of 0.82 Å (equivalent to energy 15.1 keV) was used. The sample to detector distance was approximately 145 mm allowing a 2θ range of 5-35°. A 20 µm x 20 µm beam spot (defined using vacuum tube slits) was directed on to the mounted sample. Allocated beam time was in multi-bunch mode and so each diffraction pattern took 20 s to collect (including 8 s CCD camera processing).

Post growth

An X-ray wavelength of 0.82 Å (equivalent to energy 15.1 keV) was used. The sample to detector distance was approximately 175 mm allowing a 2θ range of 5-25°. A 80 µm x 80 µm beam spot (defined using vacuum tube slits) was directed on to the mounted sample. Allocated beam time was in 16-bunch mode set up, which increased data collection time to 60 s (including 8 s CCD camera processing) per diffraction pattern, which in total took approximately 9.5 hours to collect around 470 data files.

It should be noted that due to the lower flux of X-rays in 16-bunch mode, cutting the flux further by decreasing the spot size to 20 µm spot size was not feasible given the time constraints of the beam time awarded. Therefore it became necessary to increase the beam spot size to 80 µm, although this was a slight compromise in spatial resolution, it meant better data quality. In order to make a direct spatial comparison between the two sets of data collected, every fourth diffraction pattern (from the demineralised set of data) from the track measured was analysed.

10.3 Results and Discussion - Part 1: Pilot Study

The first set of SEM images demonstrate crystal growth on enamel sections demineralised for 3 days and incubated in either ambient pressure at 37°C or 70°C for 4 days; or treated with mild hydrothermal conditions. The original incubation time was initially modified (only for treatment in ambient pressure at 37°C and 70°C) and reduced in order to monitor the evolution of growth.

Demineralised enamel – 3 days

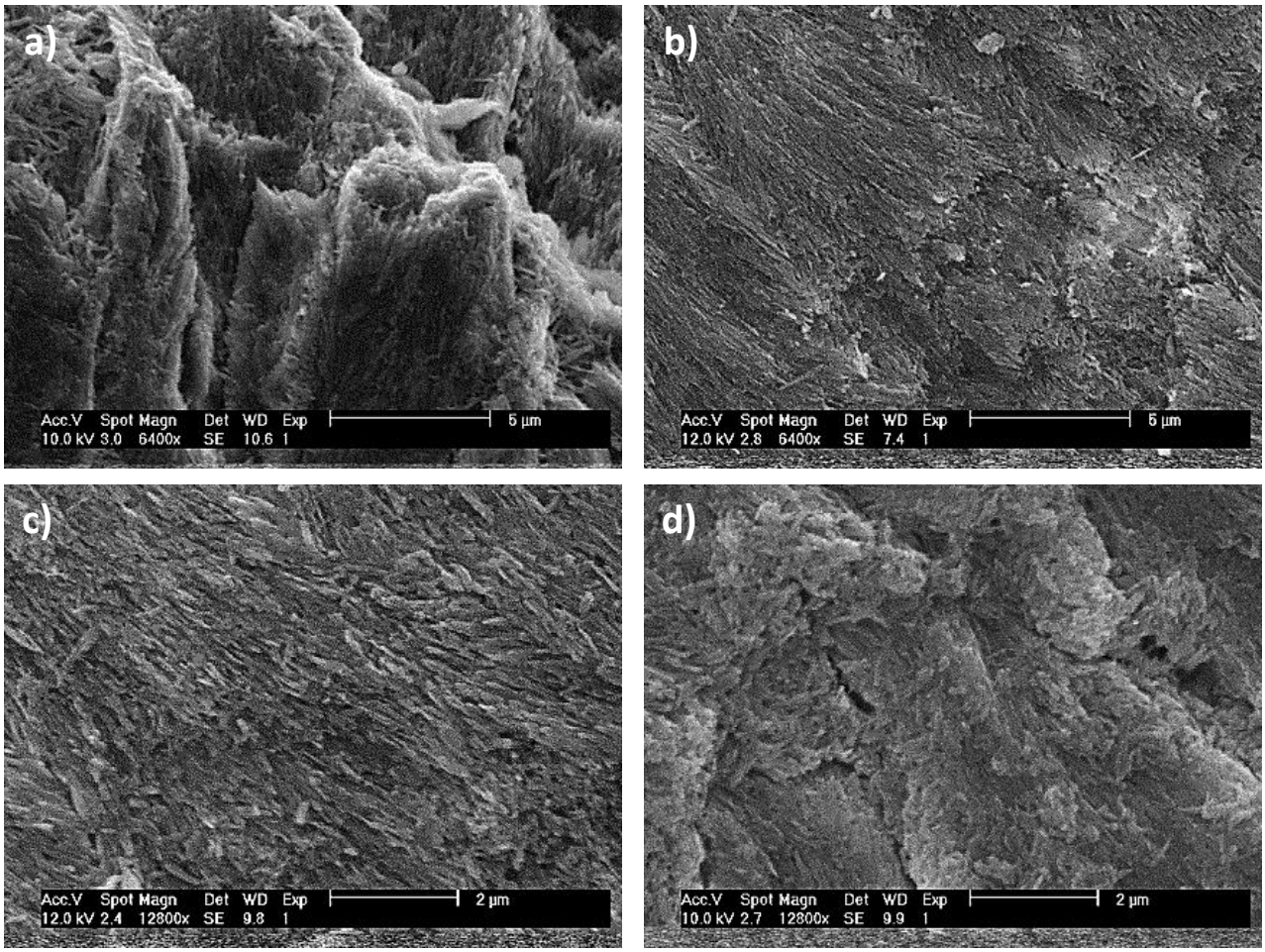

Figure 10.3: Scanning electron micrographs of natural permanent human enamel after 3 day dissolution depicting enamel a) prisms, b) ordered crystals, c) ordered crystals at higher magnification and d) demineralised region.

Figure 10.3 shows SEM images of enamel after 3 days in demineralising solution. Images reveal very little destruction caused to the enamel microstructure after 3 days in demineralising solution. In general the prismatic structure (Fig. 10.3a) and crystal arrangement (Fig. 10.3b and 10.3c) remain intact and have maintained their orientation; however Figure 10.3d shows demineralisation to have caused a slight loss in crystal organisation. Although initial mineral loss, in both primary and permanent enamel, with time is linear (Wang et al., 2006), from this it can be seen that 3 days of dissolution has not had a significant morphological effect on the microstructure.

Ambient 37°C method (following 3-day demineralisation)

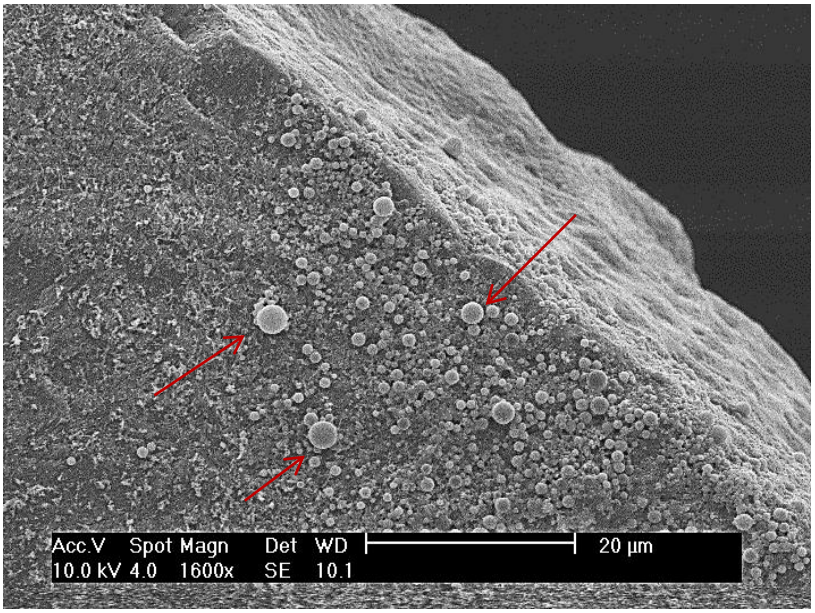

Figure 10.4: SEM images of a) demineralised substrate surface and b) after 4 days in ambient 37C method remineralising solution.

The sample immersed in the ambient 37°C suspension and incubated for 4 days exhibited poor crystal growth (Fig. 10.4) across the surface, however there was a presence of small, micron and nano sized spherical structures, some of which formed larger aggregates (indicated by red arrows) randomly dispersed across the surface of the enamel.

Ambient 70°C method (following 3-day demineralisation)

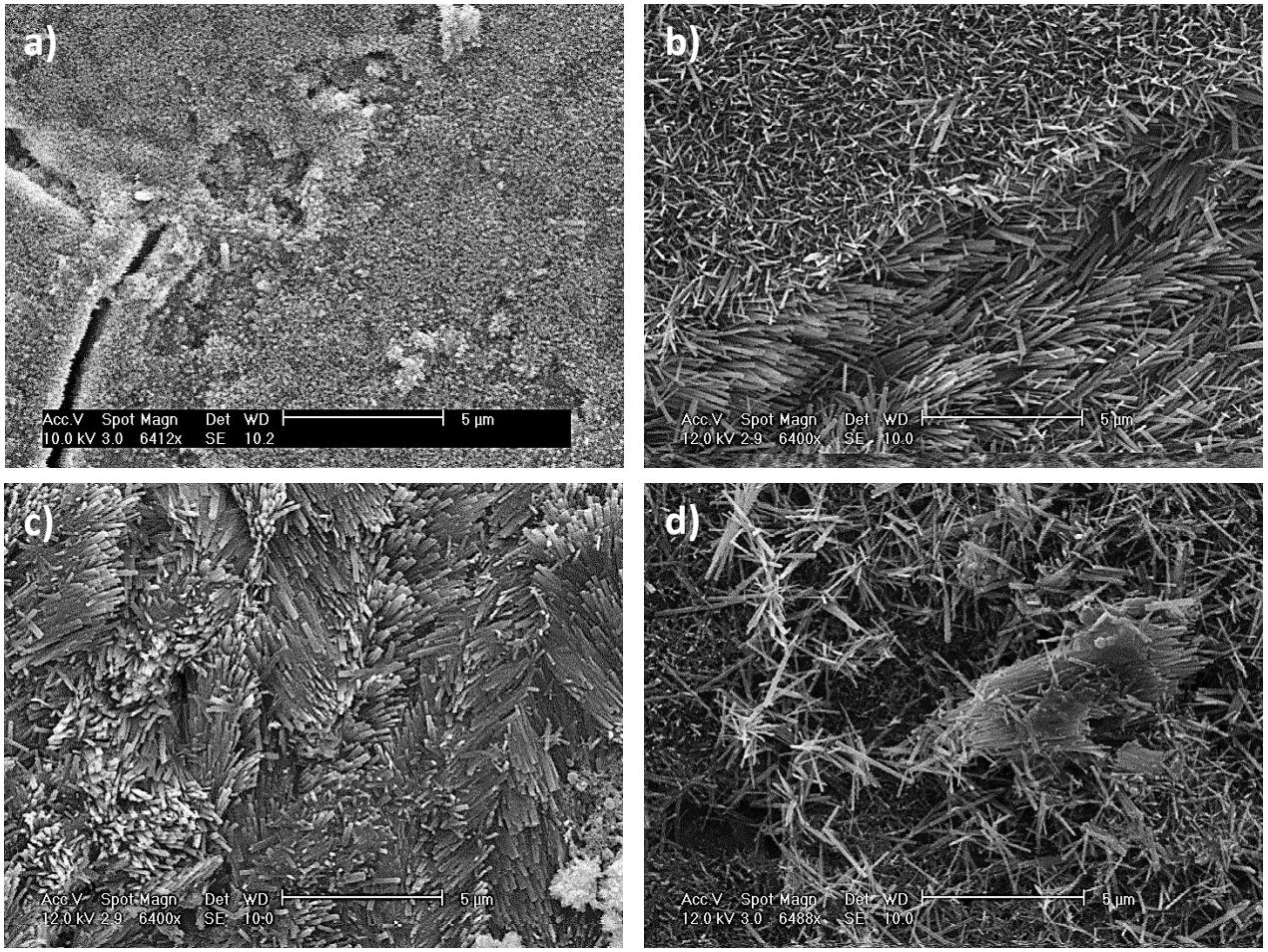

Figure 10.5: SEM images of synthetic enamel like apatite crystals (incubation for 4 days) grown directly onto 3 day demineralised enamel surface demonstrating the three variations in morphology observed: a) nanosized crystals, b) and c) long thin needle like structures displaying regions of directional growth and d) needle-like crystallites lacking directional order.

Full coverage of synthetic apatite crystals across the whole enamel surface was achieved using the ambient 70°C conditions. Fig 10.5 demonstrates the variations seen in the crystal morphology and arrangement. Fig 10.5a shows a region of the surface where the synthetic crystals form a thin film coating, made up of small nanosized crystals, whereas the other regions show the formation of thin needle like structures, giving a grass like appearance (Fig. 10.5b). There is evidence of both ordered directional growth (Fig. 10.5c) and areas

where thin crystals have been deposited on to the surface (Fig. 10.3d). Despite some directional orientation in some regions, generally there is an absence of bundling of the synthetic crystal into prism-like structures.

Hydrothermal Treatment (following 3-day demineralisation)

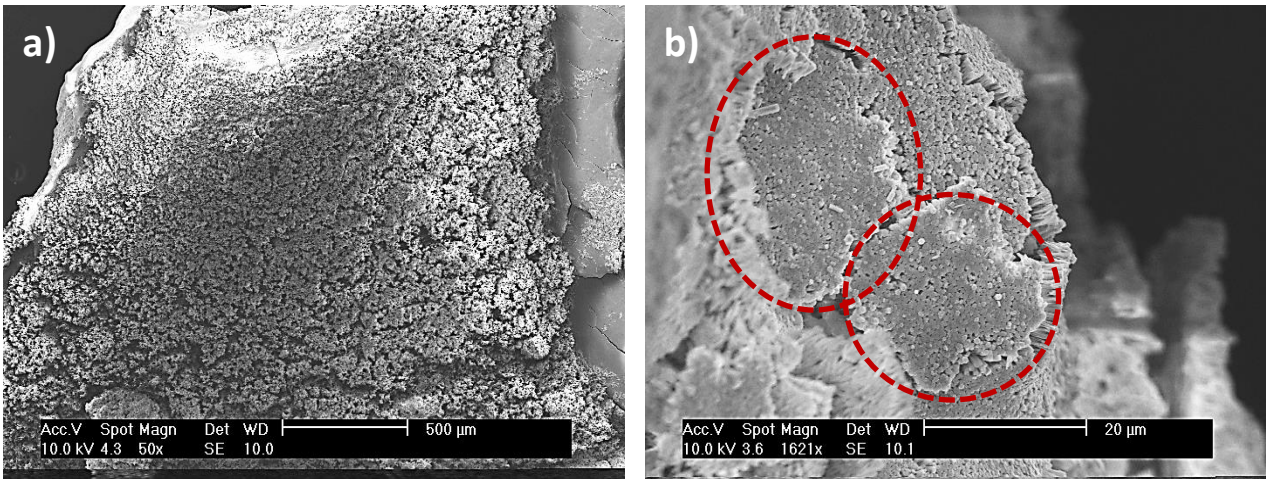

Figure 10.6: SEM images of synthetic enamel like apatite crystals grown directly onto 3 day demineralised enamel surface under mild hydrothermal conditions, resulting in evidence of a) dense coverage of ordered crystals and b) bundling to form prismatic structures.

The SEM images of specimens treated under hydrothermal conditions show growth of well-ordered apatite crystals which appear enamel-like in their microstructural arrangement, with uniform coverage across the sample (Fig. 10.6a). The morphology of the synthetic apatite showed thick, long crystallites with hexagonal faces. There was evidence of crystals bundling together to form prism like structures (Fig. 10.6b), with an approximate diameter of 5 to 10µm (indicate by red circles). It should be noted that following this treatment, the high temperature and elevated pressure caused the enamel sample to be extremely fragile and brittle.

Demineralised enamel – 7 days

Since the goal of the pilot study was crystallite-growth optimization, following the observations presented in 10.3.1, the methodology was modified for optimization. Firstly it

was decided to increase both the demineralisation time from 3 to 7 days and the remineralisation time from 4 to 6-8 days in order to mimic the effect of a greater lesion and to give greater subsequent apatite growth (this follows the protocol of the original design study (Yin et al., 2009)). In addition this methodology is consistency with the demineralisation regime presented in Chapter 9. Secondly, the remineralising suspension volume was increased to 50 ml. In Section 10.3.1, the specimens were immersed in a 10 ml suspension; however the small volume made it difficult to measure pH changes during the treatment, as readings were not stable. Thirdly, after a period of 5 days each sample was replenished with fresh remineralising solution to aid growth. Finally, due to the fragile nature of samples treated hydrothermally, it was decided to discontinue this methodology.

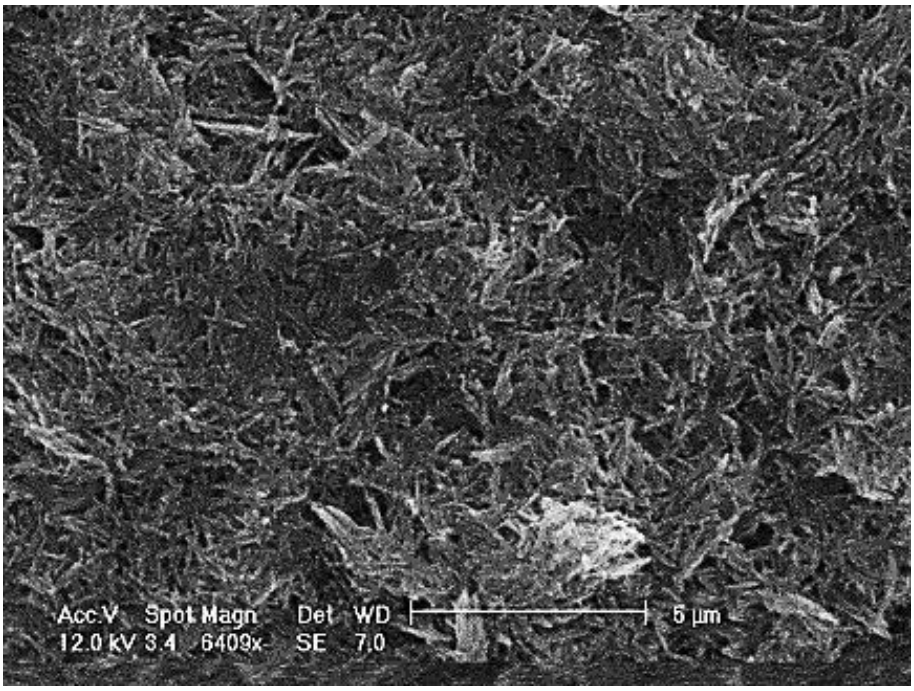

Figure 10.7: SEM of natural human enamel after 7 day dissolution (pH4) acetic acid.

The SEM images show the effect of increased demineralisation time on enamel morphology. After 7 days of demineralisation, disruption of the enamel microstructure can be seen by a loss of crystal alignment and no evidence of prismatic structure such as prism boundaries (Fig. 10.7).

Ambient 37°C (following 7-day demineralisation)

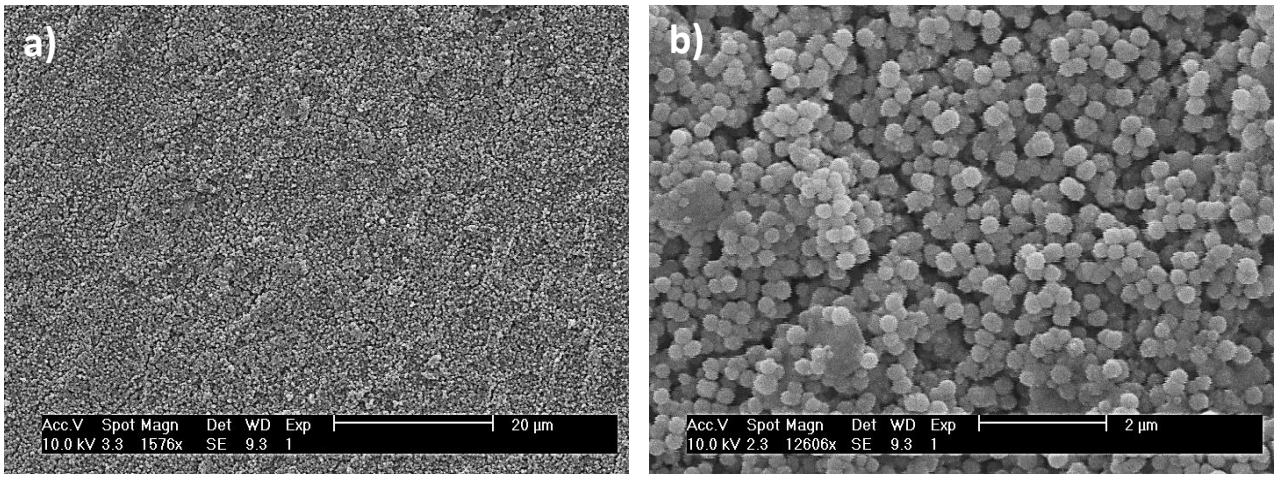

Figure 10.8: SEM images of synthetic enamel like apatite crystals (incubation for 8 days at 37°C a) grown directly onto 7 day demineralised enamel surface b) magnified showing small spherical structures.

When the incubation time was increased (Fig. 10.8), the SEM images reveal coverage that is more dense and more uniform on the enamel surface in comparison to the shorter incubation time in Figure 10.4. Figure 10.8a shows a large surface of the enamel sample which is covered entirely by a thin film of small compact crystals. The layer of newly formed crystals completely covers the natural enamel such that the underlying enamel cannot be seen nor can be identified the regions used as nucleation sites (pits and kinks). Growth occurred such that the crystal faces (the *c*-axis) of the crystals were perpendicular to the plane of the surface on which it grew on (Fig. 10.8b). These synthetic crystals too the shape of small spherical structures, with signs of emerging hexagonal faces. The growth pattern of the synthetic crystals was homogenous as the same crystal morphology was seen across the whole surface of the substrate.

Ambient 70°C (following 7-day demineralisation)

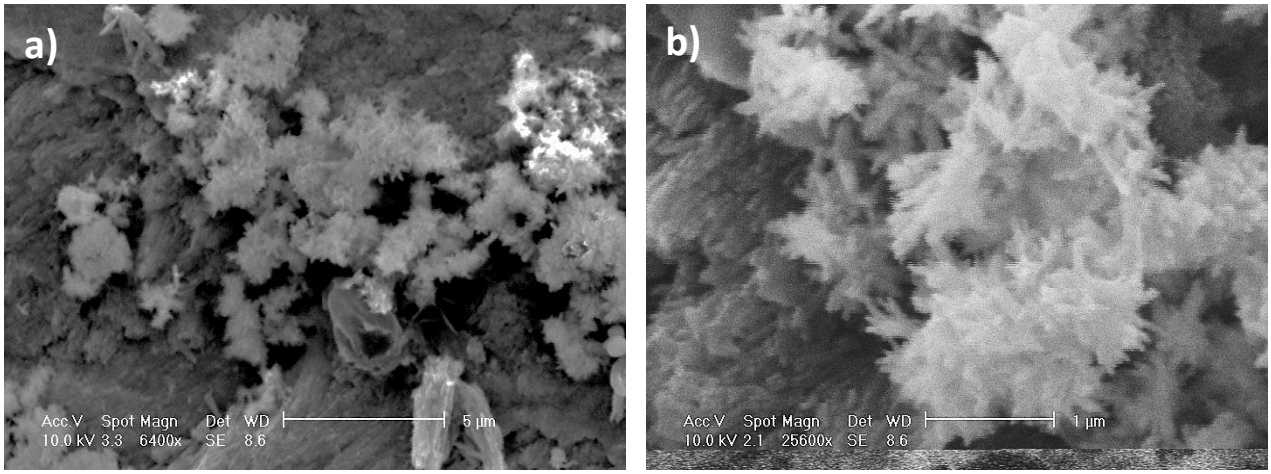

Figure 10.9: SEM images of synthetic apatite crystals (incubation for 6 days) a) present within the prism cores, b) displaying a flower like structure, grown directly onto 7 day demineralised enamel surface.

Longer crystals were once again evident on the sample incubated in ambient 70°C condition in comparison to those produced at ambient 37°C. Although the resulting crystals were thin needle like structures, they did not exhibit the same morphology as was seen in the first set (Fig. 10.5). These crystals were thicker in width and not as flat. Bundles of crystals were arranged in a flower like structure (Fig. 10.9a), which meant individual crystallites had different directional growth (Fig. 10.9b). Although crystallisation was not homogenous (i.e. different morphologies, as with the previous set) and there was no intact layer formed, coverage was moderately good across the surface of the substrate. In addition there was more growth in regions where crystals had preferentially dissolved, such as the prism cores (Fig. 10.9a).

Evaluation of growth treatments

The SEM images provide a qualitative representation of the crystal growth on demineralised enamel from each of the three physicochemical treatments. The results presented above were used to choose an optimum method for further analysis and to quantify the degree of order achieved from the synthetic crystals. The first set of data represents the crystallisation directly onto enamel sections which were artificially

demineralised for 3 days. This period of time presented to be insufficient in causing mineral loss or morphological changes through dissolution. Figure 10.3 shows enamel maintains its microstructural integrity, causing very little damage and disruption to the crystal orientation and prismatic structure. However, even in the absence of any surface defects or roughness, which would potentially serve as nucleation sites or templates for growth of partially dissolved crystals, tooth sections displayed evidence of crystal growth, with varying coverage and morphology depending on the treatment. This was due to the fact that enamel samples were placed in a supersaturated solution to allow it to overcome the large energy barrier of nucleation (Chen et al., 2006).

Samples treated with the ambient 37°C condition produced the least amount of synthetic crystals, with only a few small sized, randomly dispersed spherical structures. The ambient 70°C condition on the other hand presented an overall moderate coverage, with morphology ranging from a thin layer film of nano sized spheres, to ordered thin needle like structures. The hydrothermal treatment produced the best results, in terms of coverage and morphology, as the entire tooth was homogenously covered with long hexagonal crystals, extending to approximately 10µm along the *c*-axis, bundling together to give a prism like appearance, similar to that of natural enamel microstructure. However due to the harsh conditions of the treatment, acidic pH, high temperature and pressure, the natural enamel substrate had partially dissolved causing the overall structure to be extremely weak and brittle. The mild hydrothermal treatment was no longer carried forward.

Increase in the demineralisation period had an effect on the natural enamel microstructure, causing disruption to the crystal orientation within the prismatic structure. Along with this, the incubation time for both the ambient 37°C and ambient 70°C treatments were increased to 8 days and 6 days respectively. The former resulted in a tightly compact homogenous film of well-ordered small crystals with emerging hexagonal faces covering the entire surface whereas the latter presented moderate coverage of long needle like structures, with sharp spear like ends.

The crystallisation pattern seen from the ambient 37°C condition in the first instance is more likely to be due to reduced incubation time rather than the lack of nucleation sites on

the substrate surface, as the presence of small nucleates on the surface after 4 days was an indication for potential of growth. These small spherical structures are observed as they are kinetically favoured and display a lower surface energy. Such structures would be expected within 15 minutes of incubation (Yin et al., 2006). With a longer incubation period the small structures not only increased in quantity but also began to exhibit compact nanorods with hexagonal faces, which is thermodynamically stable, however did not grow much in length. HEDTA was added to the suspension as a chelating agent to form longer apatite crystals, as this ultimately controls and stabilises the rate at which Ca^{2+} is released, so that not all of the ions are used up straight away. Yin et al, (2006) achieved this morphology after 4 days of incubation. It is possible achieve ordered enamel like crystals directly on to demineralised surfaces with longer incubation time (to compensate for the low energy at lower temperature) and continuous replenishment of supersaturated solution (increase in the $[Ca^{2+}]$).

A completely different morphology and growth pattern was noticed when growing crystals at a higher temperature. The ambient 70°C treatment produced a combination of small crystals and ordered thin needle like structures. With increasing incubation time, the crystals evolved and grew in both length and thickness; bundles of these crystals took a flower like morphology branching from a central nucleate.

Both HEDTA and EDTA were used as a chelating agent to produce longer crystals by slowing down the release of the calcium ions in the ambient 37°C and hydrothermal methods respectively. Calcium is divalent; it has two positive charges, which is strongly attracted electromagnetically by the open ended HEDTA in the solution. This results in the calcium ion being incorporated into the HEDTA molecular structure, forming a closed ring. This conserves the Ca during the incubation time and releases it slowly, which will result in the synthesis of longer crystals rather than if all the Ca ions were used up immediately without the presence of HEDTA (Chen et al., 2006).

The mechanisms by which small nucleates grow into larger crystals can be explained by the thermodynamically driven, Ostwald ripening process, which fundamentally principle describes the growth of larger particles at the expense of smaller particles. From a

standpoint of kinetics, it is easier to nucleate many small crystals as it is kinetically favoured, whereas large crystals are thermodynamically favoured. Larger particles have a lower surface to volume ratio and are more energetically stable than smaller particles. Molecules at the surface of small particles are energetically less stable than those packed tightly within it and therefore dissociate into the solution shrinking the particle over time and increasing the number of free molecules in solution. The free molecules in the supersaturated solution redeposit on the larger particles in order to reach a more thermodynamically stable state where the surface to area ratio is minimised. This continues until small particles decrease in size until they disappear and large particles grow even larger.

The Final Decision

As previously mentioned, obtaining beam time to measure samples is extremely competitive and time is often very limited, therefore only one treatment was measured. Careful consideration was made by evaluating each treatment and through a process of elimination, based on the characteristics of the crystallisation process, and fulfilment of the initial criteria, the ambient 70°C treatment was chosen for further investigation. The hydrothermal method was eliminated early in the study on the basis that the demineralised enamel was unable to withstand the harsh conditions of the treatment, acidic pH, high temperature and pressure, caused enamel to became extremely weak and brittle and partially dissolved. It was important that the sample remain intact after treatment, as samples would be measured in transmission geometry. It was desired for the preferred orientation to be measured as a function of position to observe the organisational behaviour of the synthetic crystals. If the chosen treatment were to be translated into clinical practice then it would important that the rest of the healthy enamel remain unaffected. The ambient 37°C treatment was included in this study as a method to trial due to the successful ordered growth shown in at a low temperature. Although a homogenous layer of ordered crystals were produced, the rate of growth presented to be fairly slow, as crystals only started evolving into the hexagonal morphology, crystals were also very small in size, about 10 nm and had not grown in length. The ambient 70°C was chosen for further texture analysis. Crystals exhibited a variety of morphologies, which meant that some areas were still

growing. It was seen that with increased incubation time, crystals grew in size, especially in thickness. Crystals bundled together to for a flower like structure.

10.4 Results and Discussion – Part 2

The previous study was carried out as a pilot to determine the optimum growth conditions directly on to demineralised enamel. Three established methods were tried, all with varying characteristics and morphologies. Through a process of elimination the ambient 70°C method was selected for characterisation of orientation. A 500 µm thick section from a permanent human (LL7 Lower left second molar) tooth was placed in demineralising solution (1 vol % Acetic acid pH4) for 7 days, then washed with distilled water and measured using SXRD on the XMaS beamline at the ESRF. The sample was treated with ambient pressure at 70°C and then re-measured using on the XMaS beamline at the ESRF.

Demineralised enamel

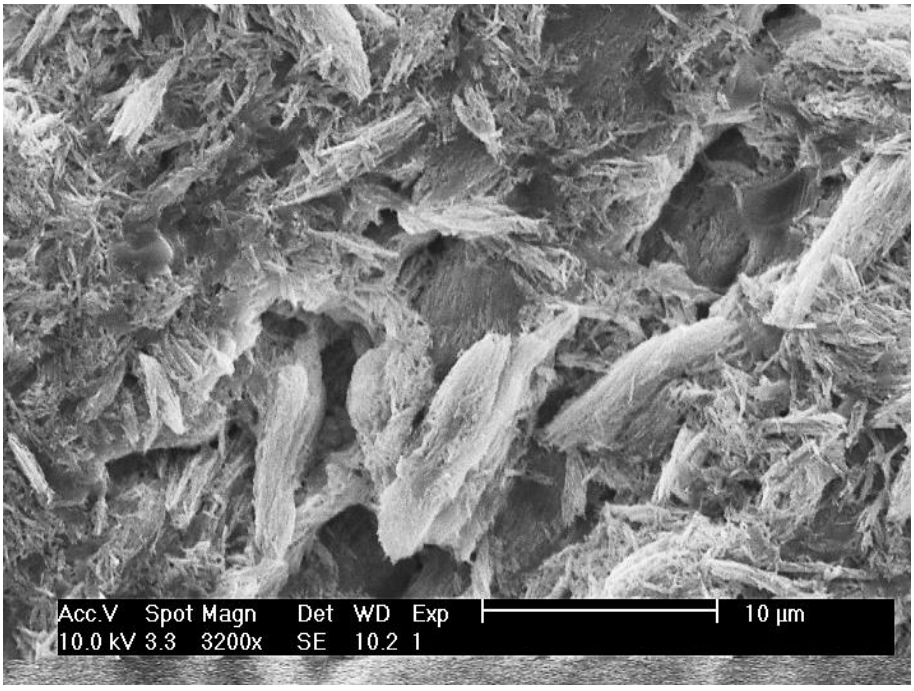

Figure 10.10: SEM of natural human enamel after 7 day dissolution (pH4).

SEM images show microstructural damage, by loss of apatite crystal orientation (Fig. 10.10) resulting from dissolution. Although there is evidence of the presence of some prismatic structure, crystal alignment is severely affected.

Synthetic crystals

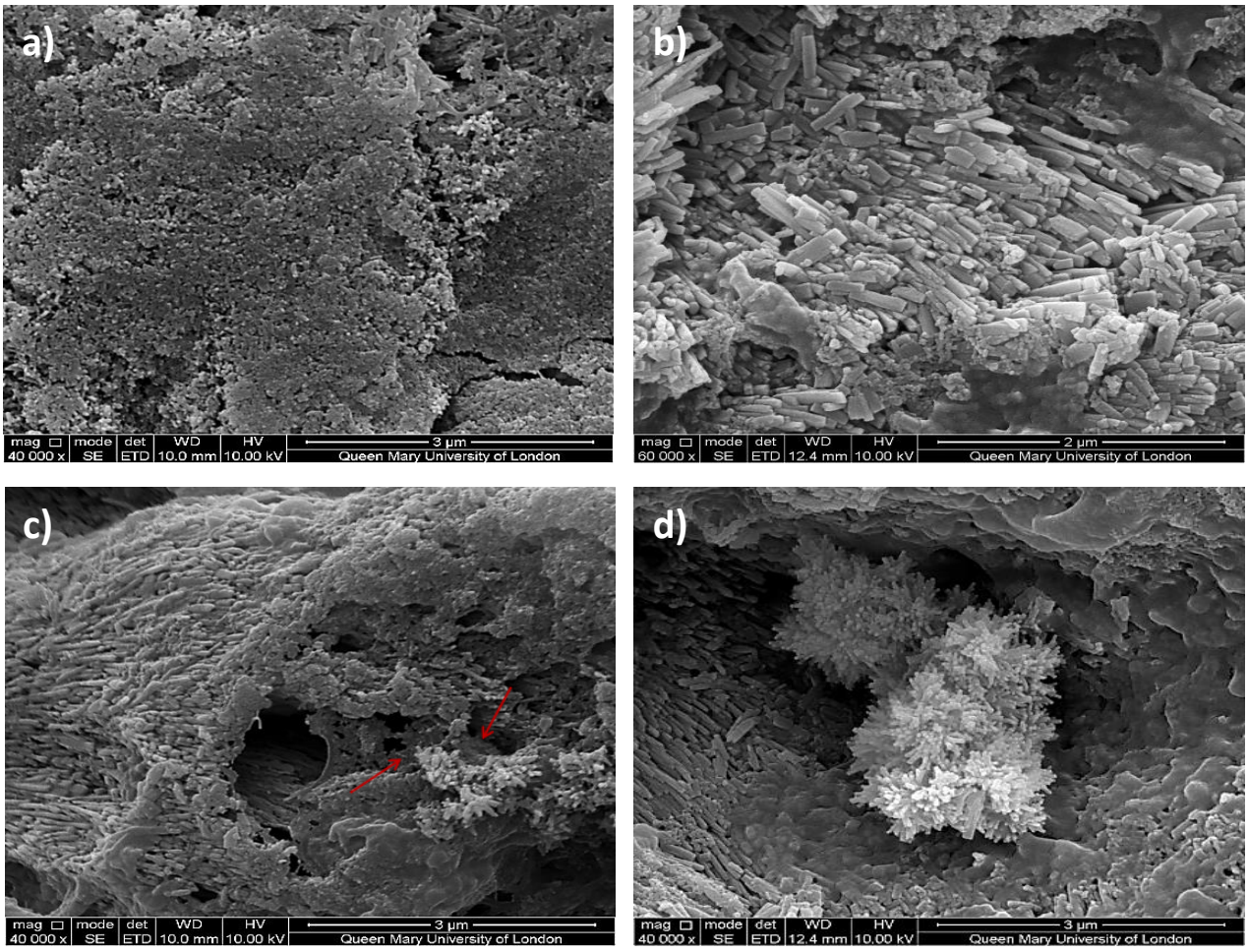

Figure 10.11: SEM images of synthetic apatite crystals grown directly onto demineralised enamel surface, morphologies include a) ordered bundles, b) thick ordered crystals, c) crystals growing near prism core and d) flower like structure inside prism core.

An even coverage of growth was achieved across the entire surface area; however crystal morphology was heterogeneous with no particular pattern. Once again, different morphologies are presented by the synthetic crystals, including small nano sized particles

crystals organised in a cluster (Fig. 10.11a). Long thick ordered crystals were evident (Fig. 10.11b), as well as flower like structures (Fig. 10.11c) seen growing in the empty prism cores (Fig. 10.11d). The synthetic crystals displayed an approximate cross section of 50-60 nm and length along the *c*-axis of 200-500 nm.

Preferred orientation

Results of the four tracks measured at a high spatial resolution using synchrotron radiation are shown in figure 10.12. In order to determine the restoration of enamel lesions by the synthetic layer, measurements were taken after demineralisation and then after remineralisation through synthetic growth. The graphs represent the four measured tracks, each showing two plots for preferred orientation, demineralised natural enamel (black circle) and synthetic growth on natural enamel surface (red square).

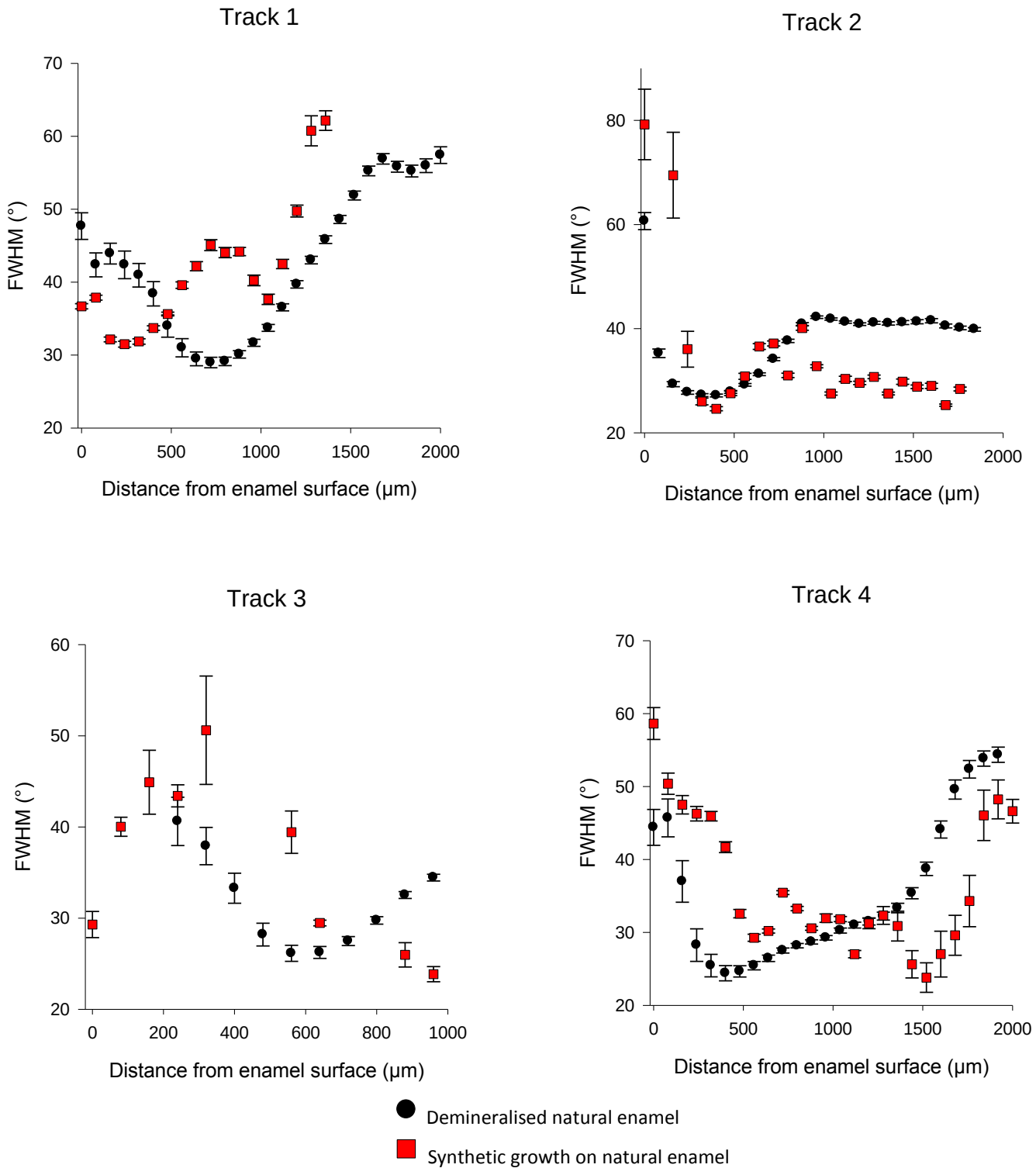

Figure 10.12: Graphs representing the FWHM tracks after demineralisation and after synthetic growth.

The graphs represent changes in the FWHM value as a function of position from enamel surface towards the EDJ. In general the artificially demineralised enamel exhibit low FWHM angles, similar to that of healthy enamel (between 20-40°), which suggests a degree of crystal orientation persists even after treatment with demineralising solution. Although the SEM images (Fig. 10.10) showed a disturbance of crystal alignment due acid attack of the microstructure, dissolution of the enamel shows to have had little effect on the crystallographic organisation. The natural surface of each track display higher FWHM angles than the bulk enamel, indicating this to be the area of structural loss. No apparent pattern in either the loss of crystal organisation (other than the surface) after demineralisation in the natural enamel or in the organisation of the synthetic crystals was seen as a function of position.

Both tracks 1 and 4 show similar features in the demineralisation, the greatest loss in texture occurred in the first 200 µm from the surface, the bulk of the enamel between 500-1000 µm and 500-1500 µm respectively display the lowest FWHM values indicating that it maintains its structural integrity and crystal order. The steadily increasing angles in the last 500-600 µm is an expected trait of dental enamel, as it is a graded structure and orientation is lost on approaching the EDJ . In track 1, the newly synthesised crystals have an opposite relationship with the demineralised crystals, whereby the lower FWHM values are seen at regions where demineralised crystals give higher FWHM angles, i.e. crystal organisation is restored in areas where the greatest damage was caused from dissolution. Regions where enamel is ordered (the bulk), the synthetic crystals do not display ordered growth. This trend was seen within the first 1 mm from the surface of the tooth section in track 1, and as a general in track 2 and 3.

The demineralised track from track 2 shows isotropic crystal organisation with very little variation across the track distance. The same was seen for the synthetic crystals; continuous low values of the FWHM angle indicate ordered growth across the whole track. Overall, the greatest loss of texture is seen at the surface of track 2, whereas the bulk of the enamel remains intact. It can be seen that the region at which the greatest disruption has occurred is

the region whereby the synthetic crystal display the greatest order. Furthermore at the bulk of the enamel the synthetic crystals display high FWHM values indicating that less order.

10.5 Discussion

Evidence from the SEM images (Fig. 10.11c) suggests that crystallisation can occur in regions where mineral has been lost. The demineralised enamel provides nucleation sites, which is the reason for greater order gained in demineralised areas. Surface properties have great influence on the crystal growth (Czajka-Jakubowska et al., 2009). There are two reasons as to why a highly ordered structure is not seen across the whole track. The first is the differences in morphology. The flower like structures were present (Fig. 10.11d) in areas exhibiting higher FWHM angles, crystals had bundled to form flower like structures rather than prism like structures. Secondly there are areas present whereby crystals have simply nucleated and grown on top of the natural surface. This is seen in areas where natural crystals have maintained their order, thus synthetic crystals deposit on top as there are no partially dissolved crystals to restore.

It is important to point out that the whole section was immersed into the acidic solution; all areas were exposed, causing attack from all possible directions. Other demineralisation studies use a coat of varnish to protect the enamel and focus on a particular region. However the nature of this study was to create nucleation sites across a large surface area, which is why the enamel was not coated in varnish.

10.6 Conclusion

This study has evaluated the growth of synthetic enamel like apatite crystals from three physicochemical methods directly onto demineralised enamel sections. Variations in coverage and morphology were attributed to a number of factors, including incubation time, temperature and substrate surface. The chosen treatment, ambient pressure at 70°C, provided evidence of different morphologies, from spherical structures to needle like structures, the crystallographic data revealed ordered crystallites where it was needed most. Although no distinct pattern of directional growth was observed when measuring the degree of preferred orientation in both the demineralised enamel and the synthetic crystals, it can

be seen that order was restored in regions whereby greatest dissolution occurred. It is likely that these are regions that incurred greatest damage and therefore gave rise to greater surface defects to act as nucleation sites.

Results from this study show great potential in the crystallographic restoration of ordered crystals in demineralised enamel samples. The treatment is also one that can be translated into clinical practice (with slight modifications). The results of this study have contributed to the understanding of the sites at which synthetic apatite crystals are most likely to compensate in the regions where most disruption has occurred.

Chapter 11: Combined Discussion, Conclusions and Future Work

11.1 Combined Discussion

The overall aim of this study was to use advanced and complementary X-ray techniques to characterise the structure of dental enamel affected by genetic mutations and environmental influences in order to aid our understanding of the process of biomineralisation and bio-demineralisation by observing disturbances in the structure at multiple length scales.

A number of X-ray techniques have previously been used to establish enamel microstructure, most of which provide qualitative data or information over an average mass, which neglect spatial variation, and involve a destructive method of sample preparation. X-ray microtomography provides a non-destructive approach to accurately quantify the mineral concentration and synchrotron X-ray diffraction spatially measures the crystallographic parameters.

The results presented in Chapters 7 and 8 focussed on enamel affected by Amelogenesis Imperfecta: a rare yet important group of genetic disorders. A significant amount of studies have been carried out to understand the basis of this disorder, most of which have been at a molecular level in order to determine the exact genetic mutation and the possible implication during enamel formation. Although links have been made to the resulting structure, this was the first study to reveal a full quantitative analysis of the crystallographic properties of AI samples as a function of position.

In Chapter 7 deciduous enamel characterised with hypoplastic AI as a result of a mutation in the ENAM gene was characterised. The two enamel samples obtained from separate individuals with the same genetic disorder showed disruption in the mineral density distribution and the crystallographic texture. Importantly, differences in severity of disruption in both mineral concentration and texture between the individuals were observed. It is not uncommon to see clinical differences in severity in different patients with the same condition. In this case it is interesting because the precise genetic mutation is

known, however differences are still observed between different individuals. This suggests that in Amelogenesis Imperfecta, as with other musculoskeletal conditions, a combination of genetics and environment give rise to the final structural and clinical phenotype observed.

The study presented in chapter 8 on enamel samples from the permanent dentition clinically diagnosed with the hypomaturation subtype of AI shows a more uniform and localised defect, with only slight variation in the severity between the two sections measured. The WH phase was not present in the hypomature enamel.

Comparing the results in Chapter 7 and 8, there were some structural characteristics that were common to both sub-types of AI, and some which were distinct. Hypoplastic and hypomature enamel show lower mineral concentration, however areas of lower texture in hypoplastic enamel showed fusion of crystals whereas in hypomature enamel, crystals are small and thick and lack bundling (prismless enamel). Comparing the severity of disruption in enamel between the two AI subtypes, it could perhaps be the case that hypomature enamel shows a more consistent structural phenotype whereas hypoplastic enamel is more likely to vary in severity. This interpretation of the sub-types of AI would need further investigation with a larger number of enamel specimens in order to confirm it. In hypomature enamel, lower texture is limited to the tooth surface (including cusps) whereas the surface of hypoplastic enamel displays greater order. Lower preferred orientation is seen generally closer to the EDJ.

Limitations in this study included, restricted sample size due to the type of disorder. Amelogenesis Imperfecta is a rare genetic disorder, which means sample collection can often be limited. Clinical phenotyping of AI is an imperfect system and can possibly lead to misdiagnosis; with known genetic mutations results could be stronger. AI brings with it different enamel defects, the weak and brittle enamel can become further damaged or even completely lost during sample preparation.

The anisotropic nature of enamel and the inter and intra natural variation which occurs makes it essential to consider type matched control, however, healthy controls can

sometimes be difficult to obtain, due to the tooth type or the fact that it may have a subsurface lesion.

A further limitation was the experimental setup, all diffraction data was collected using synchrotron radiation, and as previously mentioned obtaining beam time is a peer-reviewed, highly competitive process, with most beamlines 4-5 times oversubscribed. Time is restricted so compromises had to be between the number of samples, thickness to beamspot size ratio, resolution and counting time. Furthermore it is difficult to repeat experiments as there are always slight differences in each experimental set up. Experiments had to be well planned in advance in order to utilise maximum time. Familiarity of the beamline and optics often proved to be advantageous. This was a limitation as seen in chapter 7. Differences in the beam set up can include, different filling mode (different current and flux) which affect the flux and thus counting statistics. Changes in the optics set up can have an impact on data collection and quality. Replacing slits with compound refractive lenses (CRLs) can be used to define the beam without losing flux.

In Chapter 9 and Chapter 10, the effect on enamel structure of natural and synthetic demineralisation and remineralisation processes were characterised. In Chapter 9 it was shown that, remineralisation of demineralised enamel not only restores mineral concentration (as has been shown by other studies ref s) but also enamel organisation and texture is restored (Siddiqui et al 2014 in press).

Chapter 10 was a quantitative measure of level of order from synthetic crystal growth. Being able to achieve ordered crystallites from a supersaturated solution, this can be translated in to clinics and used to treat early caries lesions.

11.2 Conclusions

The implications of the results presented in this thesis include

1. Greater understanding of crystallite orientation (quantitative)
2. Aid in our understanding the genetic and environmental factors
3. Aid better diagnosis and treatment regimes
4. Establish a technique for studying AI and caries

11.3 Future work

In addition to experimental repeats and possible modifications to the experiment set up/ design described in this thesis, the suggestions below are proposed to improve accuracy, validate findings, and continue the research themes of this thesis.

1. In situ measurements of progression of dental caries

Chapter 9 quantifies the destruction and re-formation of enamel crystallites during demineralisation and remineralisation respectively. To further clarify the crystallographic mechanism that occurs during the caries process as a function of time. By doing so, this can give us a time scale as to when greatest loss in texture is most likely to occur.

2. Refine synthetic model for white spot lesion/demineralisation
3. Diffraction tomography

Amelogenesis Imperfecta is a rare developmental disease, and obtaining samples can prove to be difficult. Furthermore it is of most importance to get spatial information. Sectioning the enamel samples results in loss of tissue, also AI samples are very weak and brittle, applying force from the diamond blade can cause breakage. Applying the method of high energy diffraction tomography samples remain intact.

4. Mechanical testing

To date there has only one study that tests the mechanical properties of different AI samples (Pavlic et al., 2007). Further investigation of the correlation between mechanical and structural properties of AI enamel can provide further insight in to the process of enamel formation.

5. Map the structural features across all types of AI subtypes

Further investigation of enamel samples require additional beam time. Results from this study are strong and positive enough to serve as a foundation for further proposals.

6. Use these techniques to study other conditions which affect enamel structure e.g. Molar incisor hypomineralisation (MIH)

References

AHMED, F. 2011. Multiscale Quantitative Imaging of Human Femoral Heads Using X-ray Microtomography. Ph.D thesis. *Institute of Dentistry*, Queen Mary University of London.

AHMED, M.2011. X-ray Microtomography Study of Carious Dentine and a Comparison of its Removal by Three Techniques. Ph.D thesis. *Institute of Dentistry*, Queen Mary University of London.

AL-JAWAD, M., SIMMONS, L. M., STEUWER, A., KILCOYNE, S. H., SHORE, R. C., CYWINSKI, R. & WOOD, D. J. 2008. Three dimensional mapping of texture in dental enamel. *Bioceramics, Vol 20, Pts 1 and 2,* 361-363**,** 877-880 1371.

AL-JAWAD, M., STEUWER, A., KILCOYNE, S. H., SHORE, R. C., CYWINSKI, R. & WOOD, D. J. 2007. 2D mapping of texture and lattice parameters of dental enamel. *Biomaterials,* 28**,** 2908-2914.

ALDRED, M. J., SAVARIRAYAN, R. & CRAWFORD, P. J. M. 2003. Amelogenesis imperfecta: a classification and catalogue for the 21st century. *Oral Diseases,* 9**,** 19-23.

ALMER, J. D. & STOCK, S. R. 2005. Internal strains and stresses measured in cortical bone via high-energy X-ray diffraction. *Journal of Structural Biology,* 152**,** 14-27.

ALQAHTANI, S. J., HECTOR, M. P. & LIVERSIDGE, H. M. 2010. Brief communication: The London atlas of human tooth development and eruption. *American Journal of Physical Anthropology,* 142**,** 481-490.

ANDERSON, P., BOLLET-QUIVOGNE, F. R. G., DOWKER, S. E. P. & ELLIOTT, J. C. 2004. Demineralization in enamel and hydroxyapatite aggregates at increasing ionic strengths. *Archives of Oral Biology,* 49**,** 199-207.

ANDERSON, P. & ELLIOTT, J. C. 1992. Subsurface Demineralization in Dental Enamel and Other Permeable Solids during Acid Dissolution. *Journal of Dental Research,* 71**,** 1473-1481.

ANDERSON, P., LEVINKIND, M. & ELLIOTT, J. C. 1998. Scanning microradiographic studies of rates of in vitro demineralization in human and bovine dental enamel. *Archives of Oral Biology,* 43**,** 649-656.

APPLEBAUM, E. 1932. Incipient Dental Caries. *Journal of Dental Research,* 12**,** 619-627.

ARENDS, J. & CHRISTOFFERSEN, J. 1986. Invited Review Article: The Nature of Early Caries Lesions in Enamel. *Journal of Dental Research,* 65**,** 2-11.

ATKINSON, M. E. & WHITE, F. H. 1992. *Principles of anatomy and oral anatomy for dental students*, Churchill Livingstone.

BANERJEE, A. & WATSON, T. F. 2011. *Pickard's Manual of Operative Dentistry,* Oxford, Oxford University Press.

BENIASH, E., SKOBE, Z. & BARTLETT, J. D. 2006. Formation of the dentino-enamel interface in enamelysin (MMP-20)-deficient mouse incisors. *European Journal of Oral Sciences,* 114 Suppl 1**,** 24-9; discussion 39-41, 379.

BERKOVITZ, B. K. B., HOLLAND, G. R. & MOXHAM, B. J. 2009. *Oral anatomy, histology and embryology,* Edinburgh, Mosby.

BLAU, S., KENNEDY, B. J. & KIM, J. Y. 2002. An Investigation of Possible Fluorosis in Human Dentition Using Synchrotron Radiation. *Journal of Archaeological Science,* 29**,** 811-817.

BOAS, F. E. & FLEISCHMANN, D. 2012. CT artifacts: causes and reduction techniques. *Imaging in Medicine,* 4**,** 229-240.

BOYDE, A. 1964. *The structure and development of mammalian enamel. PhD. [electronic resource]* [Online]. University of London.
BOYDE, A. 1989. Enamel. *Teeth.* Springer Berlin Heidelberg.
BRAGG, W. H. S. 1928. *An introduction to crystal analysis,* London, G. Bell & Sons.
BRALY, A., DARNELL, L. A., MANN, A. B., TEAFORD, M. F. & WEIHS, T. P. 2007. The effect of prism orientation on the indentation testing of human molar enamel. *Archives of Oral Biology,* 52**,** 856-860.
BROOKS, R. A. & DI CHIRO, G. 1976. Beam hardening in x-ray reconstructive tomography. *Physics in Medicine and Biology,* 21**,** 390-8.
BROWN, S. D., BOUCHENOIRE, L., BOWYER, D., KERVIN, J., LAUNDY, D., LONGFIELD, M. J., MANNIX, D., PAUL, D. F., STUNAULT, A., THOMPSON, P., COOPER, M. J., LUCAS, C. A. & STIRLING, W. G. 2001. The XMaS beamline at ESRF: instrumental developments and high-resolution diffraction studies. *Journal of Synchrotron Radiation,* 8**,** 1172-1181.
BUNGE, H. J. 1982. *Texture analysis in materials science : mathematical methods,* London, Butterworths.
COCHRANE, N. J., ANDERSON, P., DAVIS, G. R., ADAMS, G. G., STACEY, M. A. & REYNOLDS, E. C. 2012. An X-ray Microtomographic Study of Natural White-spot Enamel Lesions. *Journal of Dental Research,* 91**,** 185-191.
COFFIELD, K. D., PHILLIPS, C., BRADY, M., ROBERTS, M. W., STRAUSS, R. P. & WRIGHT, J. T. 2005. The psychosocial impact of developmental dental defects in people with hereditary amelogenesis imperfecta. *Journal of the American Dental Association,* 136**,** 620-630.
COLAÇO, M. V., BARROSO, R. C., PORTO, I. M., GERLACH, R. F., COSTA, F. N., BRAZ, D., DROPPA JR, R. & DE SOUSA, F. B. 2012. Synchrotron X-ray diffraction characterization of healthy and fluorotic human dental enamel. *Radiation Physics and Chemistry,* 81**,** 1578-1585.
CRAWFORD, P. J. M., ALDRED, M. & BLOCH-ZUPAN, A. 2007. Amelogenesis imperfecta. *Orphanet Journal of Rare Diseases,* 2**,** -.
CULLITY, B. D. 1978. *Elements of X-ray diffraction,* Reading, Mass. ; London, Addison-Wesley.
CUY, J. L., MANN, A. B., LIVI, K. J., TEAFORD, M. F. & WEIHS, T. P. 2002. Nanoindentation mapping of the mechanical properties of human molar tooth enamel. *Archives of Oral Biology,* 47**,** 281-291.
CZAJKA-JAKUBOWSKA, A., LIU, J., CHANG, S. R. & CLARKSON, B. H. 2009. The effect of the surface characteristics of various substrates on fluorapatite crystal growth, alignment, and spatial orientation. *Medical Science Monitor,* 15**,** Mt84-Mt88.
DARLING, A. I. 1956. Some Observations on Amelogenesis Imperfecta and Calcification of the Dental Enamel. *Annals of the Royal College of Surgeons of England,* 29**,** 354-369.
DARLING, A. I. 1961. The selective attack of caries on the dental enamel. *Proceedings of the Royal Society of Medicine,* 49**,** 759-765.
DAVIS, G., EVERSHED, A., ELLIOTT, J. & MILLS, D. 2010. Quantitative X-ray microtomography with a conventional source. *In:* STOCK, S. R. (ed.) *Developments in X-Ray Tomography Vii.* Bellingham: Spie-Int Soc Optical Engineering.
DAVIS, G., JAIN, N. & ELLIOTT, J. 2008. A modelling approach to beam hardening correction. *In:* STOCK, S. R. (ed.) *Developments in X-Ray Tomography Vi.* Bellingham: Spie-Int Soc Optical Engineering.
DAVIS, G. R. 1994. The effect of linear interpolation of the filtered projections on image noise in x-ray computed tomography. *J Xray Sci Technol,* 4**,** 191-9.
DAVIS, G. R. & ELLIOTT, J. C. 1997. X-ray microtomography scanner using time-delay integration for elimination of ring artefacts in the reconstructed image. *Nuclear Instruments & Methods in*

Physics Research Section a-Accelerators Spectrometers Detectors and Associated Equipment, 394**,** 157-162.
DAVIS, G. R. & ELLIOTT, J. C. 2003. High definition X-ray microtomography using a conventional impact X-ray source. *Journal De Physique Iv,* 104**,** 131-134.
DAVIS, G. R. & ELLIOTT, J. C. 2006. Artefacts in X-ray microtomography of materials. *Materials Science and Technology,* 22**,** 1011-1018.
DAVIS, G. R., EVERSHED, A. N. Z. & MILLS, D. 2013. Quantitative high contrast X-ray microtomography for dental research. *Journal of Dentistry,* 41**,** 475-482.
DAVIS, G. R. & WONG, F. S. L. 1996. X-ray microtomography of bones and teeth. *Physiological Measurement,* 17**,** 121-146.
DE CASTEELE, E. V., VAN DYCK, D., SIJBERS, J. & RAMAN, E. 2004. A model-based correction method for beam hardening artefacts in X-ray microtomography. *Journal of X-Ray Science and Technology,* 12**,** 43-57.
DE MAN, B., NUYTS, J., DUPONT, P., MARCHAL, G. & SUETENS, P. 1999. Reduction of metal streak artifacts in x-ray computed tomography using a transmission maximum a posteriori algorithm. *1999 Ieee Nuclear Science Symposium - Conference Record, Vols 1-3***,** 850-854.
DELBEM, A. C. B., SASSAKI, K. T., VIEIRA, A. E. M., RODRIGUES, E., BERGAMASCHI, M., STOCK, S. R., CANNON, M. L., XIAO, X. & DE CARLO, F. 2009. Comparison of Methods for Evaluating Mineral Loss: Hardness versus Synchrotron Microcomputed Tomography. *Caries Research,* 43**,** 359-365.
DEYHLE, H., BUNK, O. & MUELLER, B. 2011. Nanostructure of healthy and caries-affected human teeth. *Nanomedicine-Nanotechnology Biology and Medicine,* 7**,** 694-701.
DEYHLE, H., WHITE, S. N., BUNK, O., BECKMANN, F. & MÜLLER, B. 2014. Nanostructure of carious tooth enamel lesion. *Acta Biomaterialia,* 10**,** 355-364.
DOWKER, S. E. P., DAVIS, G. R. & ELLIOTT, J. C. 1997a. X-ray microtomography - Nondestructive three-dimensional imaging for in vitro endodontic studies. *Oral Surgery Oral Medicine Oral Pathology Oral Radiology and Endodontics,* 83**,** 510-516.
DOWKER, S. E. P., DAVIS, G. R., ELLIOTT, J. C. & WONG, F. S. L. 1997b. X-ray microtomography: 3-dimensional imaging of teeth for computer-assisted learning. *European Journal of Dental Education,* 1**,** 61-65.
DOWKER, S. E. P., ELLIOTT, J. C., DAVIS, G. R., WILSON, R. M. & CLOETENS, P. 2004. Synchrotron X-ray microtomographic investigation of mineral concentrations at micrometre scale in sound and carious enamel. *Caries Research,* 38**,** 514-522.
DOWKER, S. E. P., ELLIOTT, J. C., DAVIS, G. R., WILSON, R. M. & CLOETENS, P. 2006. Three-dimensional study of human dental fissure enamel by synchrotron X-ray microtomography. *European Journal of Oral Sciences,* 114**,** 353-359.
EGAN, C. K., JACQUES, S. D., DI MICHIEL, M., CAI, B., ZANDBERGEN, M. W., LEE, P. D., BEALE, A. M. & CERNIK, R. J. 2013. Non-invasive imaging of the crystalline structure within a human tooth. *Acta Biomaterialia,* 9**,** 8337-8345.
EL-SAYED, W., SHORE, R. C., PARRY, D. A., INGLEHEARN, C. F. & MIGHELL, A. J. 2010. Ultrastructural Analyses of Deciduous Teeth Affected by Hypocalcified Amelogenesis Imperfecta from a Family with a Novel Y458X FAM83H Nonsense Mutation. *Cells Tissues Organs,* 191**,** 235-239.
ELLIOTT, J. C. 1994. *Structure and chemistry of the apatites and other calcium orthophosphates,* Amsterdam [The Netherlands]; New York, Elsevier.
ELLIOTT, J. C. 1997. Structure, crystal chemistry and density of enamel apatites. *Dental Enamel,* 205**,** 54-72.

ELLIOTT, J. C., ANDERSON, P., GAO, X. J., WONG, F. S. L., DAVIS, G. R. & DOWKER, S. E. P. 1994. Application of scanning microradiography and X-ray microtomography to studies of bones and teeth. *Journal of X-Ray Science and Technology,* 4**,** 102-117.

ELLIOTT, J. C., BOLLET-QUIVOGNE, F. R. G., ANDERSON, P., DOWKER, S. E. P., WILSON, R. M. & DAVIS, G. R. 2005. Acidic demineralization of apatites studied by scanning X-ray microradiography and microtomography. *Mineralogical Magazine,* 69**,** 643-652.

ELLIOTT, J. C. & DOVER, S. D. 1982. X-Ray Microtomography. *Journal of Microscopy-Oxford,* 126**,** 211-213.

ELLIOTT, J. C., WONG, F. S. L., ANDERSON, P., DAVIS, G. R. & DOWKER, S. E. P. 1998. Determination of mineral concentration in dental enamel from X-ray attenuation measurements. *Connective Tissue Research,* 38**,** 61-72.

EVERSHED, T. 2013. A Multi-Material Approach to Beam Hardening Correction and Calibration in X-Ray Microtomography. Ph.D thesis. *Institute of Dentistry*, Queen Mary University of London.

FEARNE, J., ANDERSON, P. & DAVIS, G. R. 2004. 3D X-ray microscopic study of the extent of variations in enamel density in first permanent molars with idiopathic enamel hypomineralisation. *British Dental Journal,* 196**,** 634-638.

FEATHERSTONE, J. D. 2008. Dental caries: a dynamic disease process. *Australian Dental Journal,* 53**,** 286-91.

FELDKAMP, L. A., DAVIS, L. C. & KRESS, J. W. 1984. Practical cone-beam algorithm. *Journal of the Optical Society of America A,* 1**,** 612-619.

FINCHAM, A. G., MORADIAN-OLDAK, J., DIEKWISCH, T. G. H., LYARUU, D. M., WRIGHT, J. T., BRINGAS JR, P. & SLAVKIN, H. C. 1995. Evidence for Amelogenin "Nanospheres" as Functional Components of Secretory-Stage Enamel Matrix. *Journal of Structural Biology,* 115**,** 50-59.

FINCHAM, A. G., MORADIAN-OLDAK, J. & SIMMER, J. P. 1999. The structural biology of the developing dental enamel matrix. *Journal of Structural Biology,* 126**,** 270-299.

FINCHAM, A. G. & SIMMER, J. P. 2007. Amelogenin Proteins of Developing Dental Enamel. *Ciba Foundation Symposium 205 - Dental Enamel.* John Wiley & Sons, Ltd.

GADHIA, K., MCDONALD, S., ARKUTU, N. & MALIK, K. 2012. Amelogenesis imperfecta: an introduction. *Br Dent J,* 212**,** 377-9.

GAISER, S., DEYHLE, H., BUNK, O., WHITE, S. N. & MUELLER, B. 2012. Understanding Nano-Anatomy of Healthy and Carious Human Teeth: a Prerequisite for Nanodentistry. *Biointerphases,* 7.

GAO, X. J., ELLIOTT, J. C. & ANDERSON, P. 1993a. Scanning Microradiographic Study of the Kinetics of Subsurface Demineralization in Tooth Sections under Constant-Composition and Small Constant-Volume Conditions. *Journal of Dental Research,* 72**,** 923-930.

GAO, X. J., ELLIOTT, J. C., ANDERSON, P. & DAVIS, G. R. 1993b. Scanning Microradiographic and Microtomographic Studies of Remineralization of Subsurface Enamel Lesions. *Journal of the Chemical Society-Faraday Transactions,* 89**,** 2907-2912.

GIBSON, C. W., YUAN, Z. A., HALL, B., LONGENECKER, G., CHEN, E. H., THYAGARAJAN, T., SREENATH, T., WRIGHT, J. T., DECKER, S., PIDDINGTON, R., HARRISON, G. & KULKARNI, A. B. 2001. Amelogenin-deficient mice display an amelogenesis imperfecta phenotype. *Journal of Biological Chemistry,* 276**,** 31871-31875.

GLAS, J. E. 1962. Studies on the ultrastructure of dental enamel—II: The orientation of the apatite crystallites as deduced from X-ray diffraction. *Archives of Oral Biology,* 7**,** 91-IN15.

HABELITZ, S., MARSHALL, S. J., MARSHALL, G. W. & BALOOCH, M. 2001. Mechanical properties of human dental enamel on the nanometre scale. *Archives of Oral Biology,* 46**,** 173-183.

HAMMERSLEY, A. P. 1997. FIT2D: an introduction and overview. *ESRF Internal Report, ESRF97HA02T*.

HART, T. C., HART, P. S., GORRY, M. C., MICHALEC, M. D., RYU, O., UYGUR, C., OZDEMIR, D., FIRATLI, S., AREN, G. & FIRATLI, E. 2003. Novel ENAM mutation responsible for autosomal recessive amelogenesis imperfecta and localized enamel defects. *American Journal of Human Genetics,* 73**,** 558-558.

HICKS, M. J. & SILVERSTONE, L. M. 1984. Acid-etching of caries-like lesions of enamel: a polarized light microscopic study. *Caries Research,* 18**,** 315-26.

HIROTA, F. 1982. Prism arrangement in human cusp enamel deduced by X-ray diffraction. *Archives of Oral Biology,* 27**,** 931-7.

HIROTA, F. 1986. An Explanation for the "Two Fiber Axes" Problem in Human Enamel by X-ray Diffraction. *Journal of Dental Research,* 65**,** 978-981.

HOUNSFIELD, G. N. 1973. Computerized transverse axial scanning (tomography): Part 1. Description of system. *The British Journal of Radiology,* 46**,** 1016-1022.

HU, C. C., FUKAE, M., UCHIDA, T., QIAN, Q., ZHANG, C. H., RYU, O. H., TANABE, T., YAMAKOSHI, Y., MURAKAMI, C., DOHI, N., SHIMIZU, M. & SIMMER, J. P. 1997. Cloning and characterization of porcine enamelin mRNAs. *Journal of Dental Research,* 76**,** 1720-1729.

HU, C. C., HART, T. C., DUPONT, B. R., CHEN, J. J., SUN, X., QIAN, Q., ZHANG, C. H., JIANG, H., MATTERN, V. L., WRIGHT, J. T. & SIMMER, J. P. 2000. Cloning human enamelin cDNA, chromosomal localization, and analysis of expression during tooth development. *Journal of Dental Research,* 79**,** 912-919.

HU, J. C., CHUN, Y. H., AL HAZZAZZI, T. & SIMMER, J. P. 2007. Enamel formation and amelogenesis imperfecta. *Cells Tissues Organs,* 186**,** 78-85.

HU, J. C. C. & YAMAKOSHI, Y. 2003. Enamelin and autosomal-dominant amelogenesis imperfecta. *Critical Reviews in Oral Biology & Medicine,* 14**,** 387-398.

HUANG, T. T., JONES, A. S., HE, L. H., DARENDELILER, M. A. & SWAIN, M. V. 2007. Characterisation of enamel white spot lesions using X-ray micro-tomography. *Journal of Dentistry,* 35**,** 737-43.

ITO, M., EJIRI, S., JINNAI, H., KONO, J., IKEDA, S., NISHIDA, A., UESUGI, K., YAGI, N., TANAKA, M. & HAYASHI, K. 2003. Bone structure and mineralization demonstrated using synchrotron radiation computed tomography (SR-CT) in animal models: preliminary findings. *Journal of Bone and Mineral Metabolism,* 21**,** 287-293.

JENNINGS, R. J. 1988. A method for comparing beam-hardening filter materials for diagnostic radiology. *Medical Physics,* 15**,** 588-599.

JOHNSON, N. W. 1967. Some aspects of the ultrastructure of early human enamel caries seen with the electron microscope. *Archives of Oral Biology,* 12**,** 1505-1521.

KALENDER, W. A. 2006. X-ray computed tomography. *Physics in Medicine and Biology,* 51**,** R29-43.

KAY, M. I., YOUNG, R. A. & POSNER, A. S. 1964. Crystal Structure of Hydroxyapatite. *Nature,* 204**,** 1050-2.

KEREBEL, B., DACULSI, G. & KEREBEL, L. M. 1979. Ultrastructural studies of enamel crystallites. *Journal of Dental Research,* 58**,** 844-51.

LARSON, A. C. & VON DREELE, R. B. 2000. General Structure Analysis System (GSAS). *Los Alamos National Laboratory Report LAUR 86-748*.

LAUTENSACK, J., RACK, A., REDENBACH, C., ZABLER, S., FISCHER, H. & GRÄBER, H.-G. 2013. In situ demineralisation of human enamel studied by synchrotron-based X-ray microtomography – A descriptive pilot-study. *Micron,* 44**,** 404-409.

LEVENTOURI, T., ANTONAKOS, A., KYRIACOU, A., VENTURELLI, R., LIAROKAPIS, E. & PERDIKATSIS, V. 2009. Crystal Structure Studies of Human Dental Apatite as a Function of Age. *International Journal of Biomaterials,* 2009.

LIMAYE, A., 2006. Drishti - Volume Exploration and Presenatation Tool. *VIS.* Baltimore.

LOW, I. M. 2004. Depth-profiling of crystal structure, texture, and microhardness in a functionally graded tooth enamel. *Journal of the American Ceramic Society,* 87**,** 2125-2131.

LOW, I. M., DURAMAN, N. & MAHMOOD, U. 2008. Mapping the structure, composition and mechanical properties of human teeth. *Materials Science & Engineering C-Biomimetic and Supramolecular Systems,* 28**,** 243-247.

LYNCH, R. J. M. 2013. The primary and mixed dentition, post-eruptive enamel maturation and dental caries: a review. *International Dental Journal,* 63**,** 3-13.

MAHONEY, E. K., ROHANIZADEH, R., ISMAIL, F. S. M., KILPATRICK, N. M. & SWAIN, M. V. 2004. Mechanical properties and microstructure of hypomineralised enamel of permanent teeth. *Biomaterials,* 25**,** 5091-5100.

MANN, S. 2001. *Biomineralization : principles and concepts in bioinorganic materials chemistry,* Oxford, Oxford University Press.

MARDH, C. K., BACKMAN, B., HOLMGREN, G., HU, J. C. C., SIMMER, J. P. & FORSMAN-SEMB, K. 2002. A nonsense mutation in the enamelin gene causes local hypoplastic autosomal dominant amelogenesis imperfecta (AIH2). *Human Molecular Genetics,* 11**,** 1069-1074.

MARGOLIS, H. C., BENIASH, E. & FOWLER, C. E. 2006. Role of macromolecular assembly of enamel matrix proteins in enamel formation. *Journal of Dental Research,* 85**,** 775-793.

MATTHIES, S., WENK, H.-R. & VINEL, G. W. 1988. Some basic concepts of texture analysis and comparison of three methods to calculate orientation distributions from pole figures. *Journal of Applied Crystallography,* 21**,** 285-304.

MCCUSKER, L. B., VON DREELE, R. B., COX, D. E., LOUER, D. & SCARDI, P. 1999. Rietveld refinement guidelines. *Journal of Applied Crystallography,* 32**,** 36-50.

MECKEL, A. H., GRIEBSTEIN, W. J. & NEAL, R. J. 1965. Structure of mature human dental enamel as observed by electron microscopy. *Archives of Oral Biology,* 10**,** 775-783.

NANCI, A. & TEN CATE, A. R. O. H. 2003. *Ten Cate's oral histology : development, structure, and function,* St. Louis, Mo. ; [London], Mosby.

NANCI, A. & TEN CATE, A. R. O. H. 2008. *Ten Cate's oral histology : development, structure, and function,* St. Louis, Mo. ; [London], Mosby.

PATTERSON, A. L. 1939. The Scherrer Formula for X-Ray Particle Size Determination. *Physical Review,* 56**,** 978-982.

PAVLIC, A., SKRABA, P., KOSEC, L., PETELIN, M. & ALALUUSUA, S. 2007. Microhardness and microstructure of deciduous enamel with different types of amelogenesis imperfecta. *Central European Journal of Medicine,* 2**,** 511-527.

POOLE, D. F. G. & BROOKS, A. W. 1961. The arrangement of crystallites in enamel prisms. *Archives of Oral Biology,* 5**,** 14-IN5.

RASHBAND, W. S. 1997-2014. ImageJ. *National Institutes of Health , Bethesda, Maryland, USA,* http://imagej.nih.gov/ij/.

RAUE, L. & KLEIN, H. 2010. Location depending textures of the human dental enamel. *Texture and Anisotropy of Polycrystals Iii,* 160**,** 281-286 330.

RAUE, L. & KLEIN, H. 2011. Calculation of anisotropic properties of dental enamel from synchrotron data. *Journal of Synchrotron Radiation,* 18**,** 550-556.

RAUE, L. & KLEIN, H. 2012. New insights in prism orientation within human enamel. *Archives of Oral Biology,* 57**,** 271-276.

REYES-GASGA, J., MARTINEZ-PINEIRO, E. L. & BRES, E. F. 2012. Crystallographic structure of human tooth enamel by electron microscopy and x-ray diffraction: hexagonal or monoclinic? *J Microsc,* 248**,** 102-9.

RIETVELD, H. 1988. The Rietveld Method - A Historical Perspective. *Australian Journal of Physics,* 41**,** 113-116.

ROBINSON, C., ROBINSON, C., KIRKHAM, J. & SHORE, R. 1995. *Dental enamel: formation to destruction*, CRC Press.

ROBINSON, C., SHORE, R. C., BROOKES, S. J., STRAFFORD, S., WOOD, S. R. & KIRKHAM, J. 2000. The Chemistry of Enamel Caries. *Critical Reviews in Oral Biology & Medicine,* 11**,** 481-495.

SAKAE, T., HIRAYAMA, K., YAMAMOTO, H., SUZUKI, K., HAYAKAWA, Y., TAKAHASHI, Y., KUWADA, T., NAKAO, K., NOGAMI, K., INAGAKI, M., TANAKA, T., HAYAKAWA, K., SATO, I. & KAKEI, M. 2011. Three-dimensional Orientation Analysis of Human Enamel Crystallites Using X-ray Diffraction. *Journal of Hard Tissue Biology,* 20**,** 7-10.

SEIBERT, J. A. 2004. X-Ray Imaging Physics for Nuclear Medicine Technologists. Part 1: Basic Principles of X-Ray Production. *Journal of Nuclear Medicine Technology,* 32**,** 139-147.

SEREDIN, P., KASHKAROV, V., LUKIN, A., IPPOLITOV, Y., JULIAN, R. & DOYLE, S. 2013. Local study of fissure caries by Fourier transform infrared microscopy and X-ray diffraction using synchrotron radiation. *Journal of Synchrotron Radiation,* 20**,** 705-710.

SHORE, R. C., BACKMAN, B., ELCOCK, C., BROOK, A. H., BROOKES, S. J. & KIRKHAM, J. 2010. The Structure and Composition of Deciduous Enamel Affected by Local Hypoplastic Autosomal Dominant Amelogenesis Imperfecta Resulting from an ENAM Mutation. *Cells Tissues Organs,* 191**,** 301-306.

SIDDIQUI, S., ANDERSON, P. & AL-JAWAD, M. 2014. Recovery of Crystallographic Texture in Remineralized Dental Enamel. *Plos One,* 9**,** e108879.

SILVERSTONE, L. M. 1967. Observations on the dark zone in early enamel caries and artificial caries-like lesions. *Caries Research,* 1**,** 260-74.

SIMMER, J. P. & FINCHAM, A. G. 1995. Molecular Mechanisms of Dental Enamel Formation. *Critical Reviews in Oral Biology & Medicine,* 6**,** 84-108.

SIMMER, J. P. & HU, J. C. 2001. Dental enamel formation and its impact on clinical dentistry. *Journal of Dental Education,* 65**,** 896-905.

SIMMONS, L. M., AL-JAWAD, M., KILCOYNE, S. H. & WOOD, D. J. 2011. Distribution of enamel crystallite orientation through an entire tooth crown studied using synchrotron X-ray diffraction. *European Journal of Oral Sciences,* 119**,** 19-24.

SIMMONS, L. M., MONTGOMERY, J., BEAUMONT, J., DAVIS, G. R. & AL-JAWAD, M. 2013. Mapping the spatial and temporal progression of human dental enamel biomineralization using synchrotron X-ray diffraction. *Archives of Oral Biology,* 58**,** 1726-1734.

SUI, T., LUNT, A. J. G., BAIMPAS, N., SANDHOLZER, M. A., HU, J., DOLBNYA, I. P., LANDINI, G. & KORSUNSKY, A. M. 2014a. Hierarchical modelling of in situ elastic deformation of human enamel based on photoelastic and diffraction analysis of stresses and strains. *Acta Biomaterialia,* 10**,** 343-354.

SUI, T., SANDHOLZER, M. A., BAIMPAS, N., DOLBNYA, I. P., LANDINI, G. & KORSUNSKY, A. M. 2013. Hierarchical modelling of elastic behaviour of human enamel based on synchrotron diffraction characterisation. *Journal of Structural Biology,* 184**,** 136-146.

SUI, T., SANDHOLZER, M. A., LE BOURHIS, E., BAIMPAS, N., LANDINI, G. & KORSUNSKY, A. M. 2014b. Structure-mechanical function relations at nano-scale in heat-affected human dental tissue. *Journal of the Mechanical Behavior of Biomedical Materials,* 32**,** 113-124.

TAFFOREAU, P. 2007. Non-destructive 3D-investigation of dental microstructures and incremental features using X-ray synchrotron microtomography, new interpretation of the laminations vs. cross-striations phenomena. *Journal of Morphology,* 268**,** 1140-1140.

TAFFOREAU, P., BOISTEL, R., BOLLER, E., BRAVIN, A., BRUNET, M., CHAIMANEE, Y., CLOETENS, P., FEIST, M., HOSZOWSKA, J., JAEGER, J. J., KAY, R. F., LAZZARI, V., MARIVAUX, L., NEL, A., NEMOZ, C., THIBAULT, X., VIGNAUD, P. & ZABLER, S. 2006. Applications of X-ray synchrotron microtomography for non-destructive 3D studies of paleontological specimens. *Applied Physics a-Materials Science & Processing,* 83**,** 195-202.

TAFFOREAU, P., ZERMENO, J. P. & SMITH, T. M. 2012. Tracking cellular-level enamel growth and structure in 4D with synchrotron imaging. *Journal of Human Evolution,* 62**,** 424-428.

TANAKA, T., YAGI, N., OHTA, T., MATSUO, Y., TERADA, H., KAMASAKA, K., TO-O, K., KOMETANI, T. & KURIKI, T. 2010. Evaluation of the Distribution and Orientation of Remineralized Enamel Crystallites in Subsurface Lesions by X-Ray Diffraction. *Caries Research,* 44**,** 253-259.

TANG, R., DARRAGH, M., ORME, C. A., GUAN, X., HOYER, J. R. & NANCOLLAS, G. H. 2005. Control of Biomineralization Dynamics by Interfacial Energies. *Angewandte Chemie International Edition,* 44**,** 3698-3702.

TEN CATE, A. R. 1989. *Oral histology : development, structure, and function,* St. Louis, Mosby.

THEWLIS, J. 1940. The X-ray Examination of Enamel: (Section of Odontology). *Proc R Soc Med,* 33**,** 387-98.

TOBY, B. 2001. EXPGUI, a graphical user interface for GSAS. *Journal of Applied Crystallography,* 34**,** 210-213.

TOHDA, H., TAKUMA, S. & TANAKA, N. 1987. Intracrystalline structure of enamel crystals affected by caries. *Journal of Dental Research,* 66**,** 1647-53.

TOHDA, H., YANAGISAWA, T., TANAKA, N. & TAKUMA, S. 1990. Growth and Fusion of Apatite Crystals in the Remineralized Enamel. *Journal of Electron Microscopy,* 39**,** 238-244.

VERNON-PARRY, K. D. 2000. Scanning electron microscopy: an introduction. *III-Vs Review,* 13**,** 40-44.

VOEGEL, J. C. & FRANK, R. M. 1977. Stages in Dissolution of Human Enamel Crystals in Dental-Caries. *Calcified Tissue Research,* 24**,** 19-27.

VON DREELE, R. B. 1997. Quantitative texture analysis by Rietveld refinement. *Journal of Applied Crystallography,* 30**,** 517-525.

WANG, L. J., TANG, R., BONSTEIN, T., BUSH, P. & NANCOLLAS, G. H. 2006. Enamel demineralization in primary and permanent teeth. *Journal of Dental Research,* 85**,** 359-63.

WASSIF, H. 2007. Application of X-Ray Microtomography to Studies of Model Dental Caries Systems. Ph.D thesis. *Institute of Dentistry*, Queen Mary University of London.

WCISLAK, L., KLEIN, H., BUNGE, H. J., GARBE, U., TSCHENTSCHER, T. & SCHNEIDER, J. R. 2002. Texture analysis with high-energy synchrotron radiation. *Journal of Applied Crystallography,* 35**,** 82-95.

WENK, H. R. & HEIDELBACH, F. 1999. Crystal alignment of carbonated apatite in bone and calcified tendon: results from quantitative texture analysis. *Bone,* 24**,** 361-9.

WILSON, R. M., ELLIOTT, J. C. & DOWKER, S. E. P. 1999. Rietveld refinement of the crystallographic structure of human dental enamel apatites. *American Mineralogist,* 84**,** 1406-1414.

WILSON, R. M., ELLIOTT, J. C., DOWKER, S. E. P. & SMITH, R. I. 2004. Rietveld structure refinement of precipitated carbonate apatite using neutron diffraction data. *Biomaterials,* 25**,** 2205-2213.

WONG, F. S. L., ELLIOTT, J. C., ANDERSON, P. & DAVIS, G. R. 1996. An x-ray microtomographic study of dental tissue mineral concentration in rat incisors. *Journal of Dental Research,* 75**,** 1174-1174.

WONG, F. S. L., ELLIOTT, J. C., DAVIS, G. R. & ANDERSON, P. 2000. X-ray microtomographic study of mineral distribution in enamel of mandibular rat incisors. *Journal of Anatomy,* 196**,** 405-413.

WONG, F. S. L., WILLMOTT, N. S. & DAVIS, G. R. 2006. Dentinal carious lesion in three dimensions. *International Journal of Paediatric Dentistry,* 16**,** 419-423.

WRIGHT, J. T., LORD, V., ROBINSON, C. & SHORE, R. 1992. Enamel Ultrastructure in Pigmented Hypomaturation Amelogenesis Imperfecta. *Journal of Oral Pathology & Medicine,* 21**,** 390-394.

XIE, Z. H., MAHONEY, E. K., KILPATRICK, N. M., SWAIN, M. V. & HOFFMAN, M. 2007. On the structure-property relationship of sound and hypomineralized enamel. *Acta Biomaterialia,* 3**,** 865-872.

XIE, Z. H., SWAIN, M. V., SWADENER, G., MUNROE, P. & HOFFMAN, M. 2009. Effect of microstructure upon elastic behaviour of human tooth enamel. *Journal of Biomechanics,* 42**,** 1075-1080.

XUE, J., ZHANG, L. L., ZOU, L., LIAO, Y. M., LI, J. Y., XIAO, L. Y. & LI, W. 2008. High-resolution X-ray microdiffraction analysis of natural teeth. *Journal of Synchrotron Radiation,* 15**,** 235-238.

YAGI, N., OHTA, N., MATSUO, T., TANAKA, T., TERADA, Y., KAMASAKA, H., TO-O, K., KOMETANI, T. & KURIKI, T. 2009. Evaluation of enamel crystallites in subsurface lesion by microbeam X-ray diffraction. *Journal of Synchrotron Radiation,* 16**,** 398-404.

YANAGISAWA, T. & MIAKE, Y. 2003. High-resolution electron microscopy of enamel-crystal demineralization and remineralization in carious lesions. *Journal of Electron Microscopy,* 52**,** 605-613.

YIN, Y., YUN, S., FANG, J. & CHEN, H. 2009. Chemical regeneration of human tooth enamel under near-physiological conditions. *Chemical Communications,* 0**,** 5892-5894.

YOUNG, R. A. 1974. Implications of atomic substitutions and other structural details in apatites. *Journal of Dental Research,* 53**,** 193-203.

YOUNG, R. A. 1993. *The Rietveld method,* Oxford, Oxford University Press.

YOUNG, R. A. & MACKIE, P. E. 1980. Crystallography of Human Tooth Enamel - Initial Structure Refinement. *Materials Research Bulletin,* 15**,** 17-29.

ZOU, W., HUNTER, N. & SWAIN, M. V. 2011. Application of Polychromatic μCT for Mineral Density Determination. *Journal of Dental Research,* 90**,** 18-30.

Appendix

Conference presentations

1. XMaS Users Meeting – Warwick, United Kingdom – May 2011 (Poster presentation)
   2D Mapping of Dental Enamel Affected by Caries
   S. Siddiqui*, M. Al-Jawad, R. Wilson, P. Anderson

2. BSODR- Sheffied, United Kingdom - September 2011 (Oral presentation)
   2D Mapping of Dental Enamel Affected by Caries
   S. Siddiqui*, M. Al-Jawad, R. Wilson, P. Anderson
   GSK MINTIG (Mineralised Tissue Group) Prize winner

3. Dental Imaging & Materials, London, United Kingdom-February 2012 (Poster presentation)
   X-ray Microtomography study of Hypomaturation Amelogenesis Imperfecta
   S. Siddiqui*, G. R. Davis, M. Al-Jawad

4. Diamond Users Meeting – September 2012 (Poster presentation)
   2D Mapping of Dental Enamel Affected by Caries
   S. Siddiqui*, M. Al-Jawad, R. Wilson, P. Anderson
   Engineering & Imaging Group Prize winner

5. IADR – Seattle, United States America – March 2013 (Poster presentation)
   Crystallographic & Microstructural Studies of Teeth Affected by Amelogenesis Imperfecta
   S. Siddiqui*, M. Al-Jawad, G. R. Davis

6. ORCA – Liverpool, United Kingdom – July 2013 (Poster and oral presentation)
   Restoration of Demineralised Enamel by Synthesis of Ordered Apatite Crystals
   S. Siddiqui*, B. Clarkson, H. Chang, M. Al-Jawad

7. XMaS users meeting - Warwick, United Kingdom – May 2014 (Poster presentation)
   Restoration of Demineralised Enamel by Synthesis of Ordered Apatite Crystals

S. Siddiqui*, B. Clarkson, H. Chang, M. Al-Jawad

Publications

1. Samera Siddiqui, Paul Anderson, Maisoon Al-Jawad. Recovery of Crystallographic Texture in Remineralized Dental Enamel, PLOS ONE (accepted) (2014)